

AD-A062 390

WASHINGTON UNIV SEATTLE

F/G 20/5

FLUID MECHANICAL REFRACTING GAS PRISM AND AERODYNAMICS OF E - B--ETC(U)

MAY 78 D W BOGDANOFF, W H CHRISTIANSEN

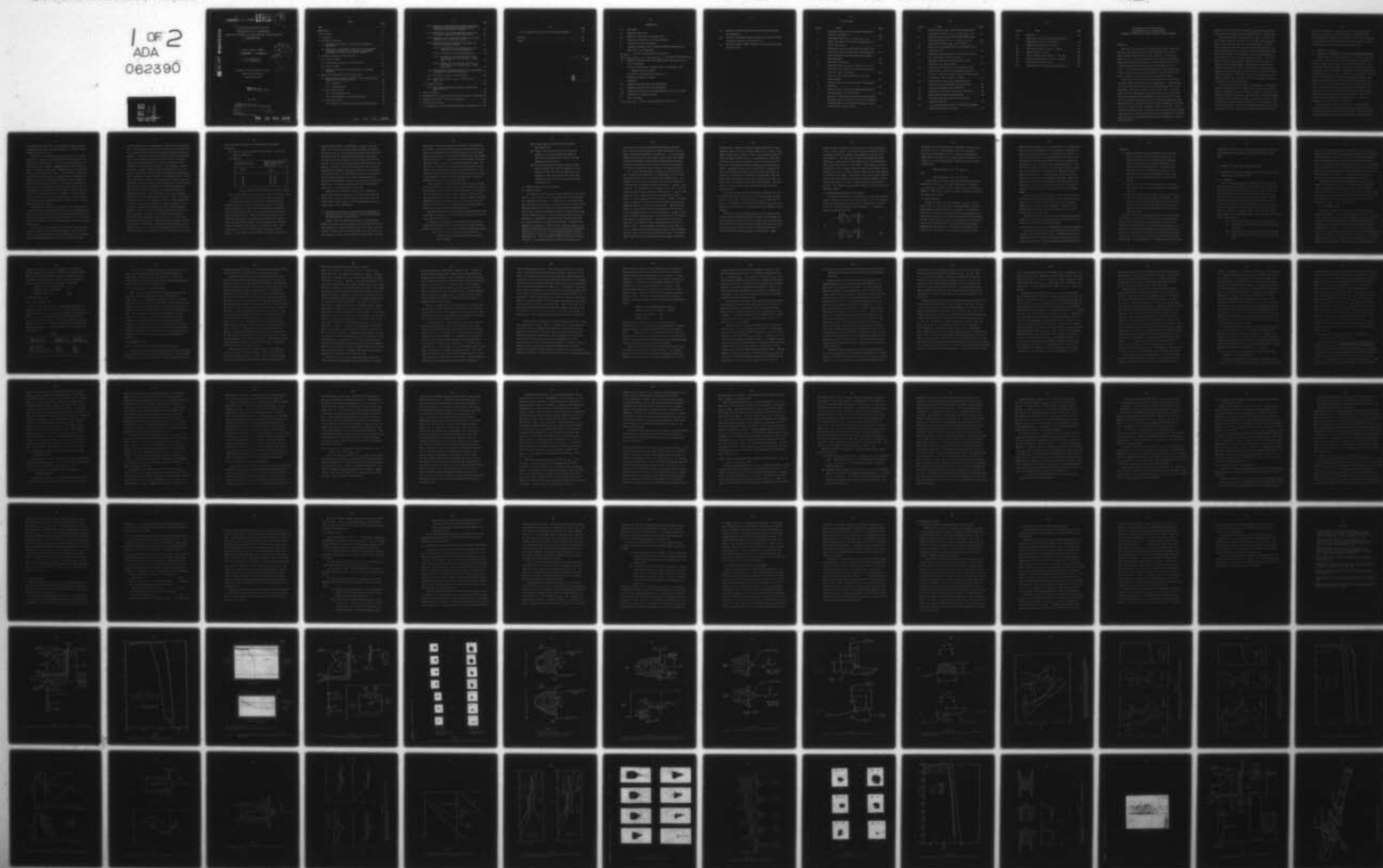
AFOSR-74-2650

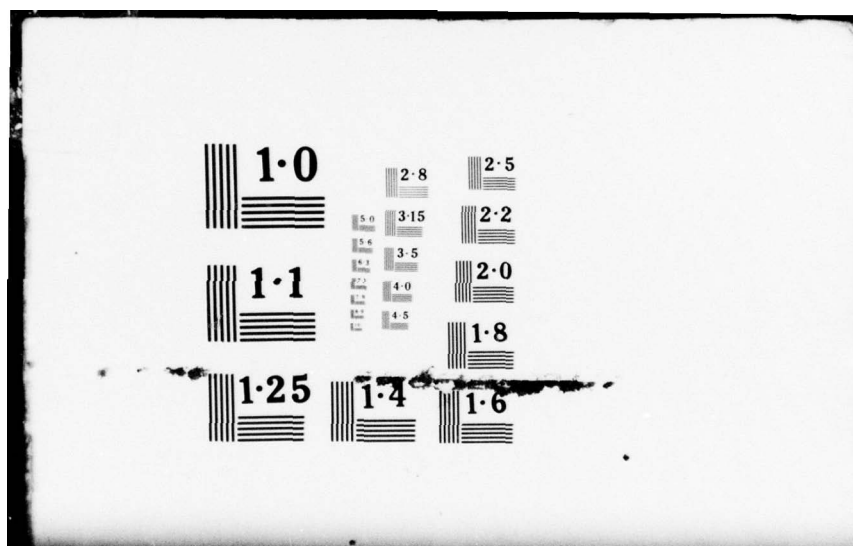
UNCLASSIFIED

AFOSR -TR-78-1494

NL

1 OF 2
ADA
062390





DDC FILE COPY AD A062390

18 AFOSR-TR-78-1494

LEVEL II

3

6
FLUID MECHANICAL REFRACTING GAS PRISM
AND AERODYNAMICS OF E - BEAM SUSTAINED

DISCHARGE IN SUPERSONIC FLOW, BOTH APPLICABLE TO LASER TECHNOLOGY.

15 AFOSR-74-2650

9 Interim Scientific Report

1 January 1977 - 31 December 1977

10 D. W. Bogdanoff
W. H. Christiansen

DDC
DEC 14 1978

Aerospace & Energetics Research Program

University of Washington

Seattle, Washington

Approved for public release;
distribution unlimited.

May, 1978

AIR FORCE OFFICE OF SCIENTIFIC RESEARCH (AFSC)
NOTICE OF TRANSMITTAL TO DDC
This technical report has been reviewed and is
approved for public release IAW AFR 190-12 (7b).
Distribution is unlimited.
A. D. BLOSE
Technical Information Officer

370 240

78 12 04.040

JOB

INDEX

	Page
Index	i
Nomenclature	iv
List of Figures	vi
1. Introduction	1
2. Experimental Techniques	3
2.1 Description of Experimental Technique for Transmission Measurements	3
2.2 Description of Experimental Techniques for the Measurement of the Shape and Size of the Light Well and the Angular Divergence of the Beam Leaving the Venus Machine	7
3. Theoretical Discussion of the Light Well	9
3.1 Light Well Shapes	9
3.2 Maximum Angular Tolerance of the Light Well	12
3.3 Partial Trapping	13
3.4 Influence of Random Density Perturbations on Light Well Performance	14
4. Comparison of Theoretical and Experimental Data	16
4.1 Determination of Extent of Light Well and Divergence Angle of Output Beam from Photographic Data	16
4.1.1 Light Wells	16
4.1.2 Divergence Angles	17
4.2 Presentation of Data	18
4.2.1 1974 Photographic Data	18
4.2.2 1977 Photographic and Transmission Data	19
4.3 Discussion of Data	19
4.3.1 Fall-off of Transmission Values with Decreasing ρ_0/ρ_s . .	19

	Page
4.3.2 Discussion of Some Differences Between Experimentally Determined and Theoretically Predicted Light Well Limits and Maximum Angular Tolerances	26
4.3.3 Estimation of the True Maximum Angular Tolerance of the Light Well Based on the Tail Calculation	30
4.3.4 Tendency of High Transmission Conditions to be Associated with ϕ_r and ϕ_z less than ϕ_{TE} and ϕ_w	31
4.3.5 Detailed Discussion of the Data from Two Series of Test Runs on the Venus Machine	32
4.3.5.1 Some Discussion of Transmission Data with Reference to Light Well Photographs	32
4.3.5.2 Estimated True Light Well Contour Plots	34
4.3.5.3 Discussion of the Operating Conditions of the Data of Figs. 13 and 20b ($x_{in} \approx .20$ mm, $\rho_{00}/\rho_s \approx 95$)	35
4.3.5.4 Discussion of the Operating Conditions of the Data of Figs. 12 and 20a ($x_{in} \approx -.16$ mm, $\rho_{00}/\rho_s \approx 95$)	39
4.3.6 Photographically Indicated Extension of the Light Beyond the Downstream Limits of the Light Well	44
4.3.7 Scattering of Light in the Venus Machine	44
4.3.8 Comparison of Data for $\rho_{00}/\rho_s \approx 68$ with that for $\rho_{00}/\rho_s \approx 95$	45
4.4 Transmission Data.	46
4.4.1 Data at High Transmission Conditions; Accuracy and Reproducibility	47
5. Additional Remarks	49
6. Recommendations for Future Low Power Research on the 90° Venus Machine.	50
7. High Power Experiments on the 90° Venus Machine	53
8. The Electrical Discharge	55
8.1 Aerodynamics of E-beam Sustained Discharges in Supersonic Flow . .	55

	Page
8.2 The Supersonic Flow Facility and Discharge Apparatus	56
References	59
Figures	60

ACCESS FOR	
NTIS	Exempt Section <input checked="" type="checkbox"/>
and	Exempt Section <input type="checkbox"/>
EXEMPTED BY	
EXEMPTED BY DATE	
A	

Nomenclature

M	Mach number
n	Refractive index of gas
n_w	Refractive index of gas at the nozzle wall
r	Distance from central axis of the Venus Machine
T	Transmission of the Venus Machine
x	In general, distance in the r direction measured upstream from the nozzle exit (-ve if downstream)
x_d, x_{dh}, x_u	See Fig. 9 and discussion of Section 4.1.1
$x_{d,T}, x_{d,w,n\Delta T}, x_{d,n,\Delta T}, x_{u,T}, x_{u,w,n\Delta T}, x_{u,w,\Delta T}$	See discussion of Section 4.2.1
x_{in}	Distance of center of input laser beam upstream from the nozzle exit (-ve if downstream)
z	(1) Axial coordinate for the Venus Machine; the $z=0$ plane is the symmetry plane of the nozzle (2) See Fig. 9 and discussion of Section 4.1.1
Δ	Difference of quantity following
λ	Wavelength
θ	Azimuthal coordinate around the Venus Machine
ρ_0	Stagnation gas density for the Venus Machine
ρ_{00}	Stagnation gas density for the Venus Machine at the start of a test
ρ_s	Gas density at standard conditions
ϕ	Angle, in general
$\phi_r, \phi_z, \phi_{TAIL}, \phi_{ref}$	See Fig. 10 and discussion of Section 4.1.2

- ϕ_T Theoretical maximum angular tolerance of the light well based
tail calculation
- ϕ_{TE} Estimated true maximum angular tolerance of the light well based
on the tail calculation; see Section 4.3.3
- ϕ_W Theoretical maximum angular tolerance of light well based on the
wall calculation

List of Figures

Figure	Title	Page
1	Experimental setup for beam transmission measurements in the 90° Venus Machine	60
2	Transmission data for $x_{in} \approx 0.0$ mm, $\rho_{oo}/\rho_s \approx 95$	61
3	Typical data pictures for transmission measurement on the 90° Venus Machine	62
4	Experimental setup for photographing the shape of the light well and the divergence angle of the output beam . .	63
5	Typical light well shape and output beam divergence angle photographs	64
6	Venus Machine geometries	65
7	Calculated shape of light well, variation of nr with r along light well centerline and variation of $n_w r$ with r along walls (wall calculation)	66
8	Light well shapes calculated in Ref. 6 using ray tracing methods	67
9	Parameters used to describe the shapes of photographed light wells	68
10	Parameters used to describe the photographed shapes of the output beams of the Venus Machine	69
11	Comparison of theoretically predicted and experimentally determined light well extents in the radial (x) direction. 1974 photographic data, and upstream light well limits estimated from transmission data	70

Figure	Title	Page
12	Light well radial extent, output beam divergence angle and transmission data for $x_{in} \approx -.16$ mm, $\rho_{00}/\rho_s \approx 95$	71
13	Light well radial extent, output beam divergence angle and transmission data for $x_{in} \approx .20$ mm, $\rho_{00}/\rho_s \approx 95$	72
14	Transmission data for $\rho_{00}/\rho_s \approx 95$, various x_{in}	73
15	Estimation of the upstream limit of the light well from transmission data	74
16	Light well shape and nr versus r profile for discussion of r oscillations of light in the well	75
17	Light well shape sketch for discussion of r and z oscillations of light in the well	76
18	Sketches used in discussion of the estimation of the true nr versus r profile along the nozzle centerline	77
19	nr versus r profile and limiting lines; used in discussion of estimates of true nr versus r profiles	78
20	Output divergence angle data, shown plotted with theoretical and quasi-theoretical limiting curves	79
21	Light well photographs; early (1974) data	80
22	Estimated true nr contour plots for the light wells	81
23	Output beam divergence angle photographs	82
24	Transmission data taken under high transmission operating conditions	83
25	nr contour plots and nr versus r profiles for recommended improved Venus Machine light wells	84

Figure	Title	Page
26	Ruby laser	85
27	Experimental setup for high power transmission measurements on the 90° Venus Machine	86
28	Schematic of discharge/flow facility	87
29	Test section pressure history, $t = 1\text{ms/div}$	88
30	Oblique shock on 2-D wedge	88
31	E-Beam voltage & current traces, $t = 50\text{ }\mu\text{s/div}$	89
32	Sustainer voltage-current traces, $t = 50\text{ }\mu\text{s/div}$	89
33	Interferogram of cathode shock	90
34	Interferogram of flow process with discharge on	90

FLUID MECHANICAL REFRACTING GAS PRISM
AND AERODYNAMICS OF E - BEAM SUSTAINED
DISCHARGE IN SUPERSONIC FLOW, BOTH APPLICABLE TO LASER TECHNOLOGY

INTRODUCTION

Small power losses associated with refraction of light in gases have motivated us to develop and study a unique fluid mechanical device for possible manipulation and storage of laser radiation. In the work performed to date, it has been shown that a beam of light can be deflected continuously through large angles along a curved path using the flow from a convergent-divergent nozzle sector whose throat lies on an arc of a circle. The flow devices that have been built and studied, based on this concept, have been named Venus machines because of the similarity to the optical conditions predicted to exist in the atmosphere of Venus.

Nozzle sectors with nominally included angles of 30° , 90° , and 180° have been studied both theoretically and experimentally. In these devices it has been clearly demonstrated that a well-defined region exists in the flow wherein light rays are trapped in near circular paths. This report details extensive measurements on the 90° device which was built in 1974. Preliminary photographic measurements^{2,3} of the size and shape of the light well and preliminary quantitative laser beam transmission measurements were obtained in 1974-75. Extensive transmission data was obtained in the following year¹, indicating maximum transmission values of $99.5 \pm 0.5\%$. In the same period, theoretical work in comparison with the experimental data yielded information on (a), stabilization of the light well perpendicular to the flow direction, and on (b) possible detrimental effects of turbulence on Venus machine performance.

Several ways of improving the Venus Machine performance were identified from the work of 1976 and applied to the construction of a 360° machine.

New transmission data is presented in this report. This data permits detailed analysis of the light well and a more accurate assessment of the optimum operating conditions of the Venus Machine. A motion-picture photographic technique was used to obtain extensive data on the size and shape of the light well under a variety of operating conditions. The angular divergence of the laser beam leaving the Venus Machine was also measured for the same range of operating conditions. These experimental results, along with parallel theoretical work, have allowed a reasonably complete understanding of the operation of the present 90° device at low laser power levels. Construction of a ruby laser and the necessary optical and detector systems for high-power Venus Machine transmission was completed. Preliminary calibration measurements with the detector system were made. The results of this year's effort is presented in some detail in the following report.

An electron-beam sustained electric discharge laser producing either pulsed or continuous power laser radiation from a supersonic gas flow is a promising approach for high-power laser development. The utility of the supersonic expansion as a means for achieving low gas temperatures required for efficient laser performance is known. Several ideas are under active consideration by the Air Force and the feasibility is unquestioned. Some of the basic information required for improved performance of these devices is being carried out in small-scale experiments using facilities at the

University of Washington. Some considerations include discharge boundary layer interactions and medium homogeneity. Preliminary results of the fundamental mechanisms of the interaction of electrical discharges of the glow type and the fluid mechanics as found in supersonic electric discharge lasers are also briefly mentioned in this report.

2. EXPERIMENTAL TECHNIQUES

2.1 DESCRIPTION OF EXPERIMENTAL TECHNIQUE FOR TRANSMISSION MEASUREMENTS

Figure 1 shows the experimental apparatus. A 1mW He:Ne laser beam is injected into the flow field by means of a SELFOC light guide.⁸ The input and output windows of the Venus Machine are antireflection coated to minimize interference problems. The output beam from the light guide is focused down to $\sim 125\mu$ diameter and injected on the nozzle symmetry plane. Using a 40x microscope, the beam is positioned to an accuracy of ± 0.02 mm. Prior to entering the nozzle, the beam is chopped at about 300 Hz and a portion is split off to provide a reference to which the output can be compared. There is a polarizer preceding the beam splitter (polarizer 1). This was found necessary because the laser beam is not perfectly randomly polarized. Drifts in the dominant polarization direction change the reference beam strength in the optical bridge as a result of the changing effective reflectivity of the beam splitter. Insertion of polarizer 1 eliminates this optical phenomena.

The measurement is carried out as follows: a calibrated prism of known transmission is aligned to reflect the input beam to the output window and the silicon photodetector behind it. (Since the intense cooling effect produced by the expanding gas causes ambient water vapor

to condense on the prism after a run, the prism is cleaned and recalibrated before every run. The maximum variation in the measured prism transmission values is ~0.3%.)

Polarizer 2 is then rotated to adjust the intensity of the reference beam at its detector, and thus equalize the signal outputs of the reference and output detectors. This is detected by one channel of the oscilloscope, which displays the difference signal between the two detectors. While this signal is zero, the two detectors are balanced and "see" the same effective light signal. The Venus Machine is then activated with the high pressure gas, and the laser beam is deflected continuously by the flow. The output and reference detector signals are again subtracted at the oscilloscope. If the gas flow transmission is the same as that of the prism, the difference signal remains zero. If the transmission is higher than the prism value, the signal is positive and if it is lower than this value it is negative. To obtain high sensitivity the difference signal is displayed at twice as large a deflection sensitivity on the oscilloscope as the reference signal. The Venus Machine was operated as follows.

The machine was allowed to run continuously from a selected initial stagnation pressure (typically 900-1500 psia) down to the pressure where the light well totally collapsed due to the decreasing density gradients. This latter pressure value was typically 650 to 900 psia. Run times under these conditions were 6-18 sec. Data was taken over a range of input laser beam positions.

At this point, it is appropriate to discuss the discovery and resolution of a problem in the experimental technique. In the first part of 1977, a detailed comparison of the 1976 transmission data with theory revealed unsatisfactory agreement for the lower stagnation pressure

portions of test runs. The disagreement was traced to the following phenomena. As a test proceeds, the temperature of the gas in the supply reservoir and, hence, that of the gas flow in the Venus Machine drops due to expansion. Hence, the flow produces an intense increasing cooling effect on the inside surfaces of the input and output windows of the machine. The high thermal conductivity of the fused silica windows allows the cooling effect to be relatively rapidly felt at the outside surfaces of the windows. Typically, about 6 seconds after the start of a run, the outside surfaces reach the ambient dew point temperature and condensation starts, spoiling all further transmission (or photographic) data. Theoretical calculations of the point on a run at which the window outside surfaces reach the dew point show excellent agreement with the experimentally observed point at which the transmission data starts showing behavior very difficult to explain from theory. The condensation problem was eliminated by building a system to maintain a flow of dry N_2 over the outside surfaces of the windows during a test run. Figure 2 shows transmission data from two test runs plotted in the form of beam transmission, T , versus ρ_0/ρ_s (ρ_s is the gas density at standard conditions, $0^\circ C$ and 760 torr). The two runs were taken under nearly identical operating conditions, that is, position of the input laser beam and initial value of ρ_0/ρ_s (ρ_{00}/ρ_s). The dashed line (1976 data) shows the artifact of fall-off of beam transmission starting at $\rho_0/\rho_s \approx 72$, which is due to condensation on the windows. The solid line shows data taken in 1977 using N_2 flow over the windows. (The slight difference between the two curves for $\rho_0/\rho_s > 72$ is probably due to unavoidable small errors in setting and measuring the input beam position - see section 4.4.1). The effect

of the condensation phenomena on data discussed in this report is given below.

- (a) 1977 data (new data presented in this report) - N_2 gas flow used, no condensation.
- (b) 1976 data

Initial Density Ratio	Density Ratio below which data is suspect due to condensation
ρ_{00}/ρ_s	ρ_o/ρ_s
~95	72 - 78
~80	61 - 66
~69	52 - 57
~58	44 - 48

For ρ_o/ρ_s above the "suspect value," the 1976 data is good.

- (c) The 1974 and 1975 data were taken with shorter runs where gas cooling of the device was insufficient to produce condensation.

A Kistler pressure gauge was connected to a charge amplifier and a second oscilloscope. Both oscilloscopes were triggered simultaneously just before the start of a run, and timing pulses were applied to the cathodes of both scopes, allowing accurate correlation of pressure and transmission data. Typical data pictures are shown in Fig. 3. The vertical scratches on the pictures are knife marks made after the run to facilitate reading the data. From the pressure data, the instantaneous gas density in the reservoir is calculated as follows. For each of the four values of initial density ratio (ρ_{00}/ρ_s) used for testing, a large number of runs have been made, starting at about the

same reservoir pressure, but descending to a range of final pressures. For each run, the initial reservoir pressure, the pressure at the end of the test, and the pressure several minutes later, when the reservoir gas has warmed up to room temperature, were taken. This data allows one to construct, for given initial reservoir conditions, a curve of pressure versus density which applies during the test run. Using this curve and the pressure data from the oscilloscope picture, the density ratio (ρ_0/ρ_s) at any time in the test run is readily calculated. For the 1976 data, the gas in the reservoir was not allowed to expand as far, and the simple assumption of a isentropic pressure-density relation in the reservoir was found to be satisfactory. The greater expansion ratios used in the 1977 work required the more complex procedure given above.

Typically transmission data is shown in Fig. 2 (referred to earlier with respect to condensation). Six runs of this type were taken in 1977, covering a range of input laser beam positions, and initial density ratios (ρ_{00}/ρ_s). The transmission data will be discussed further later in this report.

2.2 DESCRIPTION OF EXPERIMENTAL TECHNIQUES FOR THE MEASUREMENT OF THE SHAPE AND SIZE OF THE LIGHT WELL AND THE ANGULAR DIVERGENCE OF THE BEAM LEAVING THE VENUS MACHINE.

Figure 4 shows the experimental apparatus. The Venus Machine proper and the laser and coupler assembly are as in Figure 1; however, the photodetectors, chopper, polarizers, etc. of the latter set-up are not used. A lens forms an image of the light well at the exit of the Venus Machine on a sheet of paper mounted on a glass plate. Paper was

used to avoid the strongly peaked forward scattering of ground glass - this latter is objectionable especially when the angular spread of the beam is to be measured (see the following paragraph.). A 16 mm motion picture camera using Kodak 4x negative film (ASA 400) was used to photograph the light well. Two lamps very close to the plane of the paper were used to give a scale factor for the motion picture frames. The pressure in the reservoir is recorded during motion picture test runs just as it was during transmission test runs (see Section 2.2.) The timing pulse applied to the cathode of the pressure gauge oscilloscope is also applied to a third lamp near the imaging paper to allow synchronization of pressure and motion picture data.

This experimental set-up allows one to measure the size and shape of the light well at the output window of the Venus Machine. To measure the divergence angle of the beam at the output window of the Venus Machine, the imaging lens is simply removed. Otherwise, the experimental set-up is essentially as shown in Fig. 4. Typical light-well shape and output beam divergence angle data (single frames from the motion picture film) are shown in Fig. 5. The two series of data were taken at nearly, but not quite, identical operating conditions.

For both the light well shape and beam divergence angle beam, tests were taken at three sets of operating conditions, involving two values of ρ_{00}/ρ_s and two values of x_{in} .

A word should be said at this point about the early light well shape photographs taken in 1974. The set up used for these tests was basically very similar to that of Fig. 4 with the following differences.

- (a) Short runs, about 1 sec long, were used; there was no condensation and H_2 window bleed flow was neither used nor needed.

- (b) A still camera was used; only one data picture was taken per run.
- (c) Pressure data was obtained by simply reading the pressure in the reservoir before and after the test runs; the average value was taken as the stagnation pressure for the run.
- (d) At the input window of the Venus Machine, the light well was flooded with light; this contrasts with the 1977 experiments, where the input beam size is substantially smaller than the size of the light well, allowing the beam to be used to probe the structure of the light well.

3. THEORETICAL DISCUSSION OF THE LIGHTWELL

3.1 LIGHTWELL SHAPES

It is readily shown⁴⁻⁷ that for a stable light well to exist there must be a local maximum of nr in the flow pattern of the Venus Machine (n = refractive index of gas, r = distance from axis of machine; standard cylindrical co-ordinates, r , θ and z , are used in this discussion.) The shape and size of the light well can be predicted from theory for various nozzle shapes and operating conditions by calculating nr values over the region of interest in the flow field and plotting contours of constant nr . Frederick⁵ has computed the flow field for an inviscid $M = 1$ jet discharging into a region of low pressure. The geometry for Frederick's calculation is shown in Fig. 6a. Light well shapes for the 90° Venus Machine have been estimated by using Frederick's calculations downstream of the nozzle exit and a simple one-dimensional analysis upstream of the nozzle exit. The two methods are spliced together at the nozzle exit. The true geometry of the 90° Venus Machine is shown in Fig. 6b. The difference between the theoretical model used for

the light well and the real machine geometry probably accounts for some of the differences between the calculated and observed light well shapes and beam divergence angles (see Section 4): It was not, however, judged worthwhile to perform the necessary (substantially more complex) calculations to attempt to obtain better agreement between theory and experiment, especially since future higher performance Venus Machines will likely not produce the type of light well of the present device.

Fig. 7 shows calculated light well shapes and the variation of nr with r along the nozzle centerline. The dashed curve in Fig. 7b gives the variation with r of nr at the nozzle walls (denoted by $n_w r$). The ordinate in Fig. 7b has been inverted so stability can be interpreted in the usual way (the bottoms of valleys are stable). In general, at any r -coordinate in the light well, nr is greatest on the r -axis. Along the r -axis the point of maximum stability in the light well is point B. Also along the r -axis, a stability limit of the light well is at point C. Light at $r > r_c$ will rapidly be lost from the well. Outside of the nozzle exit, the light well is stabilized in the z -direction by strong density gradients which exist in the inviscid flow pattern. Upstream from the nozzle exit, there would be almost no stabilization of the light well in the z -direction based on the inviscid flow pattern. However, in this region, the thermal boundary layers at the nozzle walls act to stabilize the light well in the z -direction. A second stability limit of the light well is the "bottom" (actually the maximum) of the $n_w r$ curve in Fig. 7b, point G. This corresponds to the physical points H and I in Fig. 7a. Light passing through the boundary layers in the neighborhood of points H and I will strike the walls (which are rough on an optical scale) and will tend to be scattered outside the angular tolerance of

the light well. Theoretical light well shapes are obtained by simply noting the values of nr at the limiting points (C and G in Fig. 7b) and drawing contour lines at these nr values. This procedure produces the light well shapes sketched in Fig. 7a. The dashed line is the light well shape based on the limiting point C ("tail calculation") and the solid line is the shape based on the limiting point G ("wall calculation"). The points A and C on the nr curve in Fig. 7b correspond to the tail calculation, and points G and F to the wall calculation. For simplicity, the comparison of theoretical and experimental light well shapes will be made largely by using the x-coordinates of points A and C (or E and F, as necessary) as the theoretical prediction. These numbers give a measure of the maximum extent of the light well in the radial direction.

The light well shape and size are strongly dependent on the reservoir stagnation density ratio (ρ_0/ρ_s). Fig. 7 shows, roughly sketched, wells for $\rho_0/\rho_s = 80$. For higher values of ρ_0/ρ_s , the light well is deeper, and conversely, for sufficiently low values of ρ_0/ρ_s , the local maximum of the nr curve of Fig. 7b disappears and the light well vanishes entirely.

For long test runs of the Venus Machine, with a substantial drop in the reservoir (stagnation) temperature, there are two limiting ways to calculate the $n_w r$ curve of Fig. 7b, and hence, the "wall calculation" light well limits. For one calculation, the walls are assumed to remain at room temperature as the run proceeds. This would be the case if the walls had infinite thermal conductivity and capacity. These

results of these calculations will be referred to as "wall calculations, no ΔT " or " $w, n\Delta T$ " results. In the other limiting calculation, the walls are assumed to follow the adiabatic wall temperature of the gas as the latter decreases. This would occur if the walls had negligible thermal conductivity. These results of these calculations will be referred to as "wall calculation, with ΔT " or " $w, \Delta T$ " results. Heat transfer calculations indicate that, after 10 seconds running of the real Venus Machine, the wall temperature will be, very roughly, half-way between the two simple theoretical results discussed above. This number is only a crude estimate, however, as the correct heat transfer calculations for the wall temperature are extremely complicated, and it was not judged profitable to pursue them at this time. For comparison with experiment, both $w, \Delta T$ and $w, n\Delta T$ results will therefore be given.

3.2 MAXIMUM ANGULAR TOLERANCE OF THE LIGHTWELL

An important characteristic of the light well is the maximum tolerable angular deviation of a ray path from the θ -direction. For a ray travelling at the most stable location in the light well, corresponding to point B in Fig. 7b, the maximum tolerable angular deviation, θ , (in radians) is given to a good approximation by

$$\phi = \left\{ 2 \left[\frac{(nr)_B - (nr)_C}{(nr)_C} \right] \right\}^{1/2}, \quad (1)$$

or

$$\phi = \left\{ 2 \left[\frac{(nr)_B - (n_w r)_G}{(n_w r)_G} \right] \right\}^{1/2}, \quad (2)$$

according as the limiting point of the light well is taken as point C or point G in Fig. 7b. Corresponding to the "wall calculation, no ΔT " and "wall calculation, with ΔT " results for the light well shape, there are two values for ϕ , based on the wall calculation (i.e., using point G as the limiting point). Those two values of ϕ will be referred to as

$$\phi_{\text{wall calculation, no } \Delta T} \quad \text{or} \quad \phi_{W, n \Delta T},$$

and

$$\phi_{\text{wall calculation, with } \Delta T} \quad \text{or} \quad \phi_{W, \Delta T}.$$

As in the case of the "wall calculation" of the light well shape, the estimated value of ϕ_W for the real Venus Machine lies between $\phi_{W, \Delta T}$ and $\phi_{W, n \Delta T}$, and correct values would be extremely difficult to calculate. Both values of ϕ_W will, therefore, be plotted in comparison with experimental results.

3.3 PARTIAL TRAPPING

"Light well" shapes taken from reference 6 for $\rho_0/\rho_s = 57$ are shown in Fig. 8. These "light wells" were calculated by a technique which differs from that presented in this report. A large number of light rays arranged in an array and travelling in the θ direction were assumed to be injected into the nozzle exit region of the Venus Machine. The path of each light ray, that is, its movement in the r and z directions as it moves around the Venus Machine, was computed using the known density field of the flow. Many light rays were shown to be lost from the light well--i.e., the calculations indicated a rapid

and irreversible increase in r or in $|z|$ for the ray. The "light wells" shown in Fig. 8 are the boundaries of the regions at the optical exit of the Venus Machine within which the outgoing rays are located. It is to be noted that this type of calculation must be done for a specific machine (in the cases shown, 180° and 30°), and is dependent on the deflection angle. Two other points should be noted here. First, for a large enough deflection angle, perhaps several complete revolutions, the "light wells" calculated by this method should approach those calculated by the nr - contour method, since almost all rays which were ever going to be lost would have been lost. Second, the nozzle shape used for these calculations has parallel instead of converging wall, and thus, the "light wells" shown in Fig. 8 cannot be compared in complete detail with those calculated for the 90° Venus Machine.

The point illustrated by a comparison of the "light wells" shown in Fig. 8 for 30° and 180° Venus Machines is that the envelope of the outgoing rays in a Venus Machine is larger for smaller deflection angles (all other factors remaining constant). In particular, the envelope shows an extension in the r -direction near the $z = 0$ axis for the smaller deflection angle.

Rays which are trapped in a light well for significant deflection angles (e.g., 30°), but which would escape for some larger deflection angle, are considered to be "partially trapped."

3.4 INFLUENCE OF RANDOM DENSITY PERTURBATIONS ON LIGHT WELL PERFORMANCE

Discussion of the light well up to this point has ignored the influence of random density perturbations. [The discussion of the (turbulent) boundary layer involved only the mean refractive index difference across the layer.] Three main classes of perturbations will be

considered:

- 1) density perturbations in the free stream flow in the light well region which are caused by residual temperature and pressure perturbations carried downstream from turbulence producing regions such as the supply pipe boundary layers and two 90° bends in the supply pipe. (The pressure perturbations are those associated with the turbulence velocities.) Of the two types of perturbations, those of temperature produce the most serious effect on light well performance.
- 2) density perturbations in the free stream flow in the light well region caused by acoustic noise radiation from the boundary layer.
- 3) density perturbations in the boundary layer in the light well region due to pressure and temperature perturbations. These density perturbations affect the performance of the light well directly since they affect light rays which have approached the wall and have been reflected back into the light well by the boundary layer.

An earlier section has introduced the concept of the maximum angular tolerance of the light well. The effect of any density perturbations will be to introduce random angular deviations along any ray transversing the Venus Machine. Some light rays, which would be trapped in the light well for the (hypothetical) case of flow without perturbations, will be lost from the wall due to random angular deviations in real flow. The rays most likely to be lost would be those injected nearest the limits of the light well. The random angular deviation would

be expected to increase with increasing density perturbation amplitude (other things remaining constant), and can be estimated for certain cases.

4. COMPARISON OF THEORETICAL AND EXPERIMENTAL DATA

4.1 Determination of Extent of Light Well and Divergence Angle of Output Laser Beam from Photographic Data.

4.1.1 LIGHT WELLS

Fig. 9 shows sketches made from typical frames of the light well motion picture data (see Section 2.2). Referring first to Figure 9(a), the measurements of light well extent were made as follows. The scale factor was determined from the fact that, at higher values of ρ_0/ρ_s , the light well filled the space between the nozzle walls, and thus z on the film corresponds to known distance between the walls, .401 mm. The location of the nozzle exit is established since, at higher ρ_0/ρ_s values, the Prandtl-Meyer fan originating at the nozzle edge is known to form a corner on the light-well (points A and B, Fig. 9a). With these reference points established, three measures were taken of the radial extent of the light well:

- x_u - the extent of the well upstream from the nozzle exit
- x_d - the total extent of the well downstream from the nozzle exit, and
- x_{dh} - the extent of the light well downstream from the nozzle exit, considering only regions of heavy exposure on the film.

x_{dh} is, to some degree arbitrary, but does allow one to distinguish between faint "tails" of the light well and portions of the well containing substantial amounts of light. All x -values are taken to be negative if they extend downstream from the nozzle exit, and positive for the converse. For motion picture frames taken at lower ρ_0/ρ_s values (e.g. Fig 9b), for which the light well is no longer attached to the corner of the nozzle exit, the nozzle exit location can still be obtained by carrying over the location established at higher ρ_0/ρ_s values using the reference marks which are on a graticle placed at the imaging plane (see Fig. 4).

The above description of data handling applies to the 1977 data. The older (1974) data, taken with a still camera, could be handled by very similar techniques, except that no reference mark is available. Hence, for data at lower ρ_0/ρ_s values, which are detached from the nozzle exit, the extent of the light well upstream and downstream from the nozzle exit cannot be determined. Only the total extent of the well can be measured (i.e. $x_{total} = |x_u| - |x_d|$ in Fig. 9b).

4.1.2 DIVERGENCE ANGLES

Fig. 10 shows sketches made from single frames of the divergence angle motion pictures. Fig. 10a shows a sketch for a condition where most of the light is contained within the light well and the transmission is high. Fig. 10b shows a sketch for a condition where the light is escaping out the tail of the light well and the transmission decreases rapidly with decreasing ρ_0/ρ_s . The angular scale of the light spot in these frames is established by the images of two lamps known to subtend an angle of 4.95 degrees. The location of the estimated center of the exposed spot (relative to the lamp image locations) remains fixed to within ± 0.5 degrees in both directions. The estimated center of the exposed spot is

indicated by the cross in Fig. 10. The shape of the exposed spot does vary, depending on conditions, but most of the comparison of this report will be based on the overall extent of the spot in the r and z directions and on the extent of the tail. These three measures of spot extent are illustrated in Fig. 10 and are listed below.

- Extent of spot in radial direction - ϕ_r
- Extent of spot in z direction - ϕ_z
- Extent of tail of spot - ϕ_{TAIL}

4.2 PRESENTATION OF DATA

4.2.1 1974 Photographic Data

Fig. 11 shows a comparison of the theoretical calculations and experimental measurements for the radial (x) extent of the light well. The experimental curves, x_u , x_d and x_{dh} are obtained as described in section 4.1.1. The x-position of the center of the light well for $42 \leq \rho_o/\rho_s \leq 50$ is uncertain because of the lack of a photographic reference point (see section 4.1.1). This data is shown dotted. The theoretical calculations were made as described in section 3.1; the notation system is given below:

TABLE I

Type of Calculation (see Section 3.1)	Upstream Light Well Limit	Downstream Light Well Limit
tail calculation	$x_{u,T}$	$x_{d,T}$
wall calculation, no ΔT	$x_{u,w,n \Delta T}$	$x_{d,w,n \Delta T}$
wall calculation, with ΔT	$x_{u,w, \Delta T}$	$x_{d,w, \Delta T}$

The test runs for the photographic data lasted only about ~1 sec, and, hence, the change of the gas reservoir stagnation temperature during these runs was quite small (see section 2.1). The six data points in Fig. 11 with bars were obtained from transmission measurements and will be discussed further in section 4.3.1.

4.2.2 1977 Photographic and Transmission Data

Figs. 12 and 13 show light well radial extent, output beam divergence angle and transmission data for two operating conditions: $\rho_{oo}/\rho_s \approx 95.4$, $x_{in} \approx -.16$ mm (Fig. 12) and $\rho_{oo}/\rho_s \approx 95.4$, $x_{in} \approx .20$ mm (Fig. 13). Each figure presents data from three different test runs taken at almost identical operating conditions. The data of Figs. 12(a) and 13(a) are presented in the same form as that of Fig. 11 (see Section 4.2.1). Figs. 12(b) and 13(b) show experimental beam divergence angle data plotted as a function of ρ_o/ρ_s obtained by the techniques described in Sections 2.2 and 4.1.2. These two figures also show theoretical curves for the maximum angular tolerance of the light well calculated according to the methods of sections 3.1 and 3.2. Figs. 12(c) and 13(c) show the corresponding 1977 transmission data. Fig. 14 shows 1977 transmission data for four test runs with $\rho_{oo}/\rho_s \approx 95$ and with different values of x_{in} .

4.3 DISCUSSION OF DATA

4.3.1 Fall-Off of Transmission Values with Decreasing ρ_o/ρ_s .

The irregular type of fall-off of machine transmission with decreasing ρ_o/ρ_s reported in the 1976 annual report proved to be an artifact produced by water condensation as the Venus Machine input and output windows (see

relevant discussion in Section 2.1). With this problem eliminated, transmission data shows a smooth fall-off of transmission (Fig. 14).

A comparison will now be made among the upstream limits of the light well determined from 1977 (and some 1976) transmission data, the 1974 photographic data, and the theoretical predictions. Curves for the latter two are shown in Fig. 11. The six data points with bars in Fig. 11 were determined from transmission data as follows. The ordinate of each point is the ρ_0/ρ_s value at which the transmission dropped to 0.5. The abscissa is the value of x_{in} for the test run. The four points with the lowest values of x were taken from the transmission data of Fig. 14. The two data points at higher x values were obtained from 1976 transmission data where a rapid fall-off of transmission with decreasing ρ_0/ρ_s was observed at ρ_0/ρ_s values above those at which condensation occurs. These old data runs contain errors of the order of 3-5% in the transmission values which do not, however, prevent good estimation of the ρ_0/ρ_s value at which $T = 0.5$. The slopes of the bars through the six data points represent estimates of the local slopes of the light well limit curve in the $\rho_0/\rho_s - x$ plane, obtained from the transmission data as follows. The general form of the $nr-r$ profile along the centerline of the light well as shown previously in Fig. 7 is reproduced in Fig. 15(a). the limiting point of the light well is point J. The x -coordinate of the center of the input laser beam for the run in question is x_{in} and the estimated diameter of the input beam is d .

The position and size of the input laser beam is represented by bar 2 in Fig. 15(a). If $nr(J) = nr(x_{in})$, as shown in Fig. 15(a), the following simplified argument can be made. Half of the light injected to would be expected to be lost from the well by passing over point J,

while the remaining light would be trapped in the well. Based on this argument, the transmission is 0.5. for the finite sized input beam. This argument is the basis for taking $T = 0.5$ data points from transmission data as measures of the location of the light well limits in the $\rho_0/\rho_s - x_{in}$ plane. If the input laser beam were to be moved $d/2$ to the right in Fig. 15(a), the expected transmission value would be 1.0 based on the simplified argument, or perhaps ~ 0.9 , roughly allowing for the fact that the beam is not cut off sharply at the estimated beam diameter. Similarly if the beam were to be moved $d/2$ to the left, the transmission would be expected to be 0 (sharply defined beam) or ~ 0.1 (more realistic beam profile). Thus, the $T = 0.5$ point in this test run, combined with the beam size estimate, defines, roughly, three points in a plot of T vs ρ_0/ρ_s and x_{in} for an input laser beam with diameter d . These three points are points A,B,and C in Fig. 15(b), with transmissions of 0.5, 0.1 and 0.9, respectively. The run data defines directly two other points with $T = 0.9$ and 0.1, points D and E. Thus, locally, contours of constant T can be drawn in the $\rho_0/\rho_s - x_{in}$ plane for $T = 0.1$ and $T = 0.9$ (the lines through points B and E and D and C, respectively). The line for $T = 0.5$ is taken to be parallel to the $T = 0.1$ and $T = 0.9$ lines. Extending an earlier argument that the $T = 0.5$ point in the test run represents a point on the light well limit curve in the $\rho_0/\rho_s - x_{in}$ plane, the $T = 0.5$ lines are taken as local estimates of the position of the light well limit line in the neighborhood of the six data points in Fig. 11. These estimates are the bars on the data points in Fig. 11. The extent of the bars in the x-direction corresponds to the diameter of the input laser beam.

The agreement shown in Fig. 11 between the upstream light wells limits determined from photographic and transmission data is regarded

by the investigators as satisfactory, though not exact. It should be noted that the photographic data involved short runs with little drop in the reservoir temperature, while the transmission data involved long runs with substantial reservoir temperature drop. Some of the differences between the photographic and transmission light well limits shown in Fig. 11 is likely traceable to the fact that the x_{in} for the transmission data is measured at the input window while x_{in} for the photographic data is measured at the output window. The input and output windows of the Venus Machine do not exactly correspond to each other, due to manufacturing and mounting errors.

In Fig. 11, the upstream well limits indicated in Fig. 11 by both the photographic and the transmission data, but especially the latter, show a marked similarity to the $x_{u,T}$ theoretical curve; the latter curve if shifted 0.20 mm to the right would match the experimental data quite well. This point will be returned to in section 4.3.2.

It is noted from Fig. 11 that the upstream well limits determined from both photographic and transmission data appear to show little respect for the theoretical well curves based on the wall calculations (see Section 3.1). The reason for this is believed to be fairly well understood and is presented below. It is convenient in the discussion to consider the transmission data run which yielded the light well limit point at $x = .67$ mm, $\rho_o/\rho_s = 86$ in Fig. 11. For this run, the transmission was ~ 0.95 at $\rho_o/\rho_s = 95$. Fig. 16 (similar to Fig. 7) shows light well shapes and $nr-r$ curves for the case in point. The light is injected centered on point M (Fig. 16a) and immediately begins to oscillate strongly in the r direction in the light well. The path of these oscillations can be represented on the $nr-r$ curve as taking place

(Fig. 16b) between points K and L. The light rays will travel at a maximum angle to the azimuthal direction (near point B on the $nr-r$ curve) of ~ 5.4 degrees. The maximum angular tolerance of the light well, implicitly based on oscillations in the r -direction (tail calculation, Section 3.2) is ~ 7.3 degrees. The maximum angular tolerance of the well, implicitly based on oscillations in the z -direction (wall calculation, Section 3.2) is ~ 3.9 degrees. For the question at hand, an important point is how rapidly the initial strong oscillations of the light ray in the r -direction are translated into oscillations in the z -direction. Fig. 17 shows a more realistic path for a light ray, injected at point a, illustrating crudely how z -oscillations may be generated from initial ray motion which is primarily in the r -direction. Motion of the light ray in the z -direction (neglecting density perturbation effects) is generated mainly by "reflections" of the rays from the regions of the light well downstream of the nozzle exit, which contain strong nr gradients in the r and z directions.

Two possibilities would appear to exist which would explain the $T = 0.95$ value obtained for the $\rho_0/\rho_s = 95$, $x_{in} = .67$ mm test run, for which the light rays are oscillating at angles up to 5.4 degrees in the r direction and the maximum angular tolerance of the light well is 3.9 degrees based on the wall calculation (implied z -oscillations). The first possibility is that strong z -oscillations of the light ray are quickly generated from the initial r -oscillations as the ray traverses the Venus Machine. The number of bounces which the light ray makes while traversing the Venus Machine is readily estimated to be about 10 in the r -direction and 20 or less in the z -direction. A number of the bounces in the z -direction will take place at incident angles greater

than the angular tolerance of the well based on the well calculation. Hence, light rays will strike the walls on the order of 10 times at incidence angles readily calculated to be up to ~3 degrees. The high transmission of the Venus Machine under these conditions could only be explained if the reflectivity of the aluminum walls was very high -- of the order of .995 at incidence angles of 1 to 3 degrees. For a perfect aluminum surface, the reflectivity is ~.990 for the relevant incidence angles. The Venus Machine nozzle wall surfaces were simply turned on a lathe. They cannot readily be tested for reflectivity. However, representative machined surfaces were tested with the following results.

Reflectivity of machined aluminum surfaces at
incidence angles of 1.2 degrees ($\lambda = 6328 \text{ \AA}$).

Finely milled surface - ~.82

Buffed Surface - ~.92

Based on the above reflectivities, it is concluded that the high transmission of the Venus Machine under the conditions in question cannot be based on repeated reflections of the light off the nozzle walls. Hence, under these operating conditions, the light, for the largest part, must not strike the nozzle walls. Hence, the oscillations in the z-directions must be restricted to angles significantly less than those which are known to occur in the r-direction.

From the original series of tests of beam divergence angle, there is no data which directly confirms this conclusion. It is also not feasible to interrupt the present program of high-power transmission measurements in the Venus Machine to take the relevant tests. However,

it may be possible in June, 1978 or thereabouts to perform the tests. The tests would be very simple, i.e. a divergence angle test run for $x_{in} = .67$ mm and $\rho_{00}/\rho_s = 95$. At the $T \approx 0.95$ condition ($\rho_0/\rho_s = 95$) if the divergence angles were measured to be ~ 5.4 degrees in the r-direction, but less than ~ 3.9 degrees in the z-direction, the conclusion reached in the previous paragraph would be confirmed. Contrarily, if the divergence angles were observed to be substantially greater than ~ 3.9 degrees in the z-direction, the conclusion would be contradicted and another explanation must be sought.

The conclusion of restricted z-oscillations tends to be confirmed by available divergence angle data which shows that for a number of operating conditions, the divergence angle of the beam leaving the Venus Machine is substantially smaller in the z-direction than in the r-direction. The largest difference in the divergence angles is noted in the data of Fig. 13b, for $\rho_0/\rho_s = 90 - 95$, where ϕ_r is $3.0 - 3.2$ degrees while ϕ_z is 1.9 degrees.

The conclusions of the present discussion, which are believed to be fairly well (though not completely) established are restated below. First, the high transmission conditions obtained at $\rho_0/\rho_s = 90 - 95$ for the test run which yielded the $\rho_0/\rho_s = 86$, $x_{in} = .67$ mm point in Fig. 11 occur, despite estimated r-oscillation angles of ~ 5.4 degrees, and wall calculation angular tolerance limits of ~ 3.9 degrees, because the strong r-oscillations of the light rays generate z-oscillations of significantly smaller amplitude while traversing the Venus Machine. The same phenomena is believed to account for the fact that for $\rho_0/\rho_s \geq 80$, the upstream well limits determined from transmission on photographic data do not respect the wall calculation light well limits in Fig. 11.

4.3.2 Discussion of Some Differences Between Experimentally Determined And Theoretically Predicted Light Well Limits and Maximum Angular Tolerances.

A number of points from the experimental data suggest that the light well shapes and nr vs r profiles are somewhat different than predicted by the theoretical work of Section 3. The main theoretical element for comparison with the experimental results is the nr versus r curve, which will now be discussed. The portion of the curve upstream of the nozzle exit is based on a simple one-dimensional analysis and should be quite accurate. The portion of the curve downstream from the nozzle exit was based on the expansion of a parallel $M = 1$ jet, not a jet issuing from a slot with walls inclined at 4 degrees to the flow centerline direction as is the case in reality. The inward momentum of the jet upstream of the nozzle exit would be expected to delay the expansion of jet downstream of the exit to a certain degree. Also no attempt was made in the calculations to allow for boundary layer effects, which might be expected to produce more serious disturbances to the flow in the downstream, supersonic free jet flow regions, than in the upstream, subsonic bounded flow. In general, the portion of the nr versus r profile downstream from the nozzle exit is regarded as much more suspect than that further upstream. There are also machining and alignment errors which may effect the nr versus r profiles in ways difficult to determine.

The location of the most stable point in the light well (point B, Fig. 7b) can be estimated from the transmission data of Fig. 14 by cross-plotting the latter in the form of T versus x_{in} with ρ_0/ρ_s as a parameter. For $60 \leq \rho_0/\rho_s \leq 95$, the maxima of these curves are fairly well defined

and agree well with the theoretical positions for the most stable position in the light well obtained from the nr versus r curves. For $\rho_0/\rho_s < 60$, it is not possible to construct a smooth curve through data cross-plotted from Fig. 14 which properly locates the maxima. For $\rho_0/\rho_s \geq 60$, the most stable point in the light well (and the maxima of the cross-plotted transmission data) are upstream of the nozzle exit. The good agreement between theory and experiment referred to above lends support to the assumption that the theoretical nr versus r curves should be fairly accurate upstream of the nozzle exit.

The upstream light well limits determined from photographic data (Figs. 11, 12a and 13a) and transmission data (Fig. 11) suggest a curve which, for $\rho_0/\rho_s \geq 50$, lies about 0.20mm to the right of the theoretical tail calculation curve. (The difference apparently increases to .25 to .30 mm for $\rho_0/\rho_s < 50$.) This suggests that the true nr versus r curve differs from that calculated according to the methods of Section 3 in a way which will now be discussed referring to Fig. 18. Fig. 18a reproduces, slightly modified, the nr versus r curve, for $\rho_0/\rho_s = 80$, of Fig. 7b. The theoretical light well limits, according to the calculation, is based on the height of point C; line 1 drawn through point C establishes the two limits, point C itself and point A. The experimental data of Figs. 11, 12a and 13a indicate that the upstream light well limit is at point a instead of point A. If one assumes that the limiting point in the light well is not at the nozzle walls (following the earlier discussion of z -oscillations and r -oscillations), it must lie on the nr curve of Fig. 18a downstream of the nozzle exit; it also must lie on line 2 through point a. The experimental data suggests

an $nr - r$ curve which, downstream of the nozzle exit, is represented by the dotted curve in Fig. 18a. This sort of analysis leads to similar rough estimates for the real $nr - r$ curves for lower ρ_0/ρ_s values. Examples are shown in Fig. 18b and Fig. 18c for $\rho_0/\rho_s = 60$ and $\rho_0/\rho_s = 50$. For the lower ρ_0/ρ_s values, point c is to the right of point C, whereas for $\rho_0/\rho_s = 80$ it is to the left.

The estimation of the form of the true $nr - r$ curves as described in the preceding paragraph is supported by divergence angle data from Figs. 12b and 13b. The data of Fig. 13b for $57 \leq \rho_0/\rho_s \leq 63$ and particularly the data of Fig. 12b for $47 \leq \rho_0/\rho_s \leq 63$ suggest a curve for the maximum angular tolerance of the light well which lies about one degree below the theoretical curve based on the tail calculation. (The difference increases to ~ 1.5 degrees for $\rho_0/\rho_s \approx 47$.) From the limiting line (line 2) in the $nr - r$ diagram of Fig. 18b (determined from photographic and transmission data of Fig. 11) a Δnr value can be determined, measured from the bottom of the light well to the line. Using an expression similar to Eqn. 1 (section 3.2), a maximum angular tolerance of the light well can be calculated. This value can then be compared with the observed angular extent of the beam leaving the Venus Machine (the data of Figs. 12b and 13b). This comparison was performed for $\rho_0/\rho_s = 60$ (Fig. 18b) and other ρ_0/ρ_s values between 47 and 63. For $55 \leq \rho_0/\rho_s \leq 63$, the agreement was excellent, supporting the procedures for estimating the true $nr - r$ curve described earlier. For $\rho_0/\rho_s \approx 50$, the agreement is no longer good. The comparison between the Δnr value determined from the transmission data and the theoretical curve (Δnr_1)

and the value determined from the divergence angle data (Δnr_2) suggests that the true $nr - r$ curve is as sketched in Fig. 18(c). For this value of ρ_0/ρ_s , the maxima of the theoretical $nr - r$ curve is approximately at the nozzle exit location; the experimental data suggests that the maximum is downstream of this point and of a higher value.

Much of the data of Figs. 11, 12, 13 and 14 appears to indicate a total disappearance of the light well (under the most favorable conditions of light injection) at ρ_0/ρ_s between 42 and 45. The theoretical curves indicate that the light well should continue to exist down to $\rho_0/\rho_s = 27$. This fact suggest that for, say, $\rho_0/\rho_s = 40$, the comparison between the theoretical and real $nr - r$ curves is as shown in Fig. 18d (estimated real curve shown dotted downstream of the nozzle exit). The theoretical curve still has a shallow local maxima and would produce a light well, while the real curve no longer has a maxima or produces a light well. It is noted here that random scattering of light from density fluctuations in the light well (e.g. free-stream and boundary - layer turbulence) would tend to cause light well failure at higher ρ_0/ρ_s values than predicted theoretically. Light which would theoretically be trapped in the light well (the theoretical calculations take no account of turbulence) can be scattered out of the well by the turbulent density fluctuations.

However, observations from experimental data (see Section 4.3.7) appear to indicate that the random scattering of light by density fluctuations is not strong enough to cause light well failure at $\rho_0/\rho_s = 42$ if the theoretical light well shapes were correct.

The differences between the theoretical $nr - r$ curves and the estimated true curves (estimated as discussed in this section) can be made roughly self-consistent over the range of ρ_0/ρ_s values considered as

follows. Fig. 19 shows, for a particular value of ρ_0/ρ_s , the theoretical $nr - r$ curve, the estimated true curve and two limiting lines. The n_0r line is evaluated at the gas density at the nozzle stagnation conditions; the $n_{fe}r$ line is evaluated at the gas density at full expansion to the ambient pressure outside the nozzle. Far upstream of the nozzle, $nr =$ curve approaches the n_0r line. If the region of the nozzle exit, the $nr - r$ curve changes rapidly from being close to the n_0r line to being close to the $n_{fe}r$ line. All the estimated true $nr - r$ curves discussed earlier suggest that, downstream from the nozzle exit, the expansion of the gas does not take place as fast in fact as is predicted theoretically. The amount by which the expansion lags behind that predicted theoretically is roughly consistent as determined over the complete range of estimated $nr - r$ curves discussed earlier. This strongly suggests, but does not prove, that delayed expansion downstream from that nozzle exit is the main cause for the difference between the theoretical and estimated true $nr - r$ curves.

An important contribution to the delayed expansion is probably due to the inward momentum of the gas flow approaching the nozzle exit; this occurs since the nozzle walls are inclined at ~ 4 degrees to the center line of the flow. The theoretical model assumed the supersonic expansion starts with a parallel flow $M = 1$ jet. Boundary layer effects and machining and alignment errors may also contribute to the differences between the theoretical and estimated true $nr - r$ curves.

4.3.3 Estimation of the True Maximum Angular Tolerance of the Light Well Based on the Tail Calculation

The divergence angle data of Figs. 12(b) and 13(b) is reproduced in Fig. 20 with an estimated true θ_T curve added. This curve was obtained,

as described below, following very closely many of the arguments presented in Section 4.3.2 with respect to the estimation of the true $nr - r$ curve. For $55 \leq \rho_0/\rho_s \leq 95$, the curve was obtained by noting the x value of the upstream limit of the light well obtained from the experimental transmission and photographic data presented in Fig. 11. Combining this information with the theoretical $nr - r$ curve (which appears to be fairly accurate upstream of the nozzle exit —see Section 4.3.2) yields a nr difference between the light well limit and the bottom of the well. Using an equation similar to Eqn. 2, Section 3.2, the estimated true maximum angle tolerance of the light well (ϕ_{TE}) based on the (pseudo-) tail calculation is obtained. For $47 \leq \rho_0/\rho_s \leq 55$, the curve basically follows the ϕ_z and ϕ_r curves of Fig. 20(a). There are, however, reasons for doing this which are consistent with the overall picture for the estimated true nr versus r curves developed in section 4.3.2. Finally, ϕ_{TE} is taken to go to zero at the point of light well failure ($\rho_0/\rho_s \approx 42$) indicated by many of the data of Fig. 11, 12, 13 and 14. Again, the $nr - r$ discussion of section 4.3.2 contains arguments very relevant to this assumption.

4.3.4 Tendency of High Transmission Conditions to be Associated

With ϕ_r and ϕ_z Less Than ϕ_{TE} and ϕ_w .

Comparing the transmission data of Figs. 12(c) and 13(c) with the Fig. 20 shows that high transmission divergence angle and ϕ_{TE} and ϕ_w data of/conditions are associated with ϕ_r and ϕ_z values which are significantly below both the ϕ_{TE} and ϕ_w limits. In this connection, it should be pointed out that crude heat transfer calculations (see Section 3.1) indicate that for the lower ρ_0/ρ_s values ($\rho_0/\rho_s = 45 - 65$) the best estimate for the location of the true ϕ_w curve is roughly halfway between the two curves shown. For higher values of

ρ_0/ρ_s the true ϕ_w curve would be expected to be progressively closer to the $\phi_{w,\Delta T}$ curve, based on heat transfer arguments. In particular, the highest transmissions, those of Fig. 13(c) (and Figs. 13b and 20b) for $\rho_0/\rho_s > 75$ are associated with ϕ_z and ϕ_r values ranging from 1 to 2.5 degrees below the ϕ_w and ϕ_{TE} limits, with the very highest T value (arrow Fig. 20b) occurring at a minimum of ϕ_r . The $x_{in} \approx -.16$ mm data (Figs. 12, 20a) does not show such outstandingly high T values, but the range of the highest T values of the run, $65 \leq \rho_0/\rho_s \leq 75$, corresponds to that region where the ϕ_r and ϕ_z values are below both the ϕ_{TE} and ϕ_w limits. In this region the ϕ_r and ϕ_z values average 0.7 to 1.0 degrees below the limits with the highest T value (arrow, Fig. 20a) centered in the region of relatively low ϕ_r and ϕ_z . Under operating conditions yielding lower T values, the ϕ_z and ϕ_r values tend to be quite close to either ϕ_w or ϕ_{TE} . The correspondence noted in this paragraph is to be expected, since ϕ_r or ϕ_z values near the limiting curves means that some light is on the point of being lost from the well; these conditions would be expected along with lower T values.

4.3.5 DETAILED DISCUSSION OF THE DATA FROM TWO SERIES OF TEST RUNS ON THE VENUS MACHINE

The two series of test runs to be discussed are those yielding the data of Figs. 12 and 20a, $\rho_{00}/\rho_s \approx 95$, $x_{in} \approx -.16$ mm, and those yielding the data of Figs. 13 and 20(b), $\rho_{00}/\rho_s \approx 95$, $x_{in} \approx .20$ mm.

4.3.5.1 SOME DISCUSSION OF TRANSMISSION DATA WITH REFERENCE TO LIGHT WELL PHOTOGRAPHS

The photographs presented in this discussion were those taken in 1974 (see Section 2.2). They were taken with the input window of the

Venus Machine flooded with light, and should provide a fairly accurate measure of the total extent of the light well. The only significant difference between the operating conditions for the photographs and those for the data of Figs. 12, 13 and 20 is that long runs with a drop in the gas reservoir temperature were taken for the latter, and short runs for the former. This means that the theoretical limiting curves for the light well shape and maximum angular tolerance based on the wall calculation are the " $n \Delta T$ " curves in Figs. 12 and 13 for the photographs but would lie somewhere between the " $n \Delta T$ " and the " ΔT " curves for the remaining data. See discussion of Sections 3.1 and 3.2. This difference is relatively small and would appear to affect the following discussion only slightly, but should be borne in mind.

The photographs for eight different values of ρ_0/ρ_s are shown in Fig. 21. The circles are of the estimated "diameter" of the input laser beam. The beam is, of course, not sharply bounded at this diameter; there is some power outside the indicated circle. Except for the case of $\rho_0/\rho_s = 43.9$ each photograph shows the position of the input laser beam for $x_{in} \approx -.16$ mm (Fig. 12 and 20a) and for $x_{in} \approx .20$ mm (Fig. 13 and 20b). The circle in the tail of the light well is that for $x_{in} \approx -.16$ mm. It was not possible to establish r and z coordinate references for the picture with $\rho_0/\rho_s = 43.9$; only the diameter of input laser beam is indicated in this case.

In the discussion to follow it should be borne in mind that one does not expect a near-perfect quantitative agreement between Fig. 21 and the data of Figs. 12, 13 and 20. In particular, the photographs of Fig. 20 are of the output window of the Venus Machine whereas the position of the input beam is measured at input window and there are manufacturing

and mounting errors which make these two position not strictly equivalent. This alone would preclude agreement of very high accuracies.

For $x_{in} \approx .20$ mm (Fig. 13c), $T > .980$ for $\rho_0/\rho_s \geq 67$ and is greater than .990 for $\rho_0/\rho_s \geq 74$ reaching a value of .997 at $\rho_0/\rho_s \approx 80$. In contrast, for $x_{in} \approx -.16$ mm (Fig. 12c) T ranges from .910 to .955 for $53 \leq \rho_0/\rho_s \leq 95$ with .955 being the maximum value. Turning to Fig. 21, it can be seen that for $x_{in} \approx .20$ mm and $\rho_0/\rho_s \geq 75$, the input laser beam is centered well inside the light well, so that not only the central portion of the beam (roughly indicated by the circle) but a large amount of the light in the outlying regions is injected inside the light well. This fact is believed to account for the very high transmission measured under these operating conditions. For $x_{in} \approx -.16$ mm, $50 \leq \rho_0/\rho_s \leq 91$, however, it is apparent from Fig. 21 that there are no ρ_0/ρ_s values where the input laser beam is injected such that the central and the outlying regions of the beam are as deeply inside the light well as is the case for $x_{in} \approx .20$ mm. Under this whole range of ρ_0/ρ_s values, it is believed that a significant part of the outlying regions of the input laser beam misses the light well, accounting for the lower transmission values of .91 to .955 (the maximum value).

4.3.5.2 ESTIMATED TRUE LIGHT WELL CONTOUR PLOTS

Fig. 22 shows estimated true light well nr contours plots constructed as follows. The nr values along the centerline upstream of the nozzle exit were taken from the theoretical nr-r curves discussed in Section 3.1. The nr values along the centerline downstream of the nozzle exit were taken from the estimated true nr-r curves in this region which were obtained as described in Section 4.3.2. The height of the nr jump through

the boundary layer is taken from a comparison of the theoretical nr and $n_w r$ curves obtained as discussed in Section 3.1. The thickness of the boundary layer is greatly exaggerated in Fig. 22 for clarity. The contour forming the boundary of the light well is taken from the photographs of Fig. 21. The variations of nr in the z -direction downstream of the nozzle exist were obtained from the theoretical calculations of Ref. 4. These calculations, although done for slightly different conditions than those of the Venus Machine, should give a fair estimate of the z -structure of the light well downstream of the nozzle exit. The plots of Fig. 22, while not of extreme accuracy, are believed to give a fairly good estimate of the true structures of the light wells. Note that the contour intervals are not the same for the five values of ρ_0/ρ_s . In each contour plot, the size and location of the input laser beam for the two operating conditions to be discussed in the two succeeding sections are indicated.

4.3.5.3 Discussion of the Operating Conditions of the Data of Figs. 13 and 20b ($x_{in} \approx .20$ mm, $\rho_{00}/\rho_s \approx 95$).

First, the operating conditions $75 \leq \rho_0/\rho_s \leq 95$ will be discussed. The relevant parts of Fig. 22 are (a) and (b). For these conditions the light is injected over a relatively small range of nr values compared to the conditions with $x_{in} = -.16$ mm. As discussed in Section 4.3.1, the light will immediately begin to oscillate in the r -direction. However, because of the injection conditions the oscillations will be of modest amplitude. Hence, the light will penetrate only

a relatively small distance into the region of curved nr contours downstream of the nozzle exit. "Reflection" of the oscillating light from these relatively gently curved contours should cause a relatively inefficient generation of z oscillations from the initial r oscillations. This relative inefficiency of generation of z oscillations is believed to be responsible for the observed fact that ϕ_z is less than ϕ_r for $\rho_0/\rho_s \geq 70$ (Fig. 13b). The injection low in the well and the corresponding modest amplitude of the initial r oscillation is very likely responsible for the fact that ϕ_z and ϕ_r are well below the limiting curves of ϕ_{TE} and ϕ_w for $\rho_0/\rho_s > 75$ (Fig. 20b). The same factors, combined with the relatively inefficient generation of z oscillations, mean that initial order of the light in the well (i.e., the initial r oscillations) tends to be relatively well preserved as the light traverses the Venus Machine, and are likely responsible for the ordering in the r and z directions apparent in the divergence angle photographs. Photographs 23a and 23b are relevant to the present discussion. Fig. 23a shows two unequal spots elongated in the r-direction separated by a region of somewhat lower light intensity. Fig. 23b shows an almost rectangular output beam oriented along the r and z directions. The injection of the laser beam low in the light well, the correspondingly relatively modest amplitudes of the r and z oscillations (well below the limiting values of ϕ_{TE} and ϕ_w) and the fact that the light well extends considerably beyond the "diameter" of the input spot in all directions (see Section 4.3.5.1) combine to yield very favorable operating conditions under which transmission of the Venus Machine is very high, from .992 to .997.

The operating conditions $63 \leq \rho_0/\rho_s \leq 75$ will be discussed. The relevant part of Fig. 22 is (c); the photographs of Fig. 21 for $\rho_0/\rho_s = 74.1$ and 64.6 are also in this range. In this case the light tends to be injected considerably higher up in the well. Stronger r oscillations will immediately start. The light also will ride much further up into the region of curved nr contours downstream from the nozzle exit. "Reflection" from these strongly curved and inclined contours should cause a much more efficient generation of z oscillations from the initial r oscillations. Then behavior of the ϕ_r and ϕ_z data of Figs. 13b and 20b for $63 \leq \rho_0/\rho_s \leq 75$ reflects roughly the above discussion. There is much less tendency for ϕ_z to be less than ϕ_r , particularly allowing for the fact that the divergence angle photographs for $\rho_0/\rho_s = 72.5$ and 75 show faint light traces which, if included in the calculation of ϕ_z , would have made ϕ_z roughly equal to ϕ_r . These traces are not present for $\rho_0/\rho_s \geq 77.5$. If ϕ_z is considered to be roughly equal to ϕ_r for $\rho_0/\rho_s = 72.5$ and 75, then, in general, in the region of discussion, ϕ_r and ϕ_z tend to be much closer to the limiting curves (ϕ_{TE} or ϕ_w) than for conditions with $\rho_0/\rho_s > 75$. The ϕ_z data are essentially at the limiting ϕ_{TE} value for $63 \leq \rho_0/\rho_s \leq 67$.

The following should be noted at this point. For $x_{in} \approx .20$ mm, the light is initially travelling in the Venus Machine with strong oscillations in the r directions only. Oscillation energy is then transferred to oscillations in the z directions (from those in the r direction). With a very high efficiency of transfer, one would expect the oscillations to be of equal amplitude in the r and z directions, but the amplitude in the z direction would not be expected to be higher than that in the r direction. The data of Figs. 13b and 20b for $60 \leq \rho_0/\rho_s \leq 70$

would appear to contradict this. However, careful examination of faint wisps of light in these photographs indicate that the condition is not significantly violated. However, the ϕ_z and ϕ_r data were kept as originally plotted, that is, those angles within which a moderately strong exposure appears on the film. This points out, to a certain degree, the arbitrary nature of taking these sort of measurements off photographs. However, the investigators believe that even if a considerably different exposure intensity was taken to establish dimensions to be taken off photographs, the discussion and conclusions of this report would be unaltered. The following paragraph returns to the main discussion of this section.

The lowered transmission values for this range of ρ_o/ρ_s likely reflects the fact that, as ρ_o/ρ_s decreases some of the outlying energy of the laser beam begins to be injected outside the well on the upstream side. See especially Fig. 21.

The transmission decreases from .992 for $\rho_o/\rho_s = 75$ to .963 for $\rho_o/\rho_s = 63$. The stronger oscillations of the light in the well are also reflected in the more disorganized structure of the divergence angle photographs. A typical such photograph is shown in Fig. 23(c) for $\rho_o/\rho_s = 65$. The divergence angle photographs tend to show a somewhat filamentary character with individual filaments subtending angles as small as 0.5 degrees. It is believed that this filamentary structure may result from a kind of extreme extending and distortion of the initially compact laser beam as it undergoes repeated reflections from the highly curved nr contours downstream from the nozzle exit. The minimum angle subtended by the filamentary structure is roughly equal to the angle subtended by the input laser beam;

the latter angle is 0.7 degrees. This explanation for the filamentary structure is tentative, at present, however.

Finally, operating conditions $\rho_0/\rho_s \leq 63$ will be discussed. Of Fig. 22, (d) and (e) are now relevant, and of Fig. 21, all photographs in the appropriate ρ_0/ρ_s range. Under these conditions, as ρ_0/ρ_s is lowered, the upstream limit of the light well rapidly moves past the input laser beam and the transmission falls very steeply. T falls from .963 at $\rho_0/\rho_s = 63$ to .048 at $\rho_0/\rho_s = 55$. The ϕ_z and ϕ_r (Figs. 13b and 20b) values and the nature of the divergence angle pictures show, in general, little change as ρ_0/ρ_s decreases below 63 to the point of "photographic light well failure" - $\rho_0/\rho_s = 55$, at which point no exposure is detectable on the film. The apparent sharp decrease in ϕ_z and ϕ_r at $\rho_0/\rho_s = 57.5$ may be due simply to the very greatly decreased amount of light falling on the film, creating an image of which only the brighter inner regions are recorded. At $\rho_0/\rho_s = 60$, a faint tail extending in the direction of the tail of the light well is noted in the divergence angle photographs. The angular extent of this tail is well beyond the ϕ_{TE} and ϕ_w limits and is indicated by the ϕ_{TAIL} point in Fig. 13b and 20b. This phenomena will be discussed further in Section 4.3.6.

4.3.5.4 Discussion of the Operating Conditions of the Data in Figs. 12 and 20a ($x_{in} \approx -.16$ mm, $\rho_{00}/\rho_s \approx 95$).

First, the operating conditions $75 \leq \rho_0/\rho_s \leq 95$ will be discussed. (a) and (b) are relevant from Fig. 22 and the first two photographs from Fig. 21. The light is injected high up in the light well under these conditions, in contrast to the corresponding conditions for $x_{in} = .20$ mm. The light is also injected over a much larger range of nr values than is the case for $x_{in} = .20$ mm. The light will immediately begin oscillating strongly in both the r and z directions;

the latter because the light is injected in regions with large nr gradients in the z direction. Under these conditions, the magnitude of the oscillations in the r and z directions would be expected to be nearly equal, as is shown experimentally by the data of Figs. 12b and 20a. A typical divergence angle picture in this ρ_0/ρ_s range is shown in Fig. 23d. The output beam is diffused and roughly circular with little trace of the fine filamentation at Fig. 23c. With the light injected at high levels in the well, the well is essentially filled up to the limiting value, $\phi_{w,\Delta T}$. That is, ϕ_z and ϕ_r are roughly equal to $\phi_{w,\Delta T}$ in Figs. 12b and 20a. (As mentioned earlier in this report, for the higher values of ρ_0/ρ_s , the true ϕ_w curve should lie fairly close to the $\phi_{w,\Delta T}$ curve.) Since the edge of the central region of the input laser beam (the circles in Fig. 22) are quite close to the light well limits, a considerable portion of the light in the outlying portions of the beam is not trapped in the light well and is lost. Hence, the transmission of the Venus is relatively low (.91 - .95) compared to the corresponding conditions with $x_{in} = .20$ mm ($T > .99$).

There are two apparent disagreements in the experimental data which should be noted at this point.

- (a) Divergence angle photographs at $x_{in} = -.16$ mm, $\rho_0/\rho_s = 80 - 95$ (injection high in light well) show little or no filamentation, while photographs at $x_{in} = .20$ mm, $\rho_0/\rho_s = 57 - 72$ (injection also high in light well) show filamentation.
- (b) Divergence angle photographs at $x_{in} = -.16$ mm, $\rho_0/\rho_s = 80 - 95$ (injection high in well) indicate a very symmetrical output beam, with $\phi_r \approx \phi_z$, while for $x_{in} = .67$ mm, $\rho_0/\rho_s = 85 - 95$ (also injection high in well), transmission and photographic data indicate that ϕ_r is substantially larger than ϕ_z (see Section 4.3.1).

Discussion of these points will be made with some reference to Figs. 22a through 22d. The data suggest that injection high in the light well on the upstream slope can cause considerable ordering to be shown in the divergence angle photographs (or implied by other data). In the cases mentioned, either filamentation or ϕ_r considerably greater than ϕ_z . On the other hand, injection high in the light well on the downstream slope appears to generate relatively disordered divergence angle photographs ($\phi_r \approx \phi_z$, little or no filamentation). It is believed that these differences may be related to the fact that light injected high in the light well on the downstream slope will immediately start oscillating strongly in the z direction as well as in the r direction. Referring to Fig. 22, some of the light from the input beam will move in the positive z direction, some in the negative z direction and some only in the r direction (the light which moves in the +ve and -ve z directions also moves in the r direction). The rapid distortion of the input beam implied by these varied z -motions may be connected with the lack of structure of the divergence angle photographs for conditions with injection high in the well on the downstream slope. The light injected high in the well on the upstream slope will initially begin to move in a well organization fashion almost solely in the r - direction. However, after crossing the well, this light will enter the region of strongly curved nr contours, and it is not clear that the disorganization of the light on "reflection" will be less than the initial disorganization of the light injected high on the downstream side, though this may, in fact, be the case. It is believed that organizational differences of the divergence angle (or implied divergence angle) data discussed in this paragraph are related to the mechanisms presented herein but, on account of the uncertainties, this must remain tentative at present.

Operating conditions with $63 \leq \rho_0/\rho_s \leq 78$ will now be discussed. Fig. 22c and the photographs for $\rho_0/\rho_s = 64.6$ and 74.1 of Fig. 21 are relevant. For these conditions, the light starts out somewhat lower in the light well than for $\rho_0/\rho_s > 78$. Also, the central region of the input laser beam is somewhat farther removed from the limits of the light well [cf. (c) Fig. 22 with (b) and (a)]. Hence, the transmission is somewhat higher than for $78 \leq \rho_0/\rho_s \leq 95$ (.947 to .955 versus .910 to .947). However, the input beam is still not nearly as well contained in the well as for conditions with $x_{in} \approx .20$ mm and $75 \leq \rho_0/\rho_s \leq 95$ and the very high transmissions of the latter ($>.99$) are not approached.

For conditions with $x_{in} \approx .20$ mm and $75 \leq \rho_0/\rho_s \leq 95$ (Section 4.3.5.3), ϕ_r and ϕ_z were substantially below the ϕ_w and ϕ_{TE} limits and $T > .99$. For this case, clearly by far the greater fraction of the light of the input laser beam is trapped well inside the input well. In contrast, for the present conditions, $T \approx .95$ and ϕ_z and ϕ_r are considerably closer to, but still below, the ϕ_{TE} and ϕ_w limits. However, there is some apparent disagreement among the experimental data. The transmission data indicates that 5% of the light is injected above the light well limits and lost, while the divergence angle data would appear to indicate that all of the input should be transmitted since all of it is below the limiting values of ϕ_w and ϕ_{TE} . The apparent disagreement is not believed to have any significant effect on the discussions of this report and may be due to one or more of the following factors:

- (a) The divergence angle and transmission data were taken under slightly different operating conditions.

(b) On the divergence angle photographs, a small amount of light can be noticed out to angles slightly larger than the values of ϕ_z and ϕ_r recorded in Figs. 12b and 20a. Inclusion of this light in the determination of ϕ_z and ϕ_r would render these values closer to ϕ_{TE} and ϕ_w .

In the range of the highest transmission values ($65 \leq \rho_0/\rho_s \leq 70$), the divergence angle photographs show organization along the r and z directions similar to, but not as strong as that for, $x_{in} \approx .20$ mm, $\rho_0/\rho_s = 90 - 95$ (Section 4.3.5.3). Fig. 23e shows a divergence angle photograph for $\rho_0/\rho_s = 67.5$. The photograph has some similarity to that for $x_{in} \approx .20$ mm, $\rho_0/\rho_s = 95$ (Fig. 23a), showing again two spots elongated in the r direction, separated (for the most part) by a region of lower light intensity. As is the case for $x_{in} \approx .20$ mm, the strongest organization of the divergence angle photograph in the r and z directions is associated with the highest transmissions of the Venus Machine.

In discussing operating conditions with $53 \leq \rho_0/\rho_s \leq 63$ Fig. 22d and the photographs of Fig. 21 for $\rho_0/\rho_s = 55.4$ and 59.7 are relevant. The transmission values are lower than for $63 \leq \rho_0/\rho_s \leq 78$, ranging from .924 to .947. The divergence angle photographs no longer have the structuring along the r and z directions. As ρ_0/ρ_s decreases, ϕ_z and ϕ_r increase until they are roughly equal to ϕ_{TE} at $\rho_0/\rho_s = 61$ and then follow the ϕ_{TE} curve as ρ_0/ρ_s decreases further.

Conditions below $\rho_0/\rho_s \leq 53$ show that the well decreases very rapidly in extent in both the r and z directions and the transmission falls very steeply, dropping from .900 at $\rho_0/\rho_s = 52$ to .091 at $\rho_0/\rho_s = 48$. Fig. 22e and the photographs of Fig. 21 for $\rho_0/\rho_s = 50.1$ and 43.9 are relevant.

4.3.6 Photographically Indicated Extension of Light Beyond the Downstream Limits of the Light Well.

Reference will be made of the Figs. 11, 12, and 13. When the light injected into the Venus Machine is in the form of a narrow beam for certain ρ_0/ρ_s values, the light well photographs indicate a substantially greater "light well" extent than those photographs taken with the input window of the Venus Machine flooded with light. (The latter photographs have been shown to give a picture of the true extent of the light well.) This phenomena occurs for $x_{in} \approx -.16$ mm, $45 \leq \rho_0/\rho_s \leq 55$, and for $x_{in} \approx .20$ mm, $55 \leq \rho_0/\rho_s \leq 72$ (compare Figs. 11, 12a and 13a). For $x_{in} \approx .20$ mm, $55 \leq \rho_0/\rho_s \leq 62$, and $x_{in} \approx -.16$ mm, $45 \leq \rho_0/\rho_s \leq 55$, the phenomena are clearly associated with light in the process of being lost from the light well and, in fact, outside the limits of the light well. The fact that the light is in process of being lost is supported by the transmission data (Figs. 12c and 13c) which indicate a very steep drop in transmission in the ρ_0/ρ_s ranges of interest. Further, the divergence angle photographs show long tails extending well beyond the maximum tolerance angles of the light well. A typical such divergence angle photograph is shown in Fig. 23c. The angular extent of these tails are indicated in Figs. 12b and 13b. For $x_{in} \approx .20$ mm, only one photograph shows a tail.

4.3.7 Scattering of Light in the Venus Machine

In Section 3.4, three types of random density perturbations were discussed which might cause scattering of light within the Venus Machine. These three types were:

- 1) Density perturbations in the free stream flow in the light well region which are caused by residual temperature and pressure perturbations carried downstream from turbulence producing regions in the approach flow system.

- 2) Density perturbations in the free stream flow in the light well region caused by acoustic noise radiation from the boundary layers.
- 3) Density perturbations in the boundary layer in the light well region due to pressure and temperature fluctuations.

Experimental estimates of the maximum random scattering angle of the Venus Machine were made as follows. The filamentary structure of the divergence angle photographs noted in Section 4.3.5.3 for $63 \leq \rho_o/\rho_s \leq 75$ (e.g., Fig. 23c) would be expected to be destroyed for random scattering much greater than half the width of the filaments. The filaments typically are of width 0.5 degrees, leading to a rough estimate of the maximum scattering angle of the Venus Machine of 0.25 degrees. The input laser beam subtends a half-angle of .35 degrees. Thus, the fine structure observed in the output beam subtends roughly the same angle as the input beam. This suggests that random scattering in the Venus Machine may be quite low, perhaps 0.1 - 0.2 degrees or less, and much less than the typical half angle subtended by the entire output beam (typically ~4 degrees). Further work is required to settle the question of the random scattering angle of the Venus Machine.

4.3.8 Comparison of Data for $\rho_{oo}/\rho_s \approx 68$ with that for $\rho_{oo}/\rho_s \approx 95$.

All of the data discussed in Section 4.3 up to this point (with the exception of the 1974 transmission data) was taken with $\rho_{oo}/\rho_s \approx 95$. For $x_{in} \approx -.16$ mm, light well and divergence angle photographs and transmission data were also taken with $\rho_{oo}/\rho_s \approx 68$. For $x_{in} \approx .20$ mm, transmission data only was taken for $\rho_{oo}/\rho_s \approx 68$. The data for corresponding ρ_o/ρ_s values is compared below. Because data for $\rho_o/\rho_s > 68$ is not available from a test run with $\rho_{oo}/\rho_s \approx 68$, the comparison is limited to $\rho_o/\rho_s \leq 68$. The photographic data (light well and beam divergence photographs) were almost identical for $\rho_{oo}/\rho_s = 68$ and 95. The

transmission data in each pair of data curves were very similar to each other; however, the rapid fall-off of transmission occurred at slightly lower values of ρ_0/ρ_S for $\rho_{00}/\rho_S \approx 68$. There would appear to be no reason why the performance of the Venus Machine should be slightly worse at $\rho_{00}/\rho_S \approx 95$ than at $\rho_{00}/\rho_S \approx 68$, as indicated by the transmission data, except for the scattering effects of density perturbations. Of the 3 causes of density perturbations given in Section 4.3.7, the first and third are clearly dependent on the difference between the gas reservoir temperature and the temperature of the Venus Machine. Since this temperature difference is larger, for example, for a $\rho_0/\rho_S = 60$, $\rho_{00}/\rho_S \approx 95$ run condition than for a $\rho_0/\rho_S = 60$, $\rho_{00}/\rho_S \approx 68$ run condition, the density perturbations and the attendant scattering of light in the light well would be expected to be larger for a $\rho_{00}/\rho_S \approx 95$ test run than for a $\rho_{00}/\rho_S \approx 68$ test run at the same ρ_0/ρ_S value. This effect may be responsible for the slightly poorer performance of the light well (at the same ρ_0/ρ_S value) for $\rho_{00}/\rho_S \approx 95$ as compared to that at $\rho_{00}/\rho_S \approx 68$.

4.4 Transmission Data

Most of the discussion of this report involves detailed analyses of transmission data along with divergence angle and light well photographic data; only a few remarks are called for which refer mainly to transmission data alone; they will be given here.

In the comparison of the photographic data with the transmission data for a given x_{in} , the relative transmission was estimated very crudely from the photographs in the region of rapid fall off of the transmission with

decreasing ρ_0/ρ_s . These crude estimates were found to agree very well in all cases with the transmission data, giving a check on the consistency of the experimental procedures.

4.4.1 Data at High Transmission Conditions; Accuracy and Reproducibility.

Fig. 24 shows 1976 transmission data for 4 test runs with $x_{in} \approx .20$ mm. As mentioned in Section 4.3.1, for $\rho_0/\rho_s < 78$, the data is suspect because of condensation of moisture on the outsides of the Venus Machine windows. However, for $\rho_0/\rho_s \geq 78$, the data is valid. These runs were taken to investigate high transmission conditions in the light well, and to check the reproducibility and accuracy of the experimental methods. The reproducibility indicated by Fig. 24 for $\rho_0/\rho_s = 80$ is $\pm .010$ in the value of T ; i.e., $T(\rho_0/\rho_s = 80) = .990 \pm .010$. The reproducibility will be discussed further after estimate is made of the accuracy of the transmission measurements. Estimated errors in the determination of T are given below:

Error in determining the transmission of the reference	
prism (see Sec. 2)	$\pm .002$
Error in reading the data off oscilloscope pictures	$\pm .001-.002$
Errors due to possible interference effects in the	
input and output windows (see Sec. 2)	$\pm .0025$
Error due to inaccuracies in the gains of the recording	
oscilloscope (not measurable)	<u>0</u>
Total estimated error in or accuracy of T values	$\pm .0055-.0065$

The maximum transmission value shown in Fig. 24 is 1.0026; the obvious minimum error in this value is .0026, well within the estimated error limits given above. The differences among the 4 curves of Fig. 24 indicate that the reproducibility of the T data is considerably larger than the error estimate. The relatively large reproducibility of $\pm .010$ is almost certainly due to the great sensitivity of the light well performance to the exact x and z-positions of the input laser beam. It has been repeatedly observed that movements of the input laser beam position, particularly in the z-direction, which are as small as .050 mm can produce substantial changes in the transmission. On the other hand, the accuracy in setting and measuring the input beam position is limited to $\pm .02$ mm. Hence, a certain amount of variability in the measured transmission values is to be expected. It should be noted that runs 1 and 4 in Fig. 24 were taken with x_{in} differing by .054 mm. Hence, the transmission data of Fig. 24 should be regarded as taken at 4 slightly different operating conditions. However, for any one of these test runs, the transmission values have the estimated accuracy given previously.

Considering runs 2 and 4 in Fig. 24, the maximum measured transmission is $1.000 \pm .0065$ or, more conservatively, $1.000 \pm .010$. Since the transmission cannot be greater than unity, this last figure could be written as $T(\max) = .995 \pm .005$.

The data of 1976 is confirmed (for $\rho_0/\rho_s > 78$) by the 1977 data of Fig. 14 for $x_{in} \approx .20$ mm. The 1977 data indicates a transmission of .991 at $\rho_0/\rho_s = 95$ rising to .997 at $\rho_0/\rho_s = 80$, in excellent agreement with runs 2 and 4 of Fig. 24.

5. ADDITIONAL REMARKS

Many of the foregoing conclusions reflect points of detailed understanding of the operation of the Venus Machine, and it is not appropriate to attempt to summarize them in this section. However, several conclusions judged to be of more general interest are given below.

(1) The operation of the existing 90° Venus Machine is fairly well understood, although there are still points on which further work needs to be done.

(2) The Venus Machine can operate at transmissions greater than .990, and possibly very close to unity (Section 4.4.1).

(3) Certain data suggest that the random angular scattering in the Venus Machine may be quite low, 0.1 to 0.2 degrees or lower (Section 4.3.7).

(4) The relatively large size of the output beam of the Venus Machine (typically about 4 degrees half angle) is due to two sets of causes.

- (a) Manufacturing and mounting errors, i.e. misalignment of the two nozzle blocks, rounding of the corners at the nozzle exit, and possibly tool marks.
- (b) Even if the errors of (a) were to be removed, the following remains. The light well is generally of an inferior shape to direct the beam. It is difficult to avoid r oscillations of significant strength, even if

the location of the input beam is very carefully selected. The shape of the light well downstream from the nozzle exit is poor, generally tending to generate strong z oscillations of the beam.

(5) Points 2,3 and 4 above indicate that potential exists for the design and construction of 90° and 360° Venus Machines of much higher performance and optical quality.

6. RECOMMENDATIONS FOR FUTURE LOW POWER RESEARCH ON THE 90° VENUS MACHINE

(1) The poor mechanical quality of the existing Venus Machine limits the amount of work which it would be profitable to undertake on it. However, it would be desirable to take divergence angle photographs at $\rho_0/\rho_s \approx 90$, $x_{in} \approx .10$ mm (see Fig. 22a). Under these operating conditions light would be injected at the very bottom of the light well, and very low values of ϕ_r and ϕ_z might be obtained, which would provide some degree of confirmation of the data which suggest that the random angular scattering of the Venus Machine is very low (Section 4.3.7). Even if the ϕ_r and ϕ_z values are not much lower than those presented in this report, the random scattering of the Venus Machine is not proven necessarily to be high; the manufacturing errors in the Venus Machine may be responsible for raising ϕ_r and ϕ_z well above the random scattering level.

(2) The simplest recommended modification of the Venus Machine would be as follows. The nozzle blocks would be removed and refinished to remove, as much as possible, rounding of the corners at the nozzle exit. The nozzle blocks would then be remounted, with careful attention to alignment, somewhat closer together. The nozzle exit gap would be set at approximately 0.30 mm

instead of the former 0.40 mm. In operation with these nozzle changes, the light well will look roughly as sketched in Fig. 25a for $\rho_0/\rho_s \approx 90$. The nr versus r profile along the centerline is also roughly sketched in Fig. 25a. It is noted that light, on injection into the well (at a low level), can oscillate with a moderate amplitude in the r direction without encountering the curved nr contours downstream from the nozzle exit which tend to generate z oscillations. Under this type of operating conditions the beam leaving the Venus Machine may well have very low ϕ_z values although ϕ_r would not be exceptionally small. If this was, in fact, observed, the postulated low random scattering angle of the Venus Machine would tend to be confirmed.

(3) It is recommended that the channel for the flow approaching the light well region of the Venus Machine be modified to reduce the amount of turbulence which will be convected to the light well. The designs for these modifications have been made and some of the parts have been constructed. The remaining parts should be constructed and the improved flow channel components installed.

(4) Depending on the results obtained from (1) and (2) above, it may be desirable to test the set of nozzle blocks of the shape sketched roughly in Fig. 25b. The changes in slope of the nozzle walls indicated in the sketch can readily be shown to modify the light well shape and the centerline $nr - r$ curve as shown (for $\rho_0/\rho_s \approx 90$). The bottom of the light well and the $nr - r$ curve are flattened. If the input laser beam is injected as indicated, oscillations in both the r and z directions

should be very small, and it would appear possible, depending on the random scattering angle of the Venus Machine, to achieve a very low output beam angle in both the r and z directions. It is probably advisable, on account of the greater manufacturing difficulty for these nozzle blocks, to perform the experiments indicated in (1) and (2) first.

(5) The types of light wells shown in Fig. 25a and 25b and those discussed in the body of this report suffer from the following two disadvantages.

- (a) The light well makes use of boundary layers for stabilization in the z -direction; this can introduce unnecessary scattering into the light ray paths due to density perturbations in the boundary layer.
- (b) The optical quality of the light well as compared to a glass index gradient fiber optic is very poor since the nr profiles across the light well in the r and z directions are far from being parabolas equal to each other. This latter, stated in a simplified way, is the requirement for an imaging quality light guide.

If the work suggested in (1) to (4) gives good results, it is recommended that the nozzle blocks similar to those sketched roughly in Fig. 25c be constructed. The nr contours sketched in Fig. 25c were taken from Reference 5. It is noted that this light well does not depend on the boundary layers for stabilization in the z direction. This light well, while having an nr surface much closer in shape to the paraboloid of revolution of an ideal index gradient glass fiber than the light wells stabilized in the z direction by

the boundary layer, still has substantial assymetry. It is therefore also recommended that small modifications of the nozzle wall shapes of Fig. 25c be made (on paper) and the nr versus r and z contours be calculated by computer. The investigators believe that an nr surface much closer to the ideal paraboloid of revolution could be achieved. The nozzle profile yielding this best nr surface should be then built and tested. For a perfect paraboloidal light well with nr versus r (or z) gradients similar to those shown in Fig. 25c, for $\lambda \approx .633$ nm, the size of the TEM_{00} mode is ~ 0.08 mm, indicating that the input laser beam could be well coupled to the input well in the available space. The coupling could probably be made fairly satisfactorily with the real light well, which would not be perfectly symmetrical.

7. HIGH POWER EXPERIMENTS ON THE 90° VENUS MACHINE

The experiments described up to this point were done using a 1 mW He-Ne laser as the light source. When focused down at the input window of the Venus Machine, this laser provides a power density of ~ 10 w/cm². To investigate the high power transmission characteristics of the Venus Machine, the ruby laser shown in Fig. 26 was constructed. This laser produces a .015 J. pulse of 40 ns duration. The beam can readily be focused down to $\sim 125 \mu$, suitable for injection into the Venus Machine. Using the ruby laser, the transmission of the Venus Machine at power densities up to 10^9 w/cm² will be investigated. The experimental set up is shown in Fig. 27. The set up is very similar to those shown in Fig. 1 and used for low power measurements. The attenuators shown allow the transmission of the Venus Machine to be investigated at power densities of 10^6

to 10^9 w/cm². The light is detected by silicon photocells which act as passive integrators of the energy of the laser pulse. Preliminary tests have shown the cells to be linear to within $\pm 1\%$. The operation of the apparatus will be as follows. Several shots will be taken using the calibrated reference prism to deflect the light. This establishes the ratio between the output pulses of the photodetectors 1 and 2 which corresponds to the known prism transmission. One or more shots will then be taken at the desired Venus Machine operating condition. From the ratio of the output pulses of the two photodetectors, the Venus Machine transmission can readily be calculated.

Unfortunately, several problems were experienced in building and testing out the detection system. Initially, very fast PIN photodiodes were used as the detectors, since they would have permitted one to follow the actual nanosecond laser pulse. After several months' work, however, it was concluded that the electronics associated with the photodiodes was not capable of yielding the desired accuracy of $\pm 1\%$. Silicon photocells acting as passive integrators were then substituted for the PIN photodiodes. Also, stray ruby light, such as reflections off the ceiling, was reaching photodetectors 1 and 2 as they were originally mounted, preventing consistent results from being obtained. By mounting the photodetectors inside light-tight boxes, this problem was eliminated. These problems and others have delayed the high power measurements considerably. We believe that the high power measurements will be started soon.

8. THE ELECTRICAL DISCHARGE

8.1 Aerodynamics of E-beam Sustained Discharges in Supersonic Flow

The electric glow discharge in supersonic flow presents a fascinating array of complex aerodynamic problems. At present the most important use of this discharge system is the case of high power CW electric lasers, of which the CO system promises to be the most efficient. In this case, a transverse electrical discharge excites a large volume of gas in the supersonic section, and a population inversion builds up in the direction of flow until lasing can take place. As laser radiation is extracted, the vibrational population is reduced, and the waste gas may be discharged through a suitable diffuser to the atmosphere.

The electrical discharge laser has basic flow problems that are very different from those associated with gas-dynamic lasers. Firstly, supersaturated mixtures and condensation may be a problem if cryogenic temperatures are used. At these low temperatures, too, any heat addition to the flowing gas stream creates large relative changes in temperature, affecting the performance of the laser. In addition, there are large losses in total pressure of the system that may affect the ability to complete diffuse the flow to the atmosphere. Then too, the electric power density loading of a high power laser discharge is limited by many physical problems, not the least of which may be a plasma instability. In the case of supersonic flows, the discharge problem may manifest itself earlier in a number of complex ways and be brought on by the flow features themselves. High power loading, which is desirable for high efficiency operation, can lead to a glow to arc transition, completely stopping the laser operation. The fundamental basis for possible deleterious interaction of the flow and discharge is the objective of this research.

8.2 The Supersonic Flow Facility and Discharge Apparatus

The flow facility that can stimulate in a satisfactory way the discharge characteristics of large scale laser discharge facilities was recently completed.

Basically, in this setup, the flow and discharge characteristics of a large scale electric laser can be tested, using a combination of long duration plus flow and electric discharges. Figure 28 is a drawing of the facility showing some of the important elements. A 6" diameter Ludwig tube provides the flow of gas required for the discharge. It is capable of storing gas at up to 300 psia. The gas is expanded through a conventional 2-D nozzle system which at present gives rise to a flow cross section of 4 cm x 20 cm. A $M = 3.5$ nozzle can be seen in Figure 28. After completion of the facility the flow duration and quality were examined, using pressure gauges and double pulse laser holographic interferometry. Figure 29 shows a typical pressure history for the test section on a time scale of 1 msec/dm. After an initial transient of 2 msec duration the pressure becomes nearly constant giving a testing time in excess of 8 msec. The Mach number of the flow was measured in Ar-N₂ mixtures and found to be $M = 3.2 \pm 3\%$ in agreement with calculations. Figure 30 shows a typical laser holographic interference photograph from which this was measured.

The discharge is located in the supersonic channel and is stabilized by an e-beam. This e-beam is produced by a plasma diode 6" in diameter and capable of being operated at up to 150 kV. The system has operated at voltages as high as 135 kV in tests. The duration of the discharge and e-beam current can be easily controlled. Time duration from 10 μ sec to

many times the transit time of a particle through the discharge can be obtained. The apparatus can supply e-beam current with a duration in excess of six times this transit time scale (transit time order of 50 μ sec) with a corresponding voltage drop of no more than 10% on the diode. At lower current densities longer time scales are possible, perhaps considerably in excess of 1 msec. A typical e-beam current and voltage trace is given in Figure 31. Both the input current to the diode and e-beam output are shown. As can be seen, the output is only a fraction of the input current, typical of plasma diodes. Nevertheless, current densities from 1 ma/cm² to 30 ma/cm² have been measured from the diode without foil failure. These current densities are somewhat higher than contemplated CW or high repetition rate systems. Higher electron densities and therefore higher sustainer current are available to pump the system more rapidly. The gas energy content will be scaled properly, of course, allowing a shorter discharge in the flow direction and more two-dimensionality in the flow. Furthermore, the higher current densities of the plasma diode, in comparison to the thermionic gun, alleviate much of the problem of dissociative attachment caused by low concentration (ppm) impurities that plague so many of the low current devices.

A high energy capacitor bank was built for the sustainer. Sustainer currents in excess of 400 amp. are possible for the testing time with a minimal (10%) voltage drop. The characteristics of the e-beam sustainer system are shown in Figure 32. Delay circuits make it possible to independently turn on and off both e-beam and sustainer currents. In this way

testing times for the most uniform conditions may be chosen. At the highest e-beam current levels, power densities in the discharge are in excess of 10^7 w/liter-amagat.

Early interferograms showed severe heating of the gas near the electrode edges. This is a result of high field strength at the edges of the finite electrodes and the concentration of current there as well. Clearly observed cathode fall heating and the cathode shock wave may be seen in Figure 33. It is believed that this information can be directly used to help evaluate phenomenon in the flowing case.

Preliminary measurements have also shown some of the effects of discharge heating in supersonic flow. Figure 34 shows the effect of cathode fall resulting in a thickening of the boundary layer and standing oblique wave emanating from the leading edge of the cathode.

REFERENCES

1. "A Fluid Mechanical Refracting Gas Prism Applicable to Laser Technology," AFOSR #74-2650, Annual Progress Report, 1 January 1976 - 31 December 1976, Aerospace & Energetics Research Program, University of Washington, Seattle, Washington, April 1977.
2. "A Fluid Mechanical Refracting Gas Prism Applicable to Laser Technology," AFOSR #69-1723H, 4th Annual Progress Report, 15 Jan. 1973 - 1 Jan. 1974, Aerospace Research Laboratory, University of Washington, Seattle, Washington, March 1974.
3. "A Fluid Mechanical Refracting Gas Prism Applicable to Laser Technology," AFOSR #74-2650, Annual Progress Report, 1 January 1974 - 31 December 1974, Aerospace Research Laboratory, University of Washington, Seattle, Washington, April 1975.
4. Schall, Wolfgang, "A New Method for Bending and Storing of Light Rays," Thesis, Dept. of Aeronautics and Astronautics, University of Washington, 1969.
5. Frederick, Walton Eugene, "A Fluid Mechanical System for the Storage or Deflection of a Laser Beam," Thesis, Dept. of Aeronautics and Astronautics, University of Washington, 1971.
6. Gantet, Claude Alain, "Study of the Trapping of Light by the Venus Machine," Thesis, Dept. of Aeronautics and Astronautics, University of Washington, 1973.
7. Dunn, Michael Joseph, "Analysis and Design of Gasdynamic Lightguides," Thesis, Dept. of Aeronautics and Astronautics, University of Washington, 1974.
8. Uchida, J., et.al., "Optical Characteristics of a Light Focusing Fiber Guide and its Applications," IEEE Journal of Quantum Electronics, Vol. QE-6, No. 10, Oct. 1970, pp. 606-612.

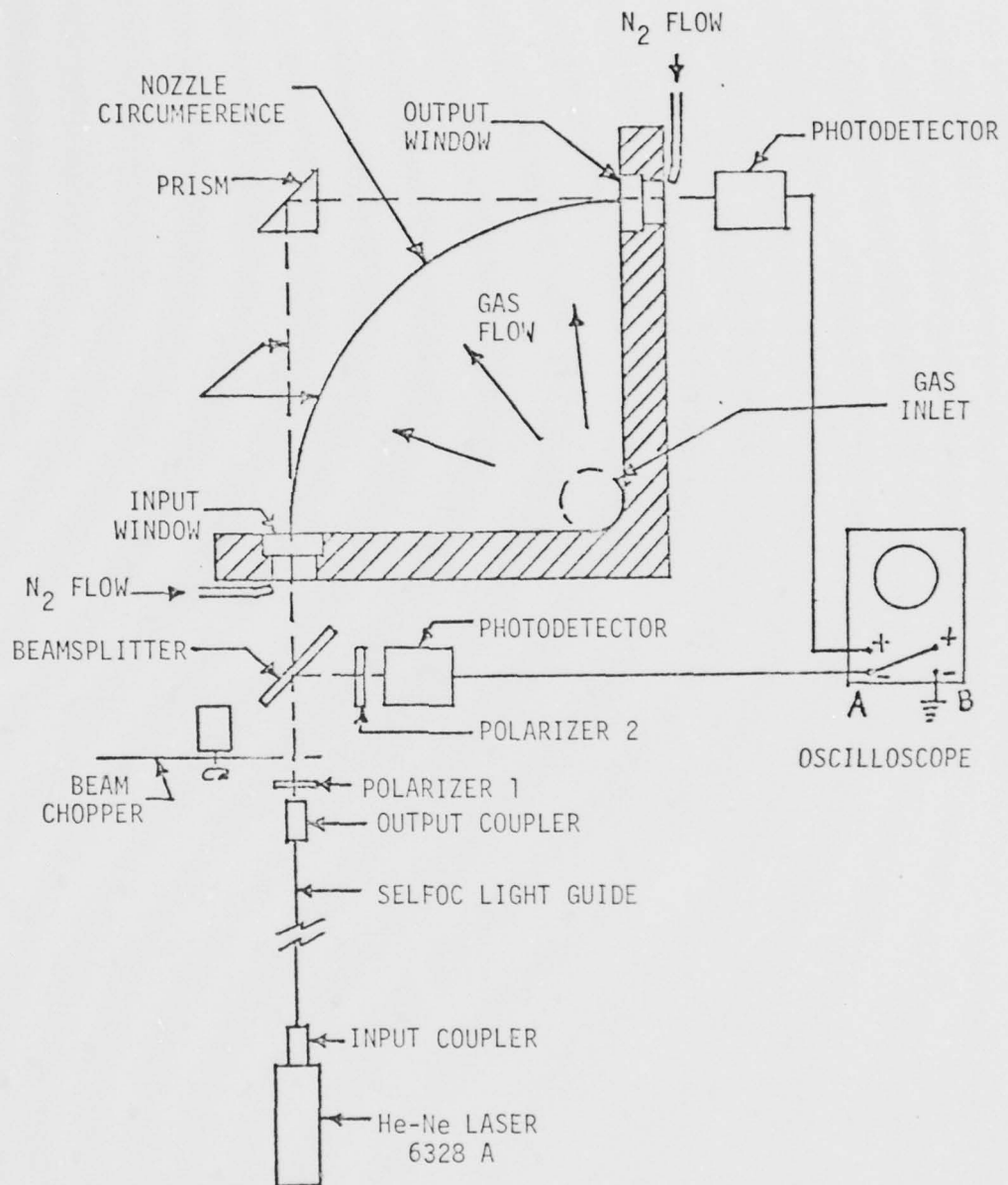


Figure 1
Experimental setup for beam transmission measurements in the 90° Venus Machine.

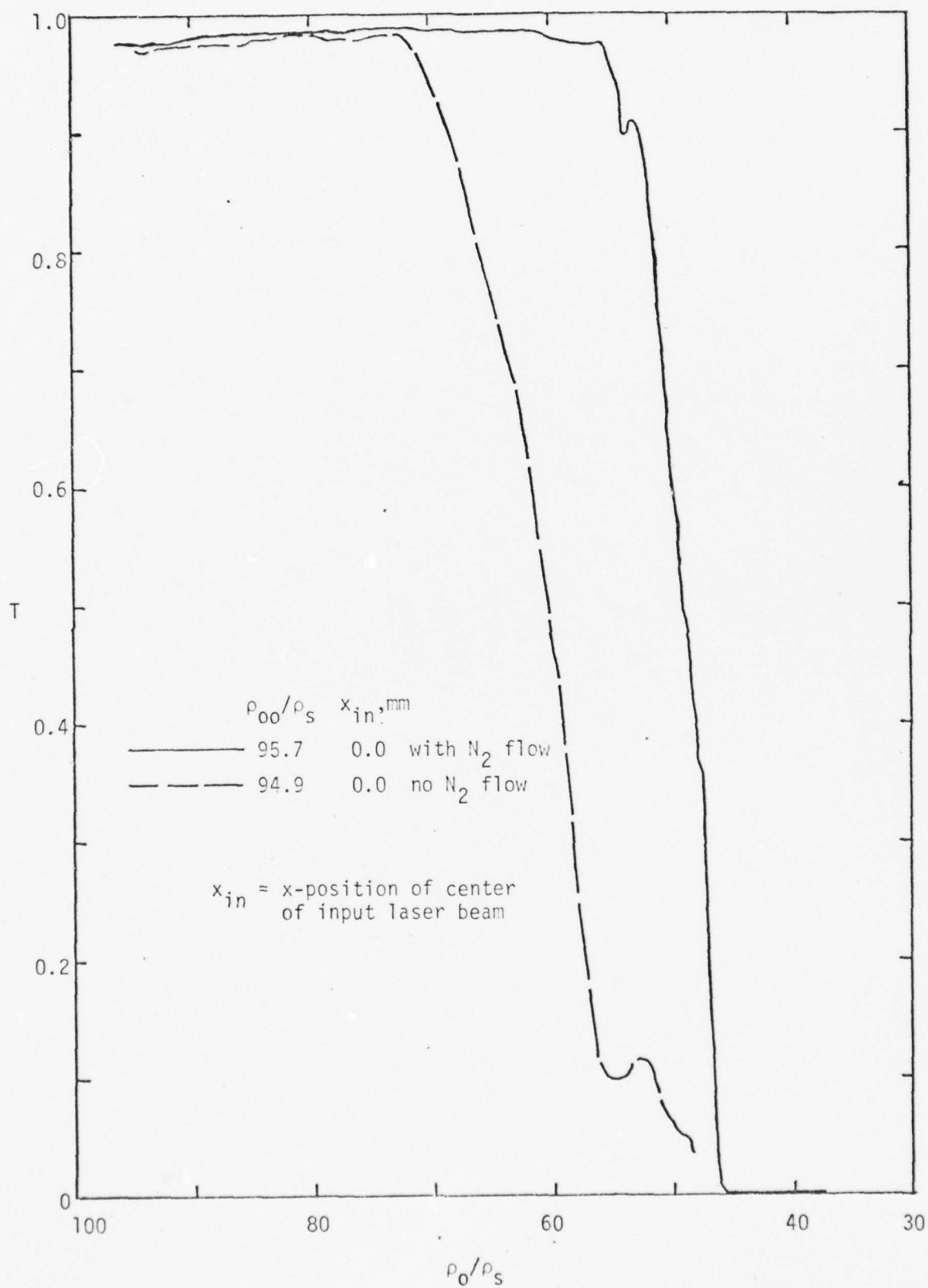
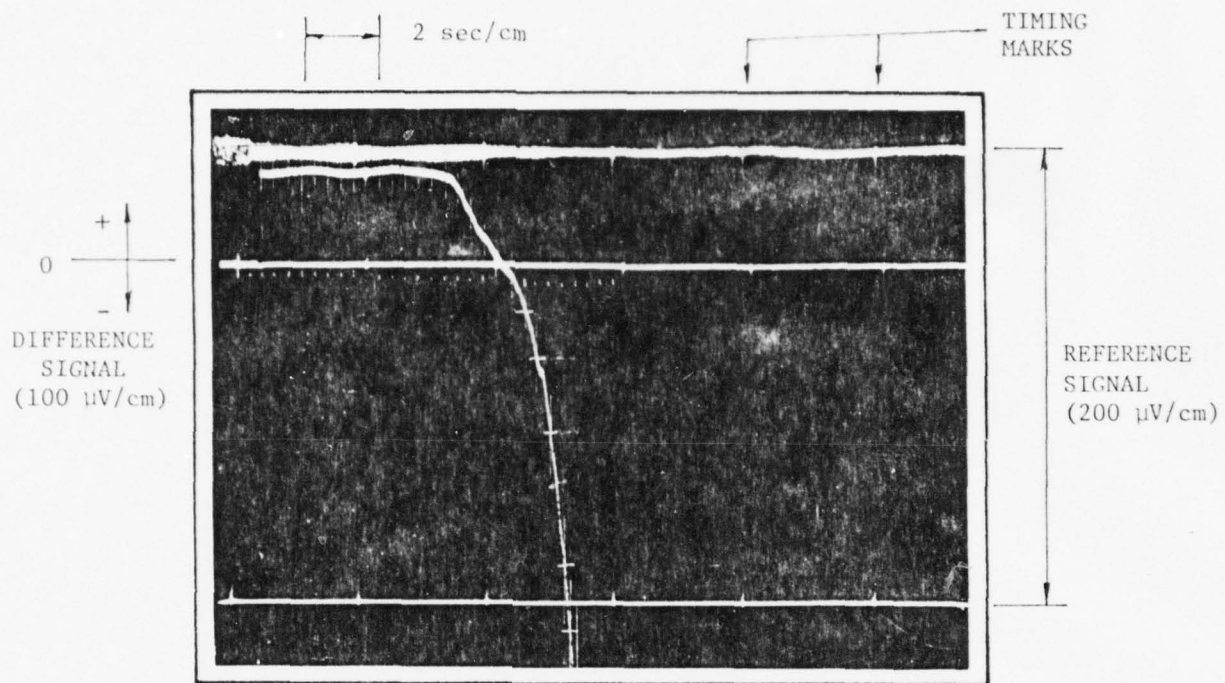
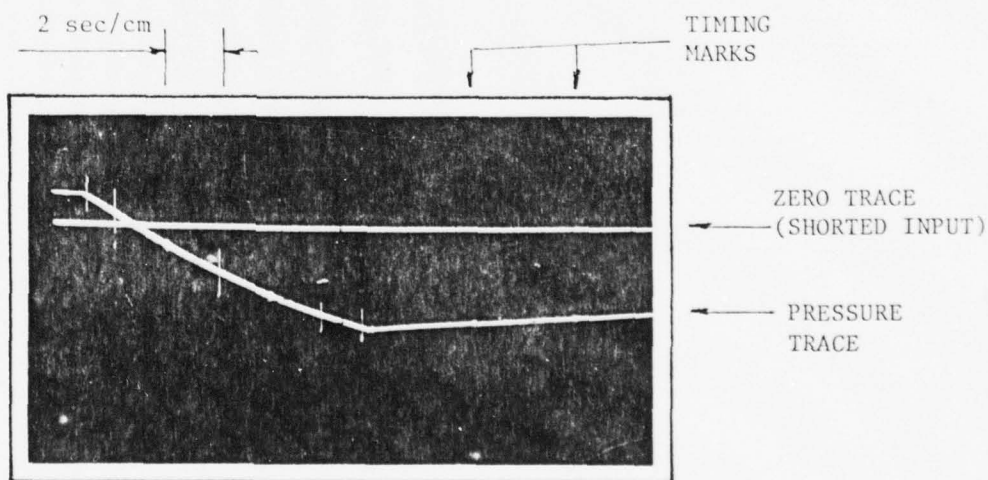


Figure 2.
 Transmission data for $x_{in} = 0.0 \text{ mm.}$, $\rho_{00}/\rho_s \approx 95$



TRANSMISSION DATA



RESERVOIR PRESSURE DATA

INITIAL STAGNATION PRESSURE = 1505 psia

INPUT LASER BEAM POSITION = .206 mm UPSTREAM OF NOZZLE EXIT

Figure 3 Typical data pictures for transmission measurement on the 90° Venus Machine.

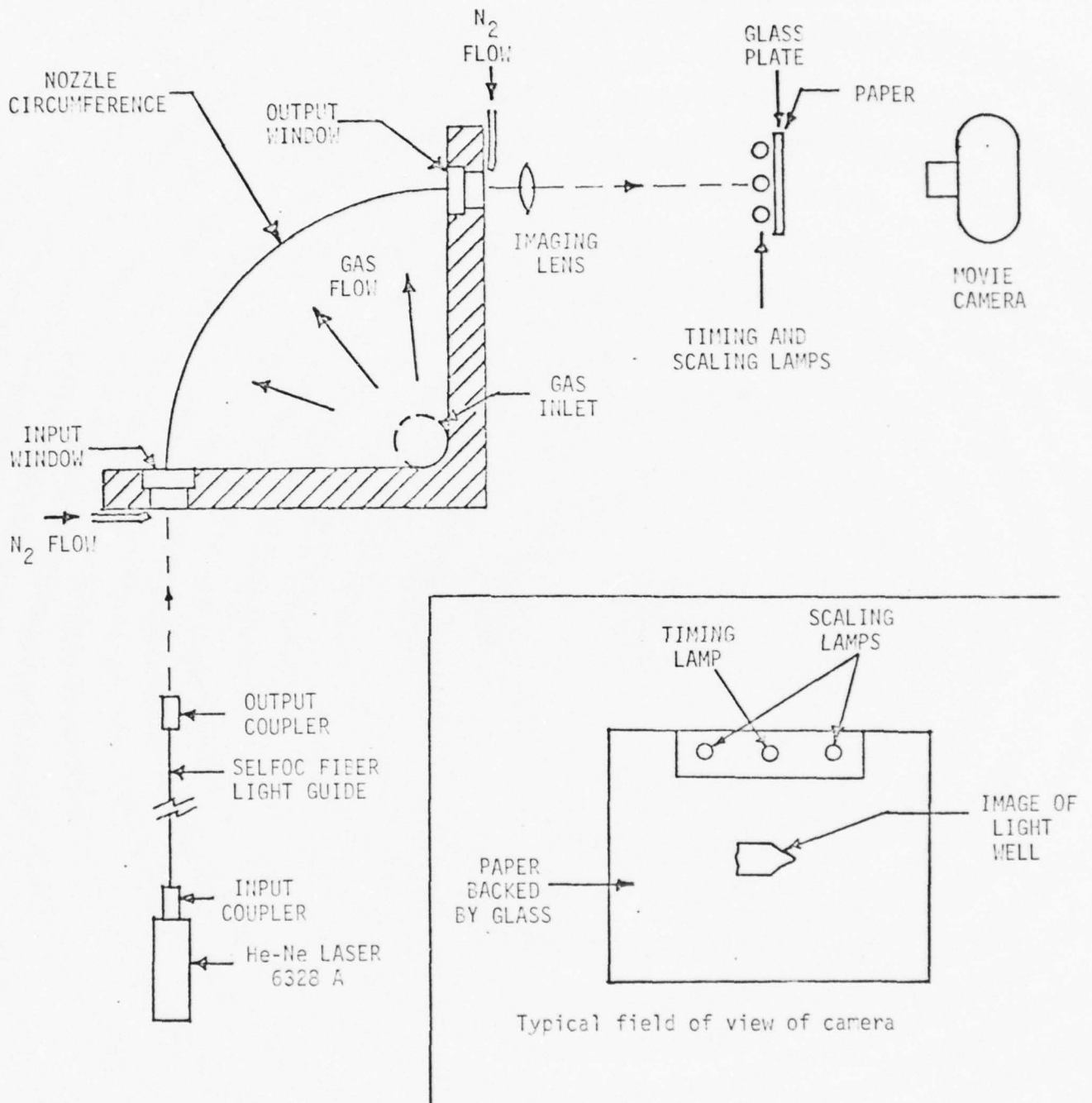
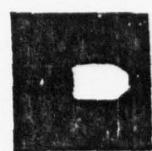
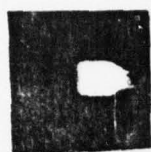
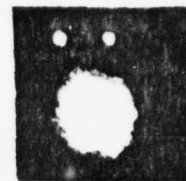


Figure 4
Experimental setup for photographing the shape of the light well and the divergence angle of the output beam.

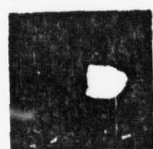
ρ_0/ρ_s



90



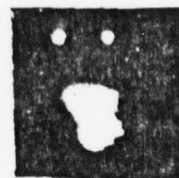
80



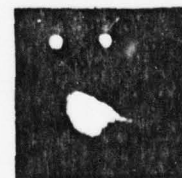
67.5



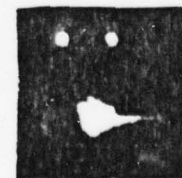
60



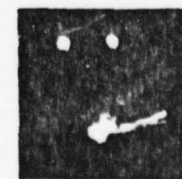
52.5



50



47.5



$\rho_{00}/\rho_s = 95.4$

$x_{in} = -.17 \text{ mm}$

Light well shape data-
with lens

$\rho_{00}/\rho_s = 95.6$

$x_{in} = -.15 \text{ mm}$

Divergence angle data-
without lens

Figure 5

Typical light well shape and output beam divergence angle photographs.

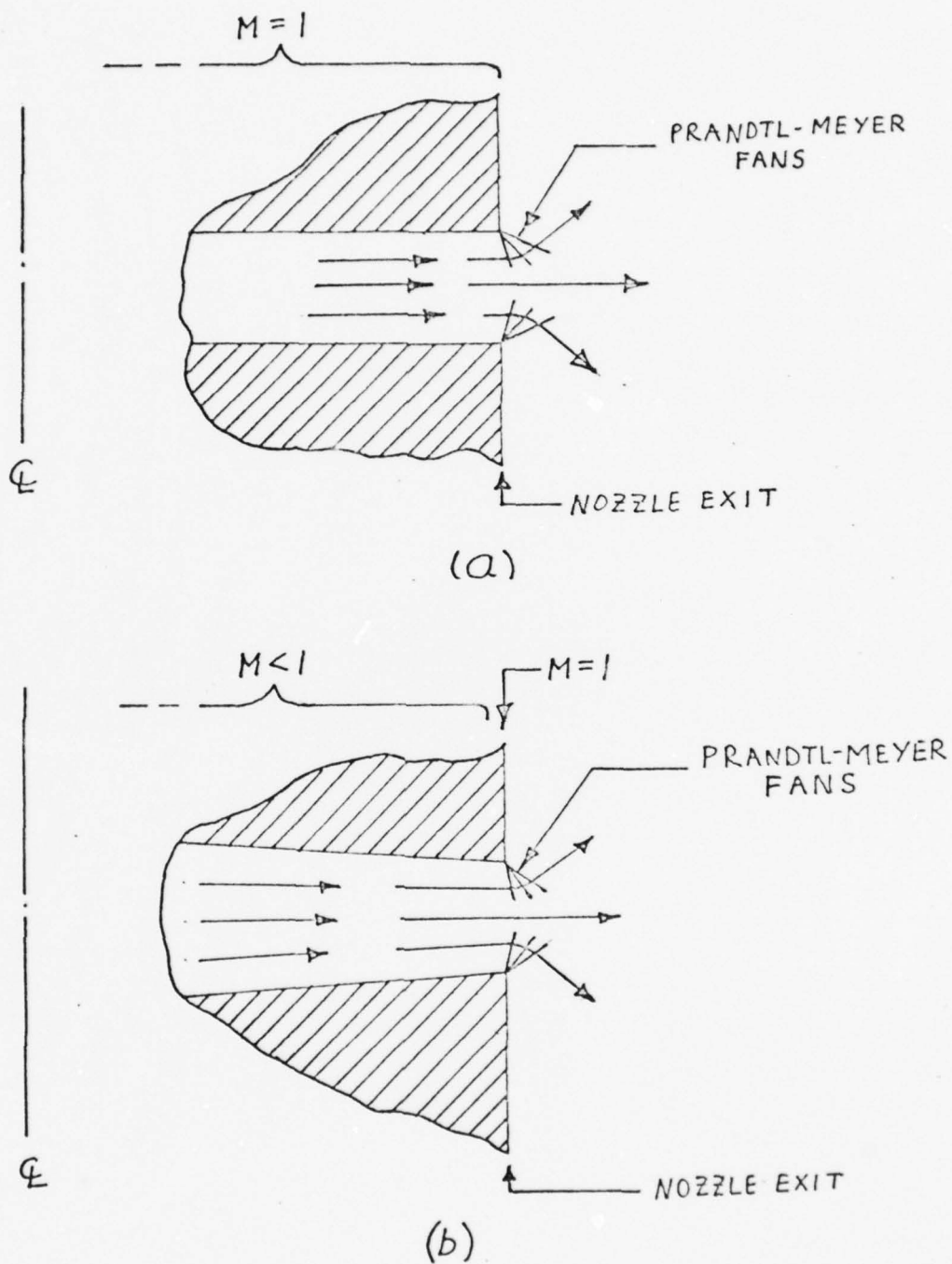


Figure 6.
Venus Machine geometries.
(a) Geometry for Frederick's calculations.
(b) Geometry for 90° Venus Machine.

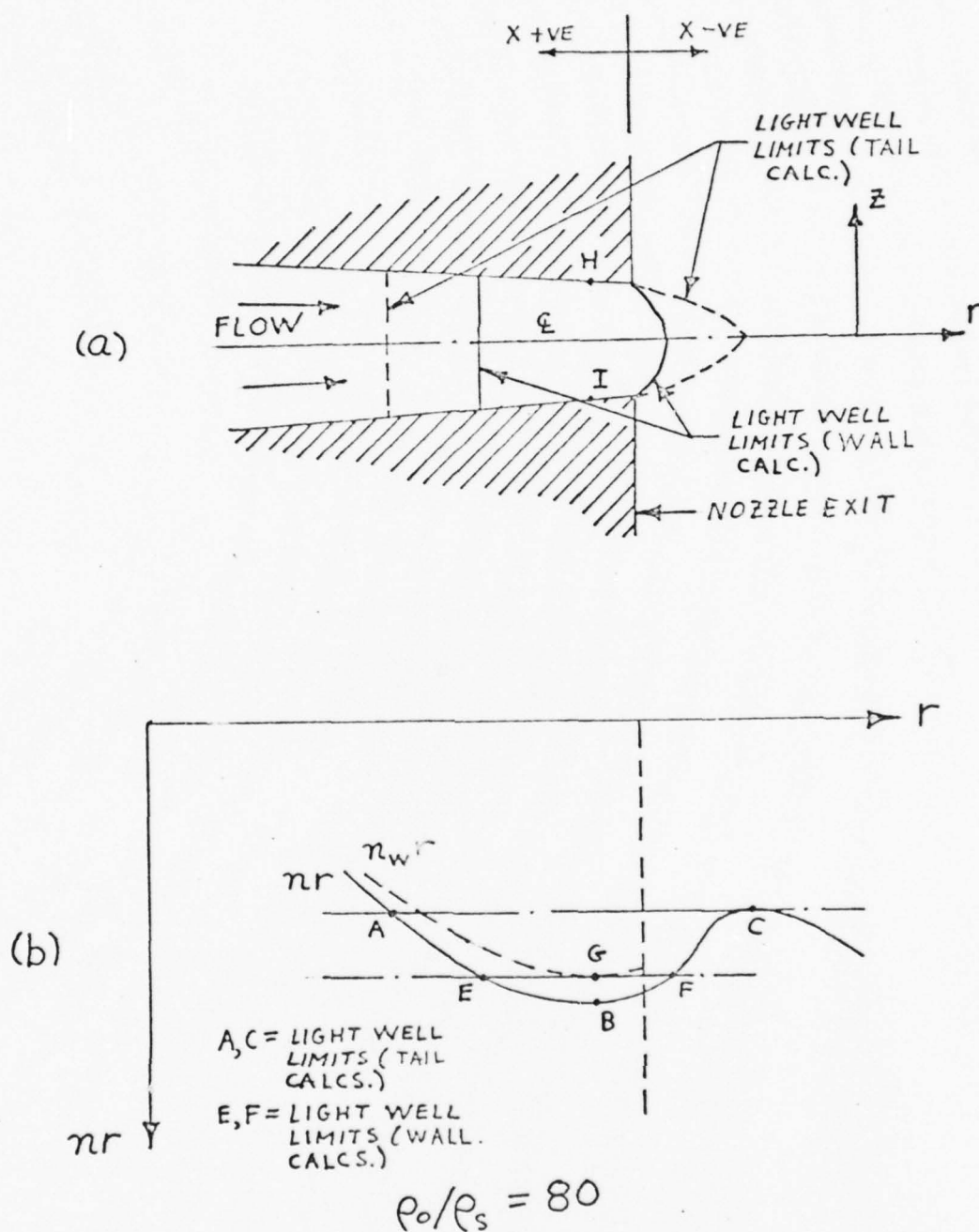


Figure 7.
 Calculated shape of light well, variation of nr with r along light well centerline and variation of $n_w r$ with r along walls (wall calculation).

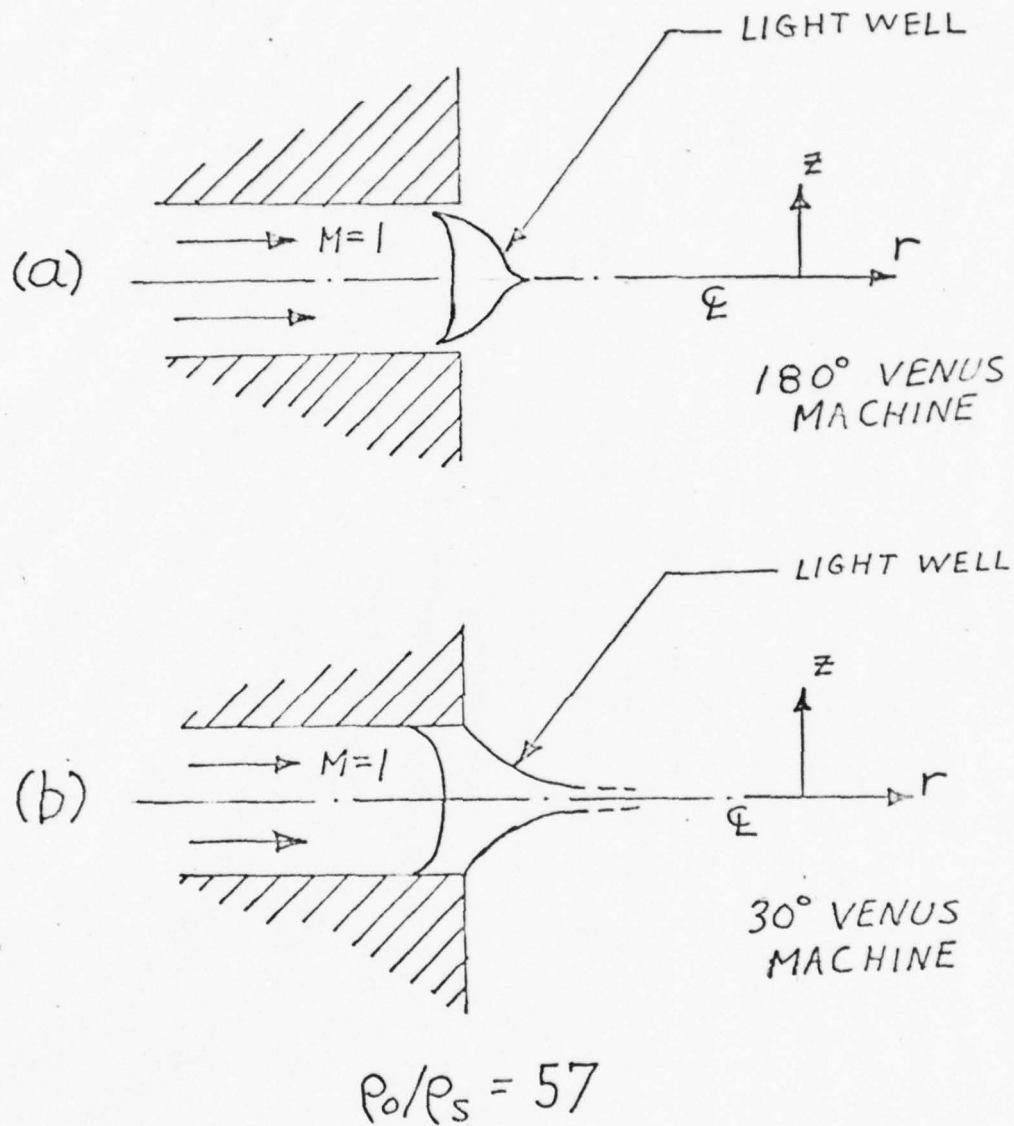
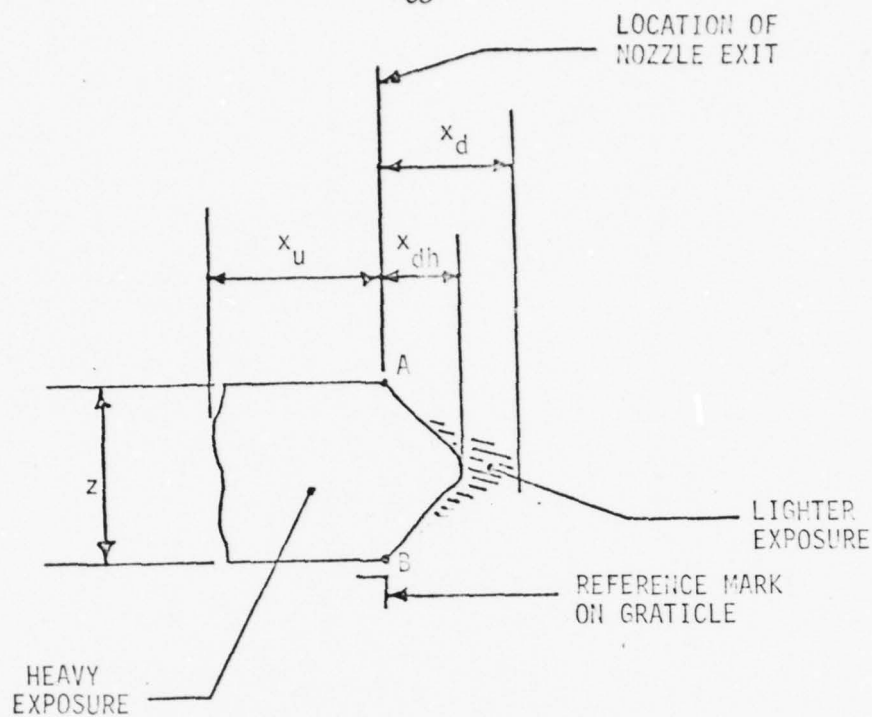


Figure 8.

Light well shapes calculated in Ref. 7 using ray tracing methods.

(a)
 $\rho_0/\rho_s = 70$



(b)
 $\rho_0/\rho_s = 50$

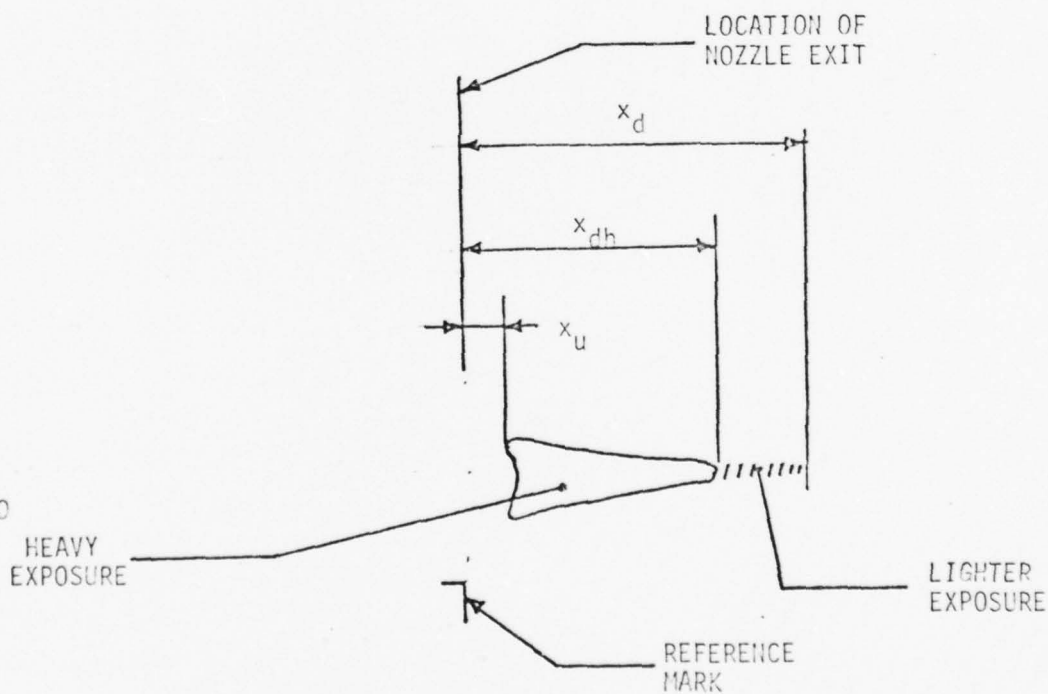


Figure 9
 Parameters used to describe the shapes of photographed light wells.

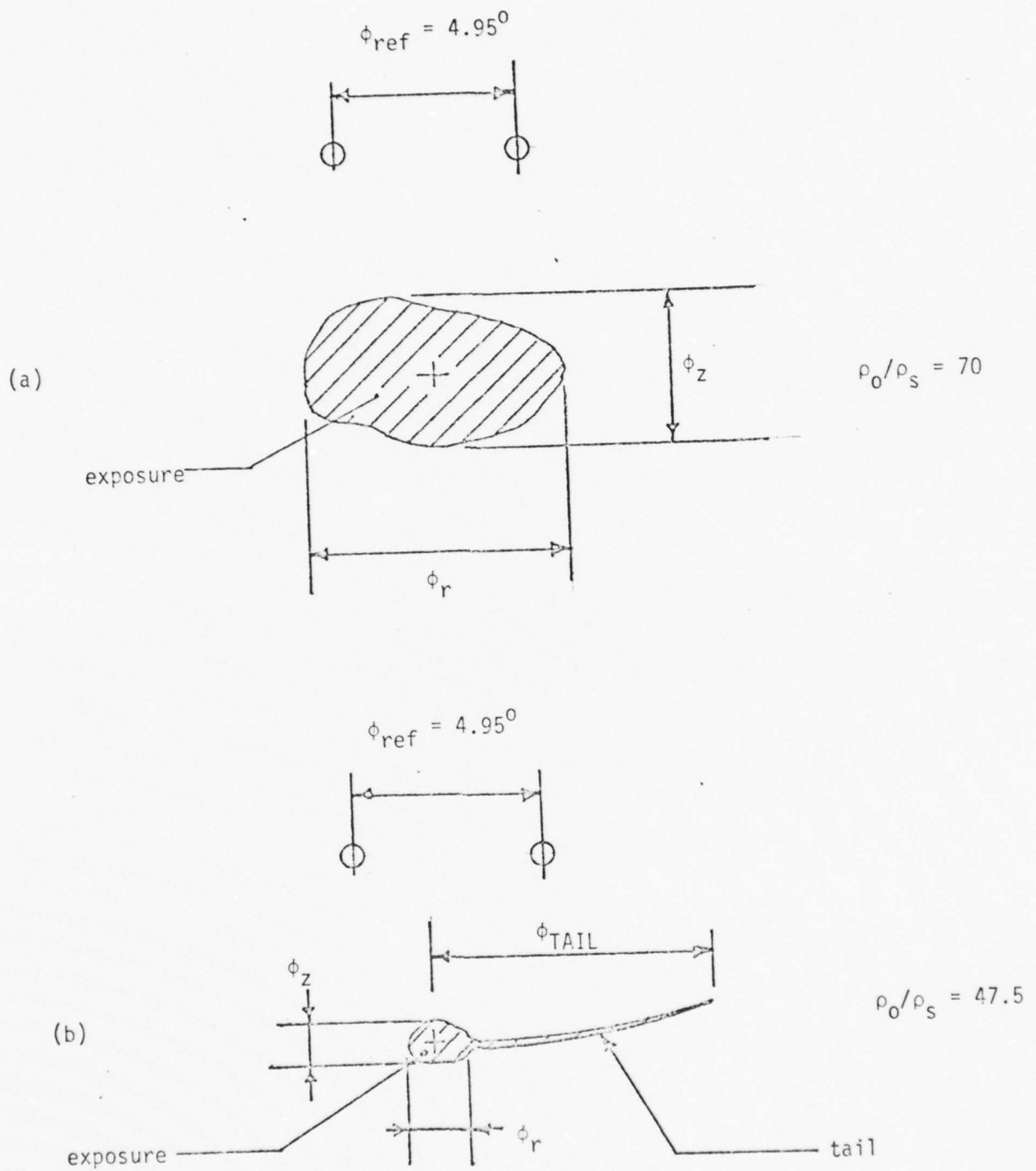


Figure 10.

Parameters used to describe the photographed shapes of the output beams of the Venus Machine.

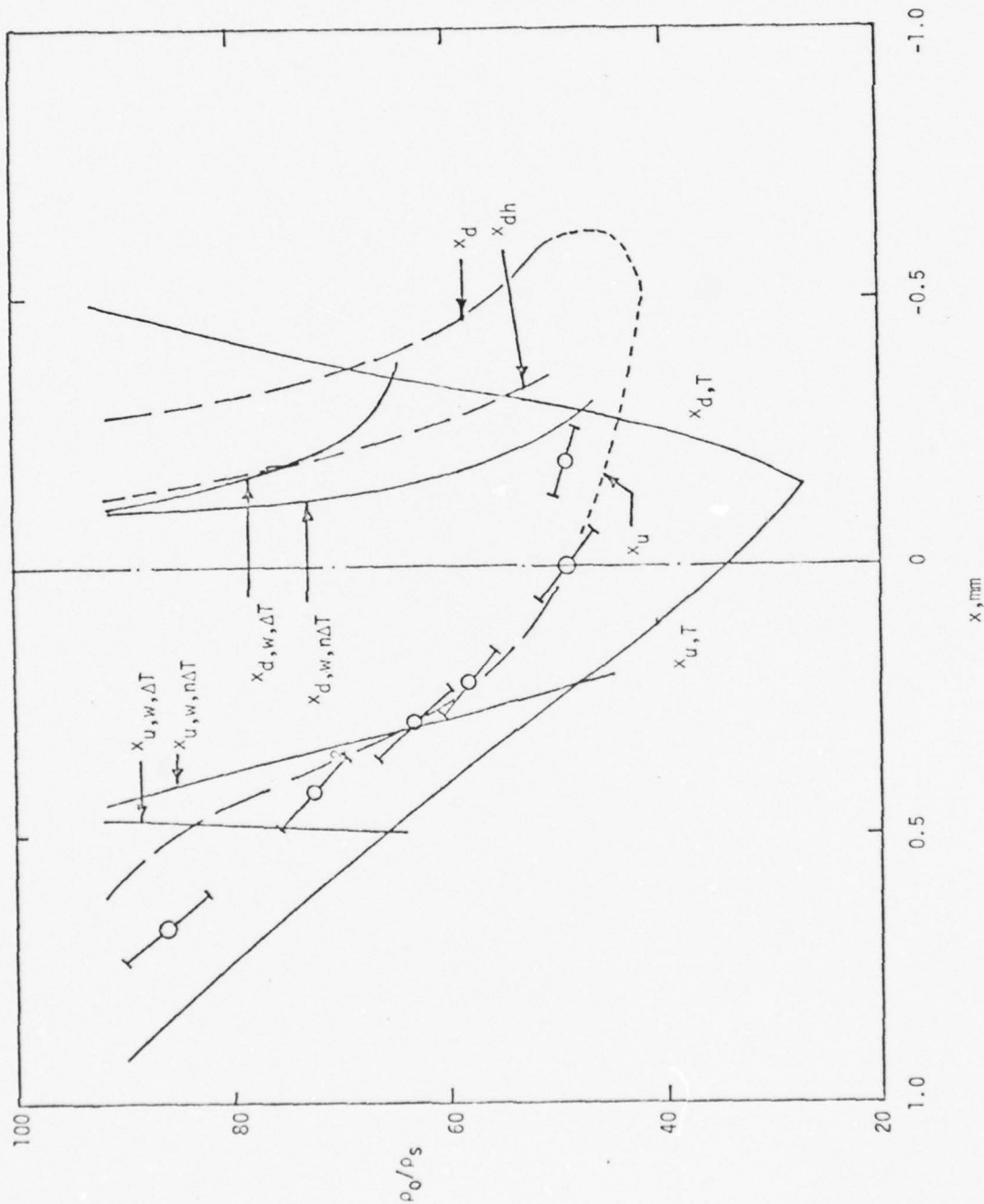


Figure 11.

Comparison of theoretically predicted and experimentally determined light well extents in the radial (x) direction. 1974 photographic data, and upstream light well limits estimated from transmission data.

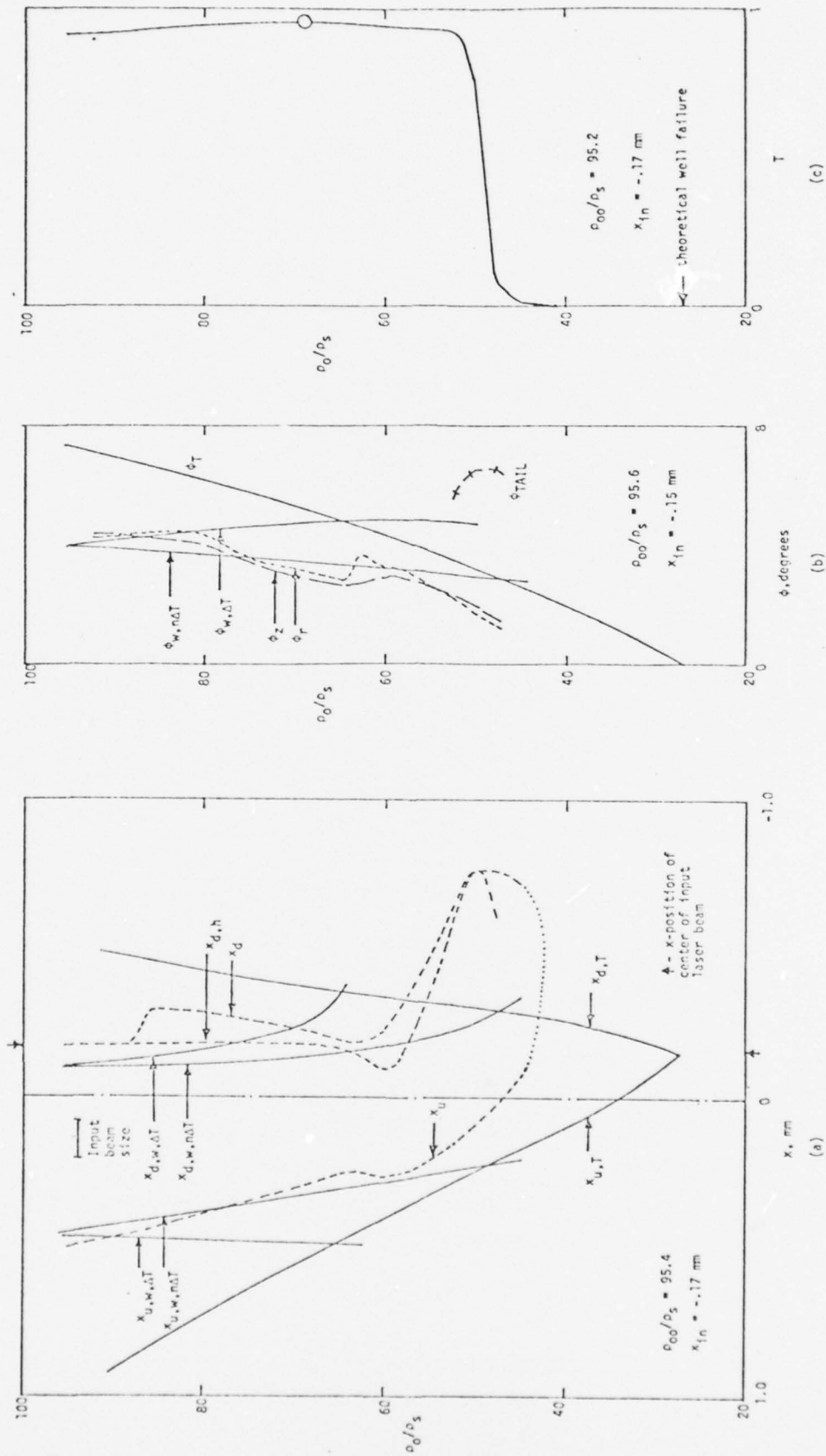


Figure 12.

Light well radial extent, output beam divergence angle and transmission data for $x_{in} \approx -.16$ mm, $\rho_{00}/\rho_s \approx 95$.

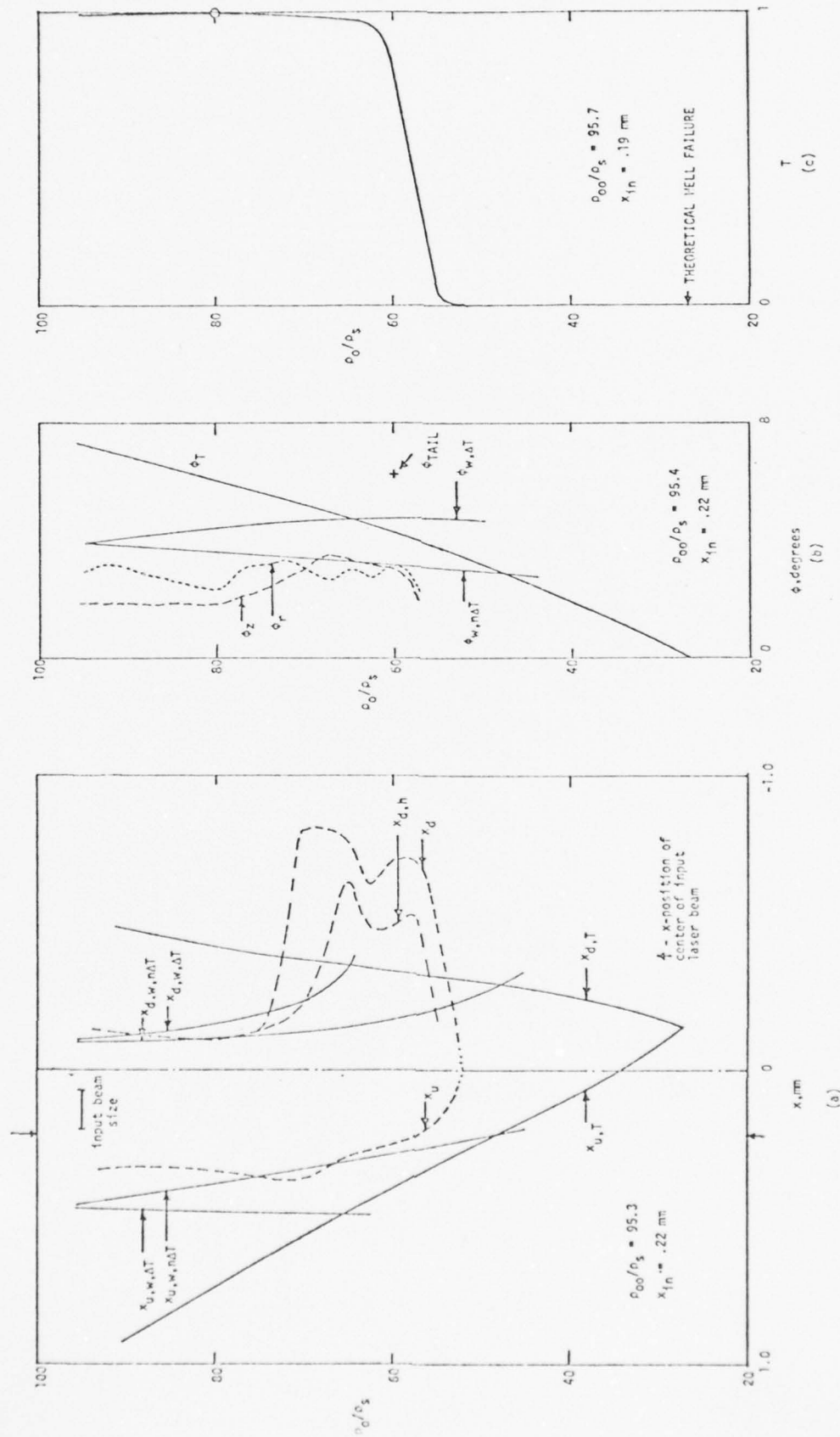


Figure 13.

Light well radial extent, output beam divergence angle and transmission data for $x_{in} \approx .20 \text{ mm}$, $\rho_{00}/\rho_s \approx 95$.

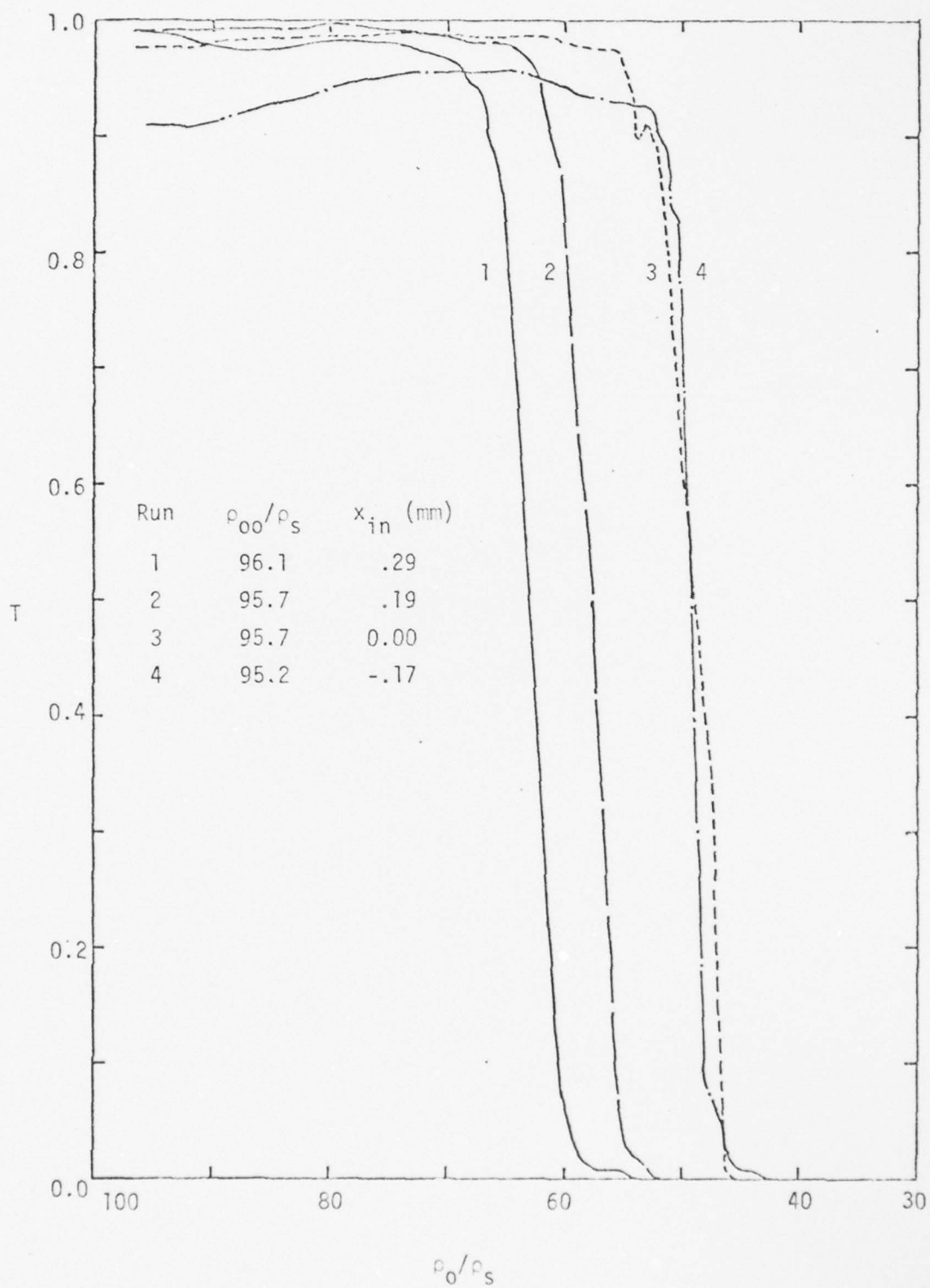


Figure 14.

Transmission data for $\rho_{00}/\rho_s \approx 95$, various x_{in} .

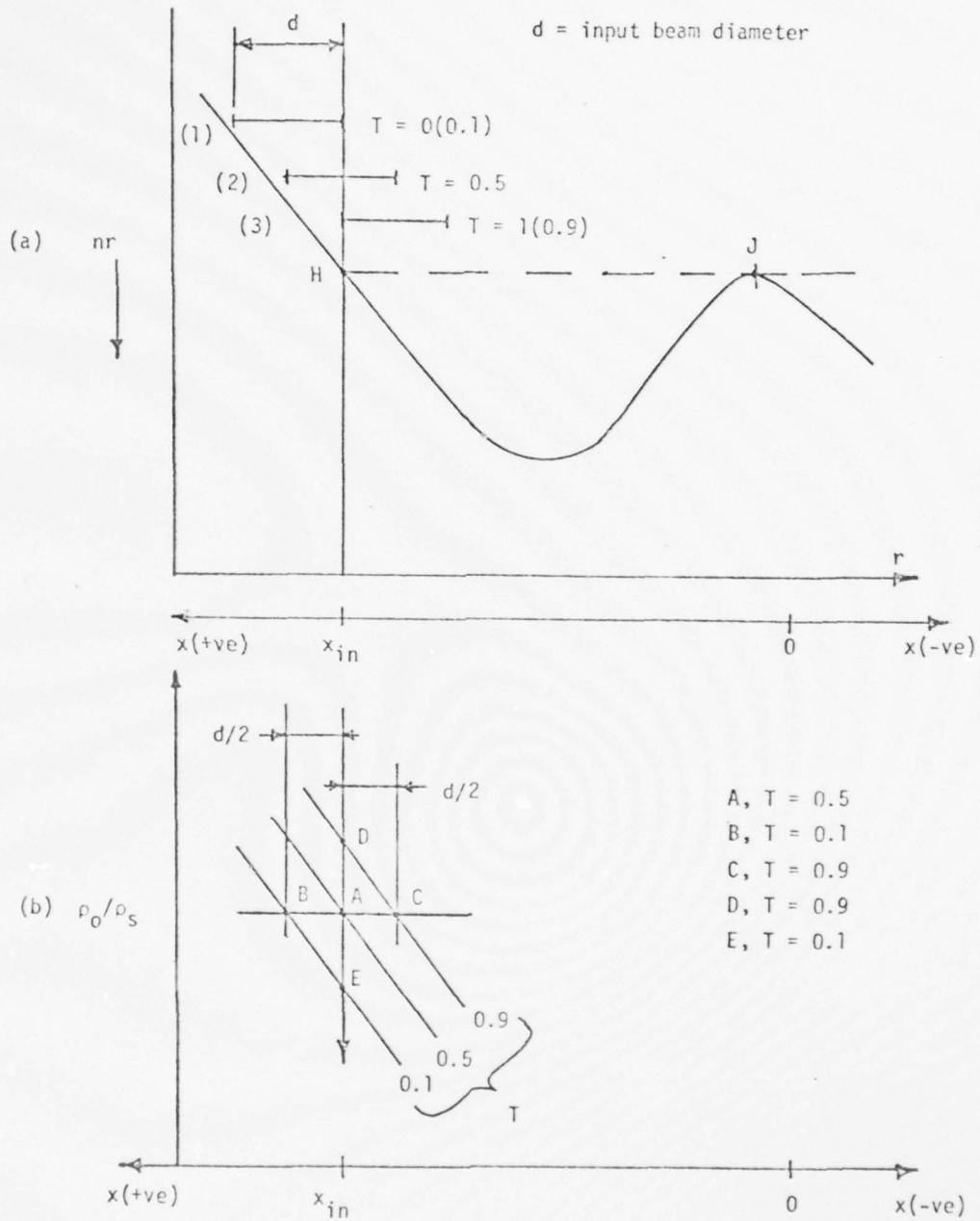


Figure 15.

Estimation of the upstream limit of the light well from transmission data.

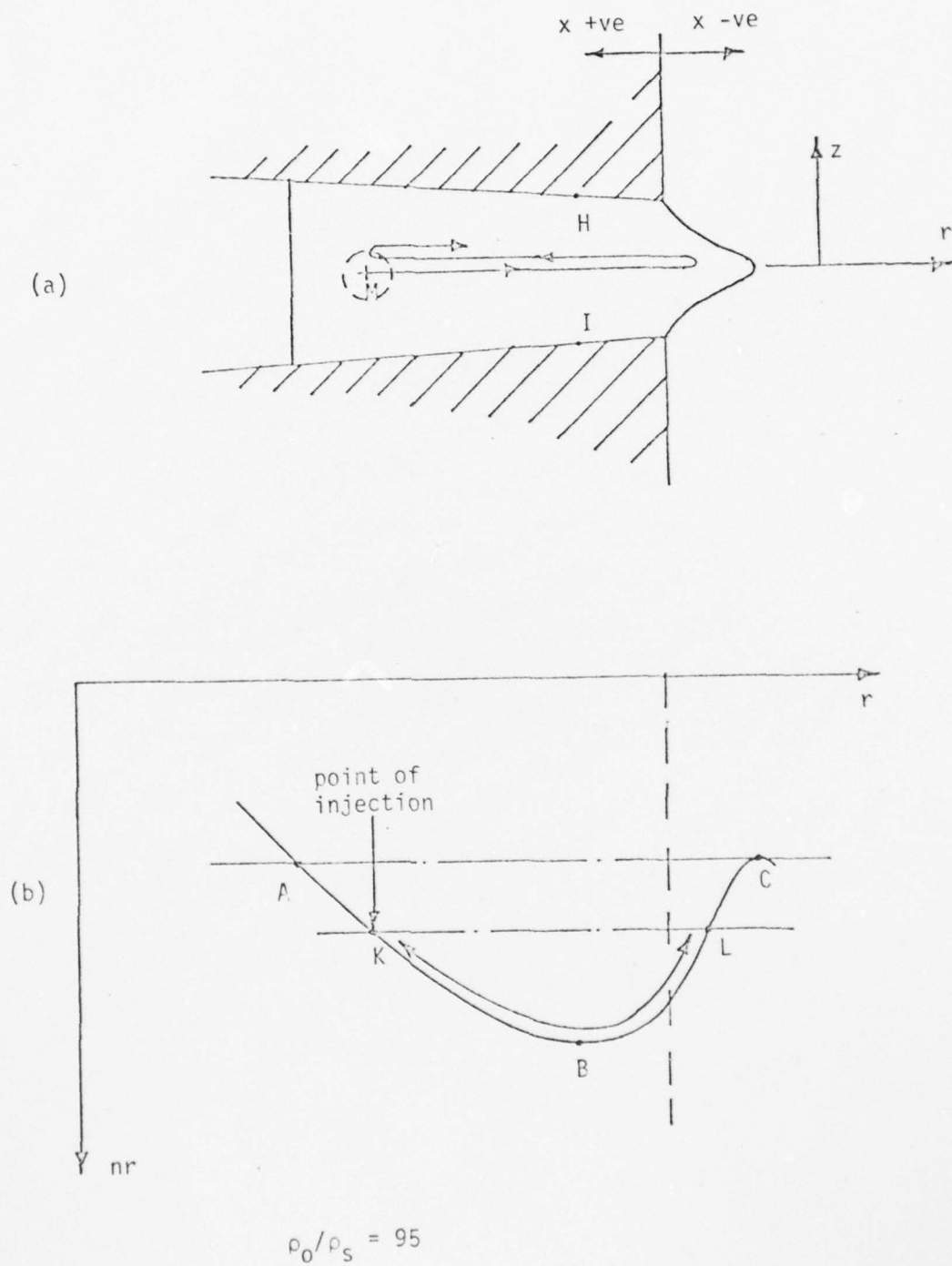


Figure 16.

Light well shape and nr versus r profile for discussion of r oscillations of light in the well.

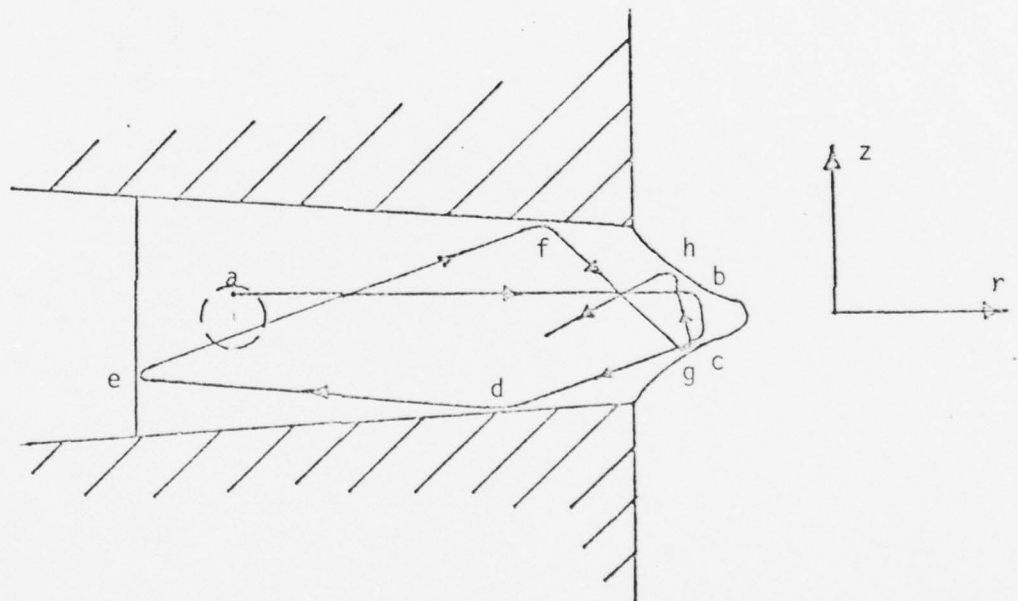


Figure 17.

Light well shape sketch for discussion of r and z oscillations of light in the well.

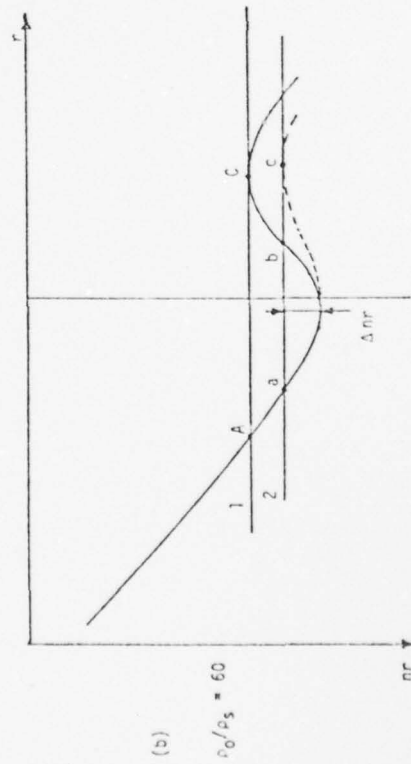
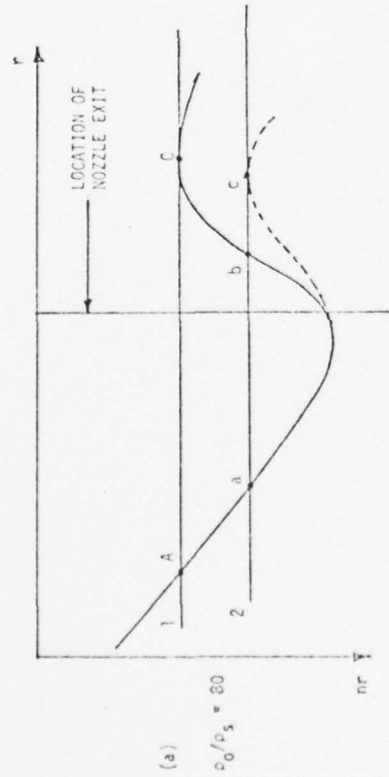


Figure 18.

Sketches used in the discussion of the estimation of the true n_r versus r profiles along the nozzle centerline.

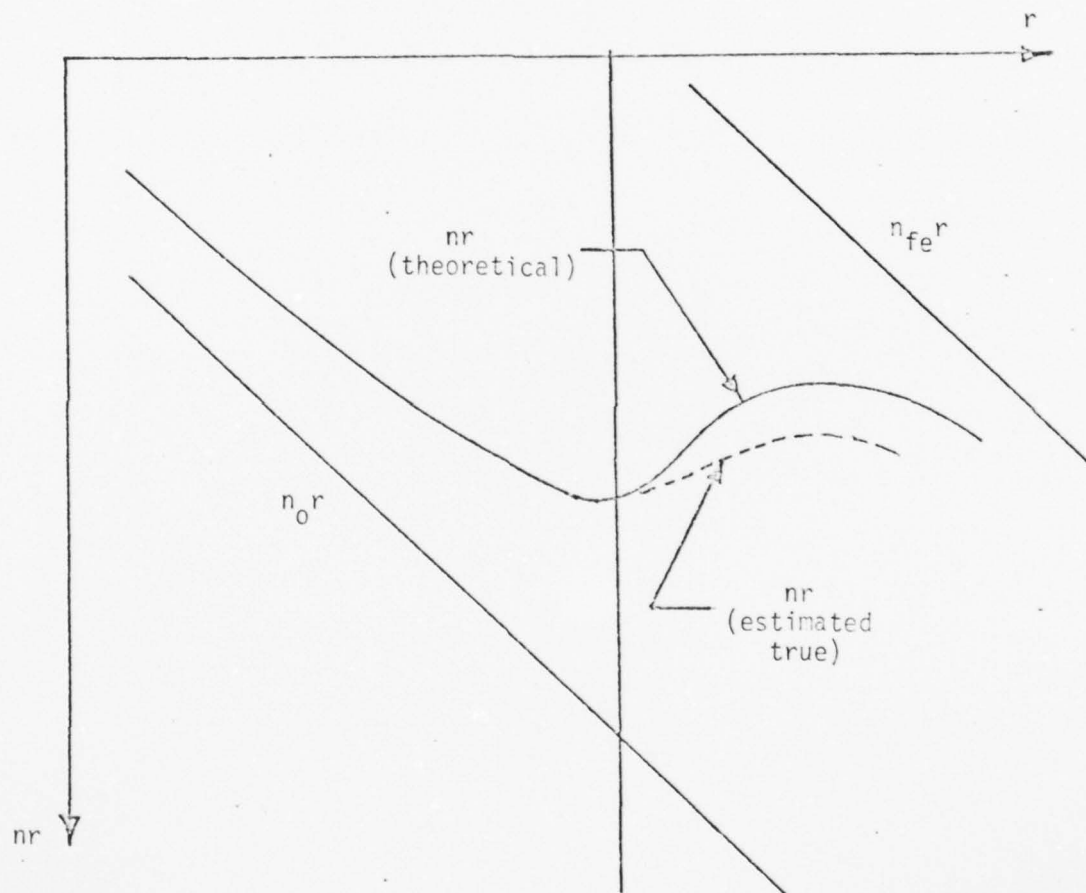


Figure 19.

nr versus r profile and limiting lines; used in discussion of estimates of true nr versus r profiles.

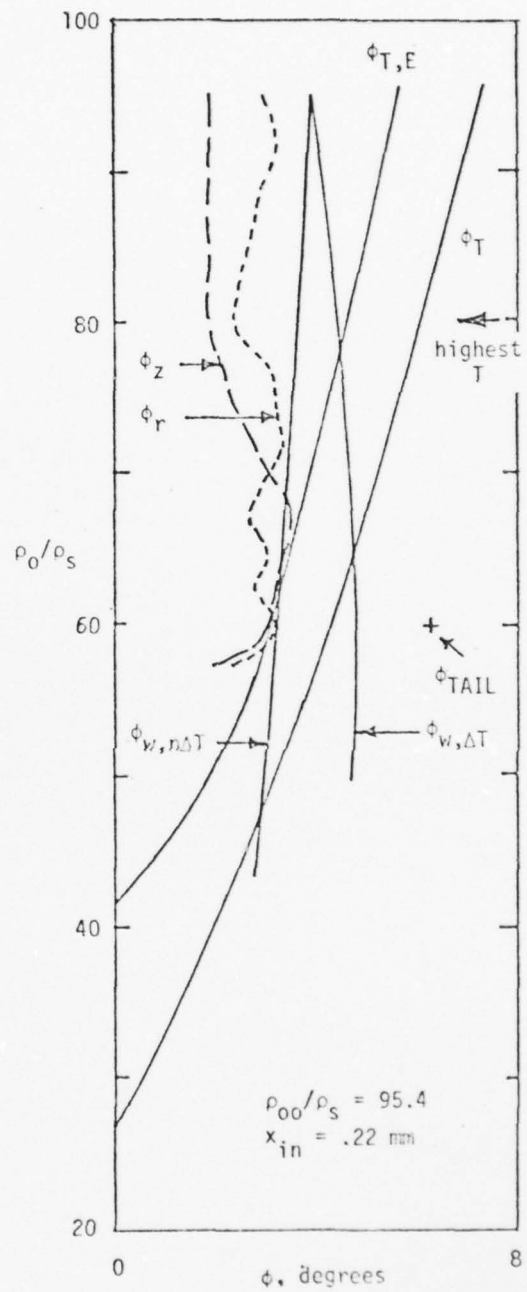
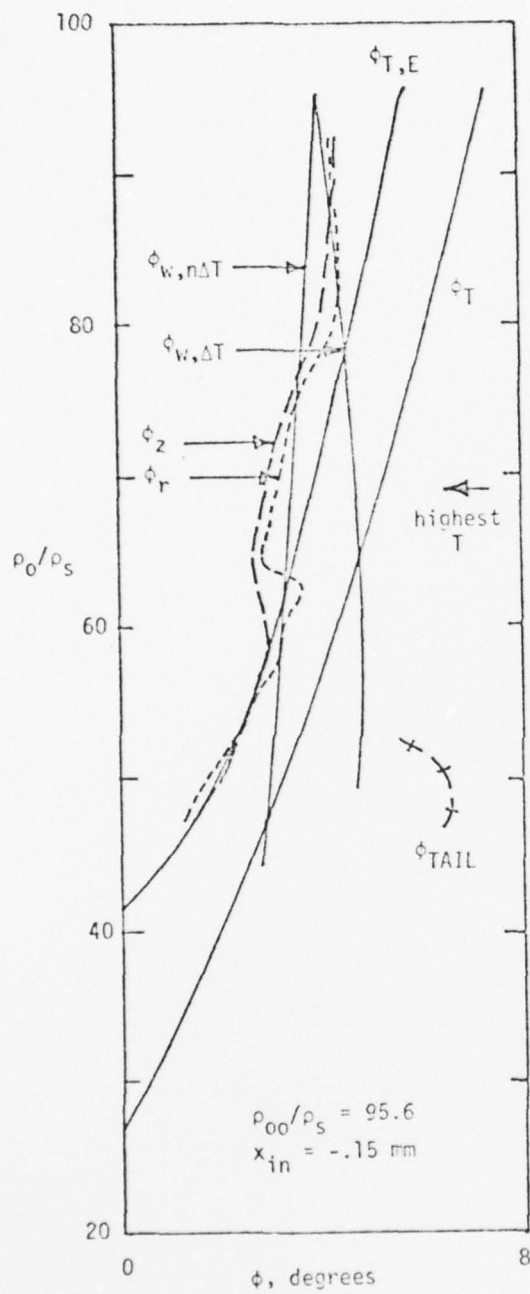


Figure 20.

Output beam divergence angle data, shown plotted with theoretical and quasi-theoretical limiting curves.

-80-

ρ_0/ρ_s

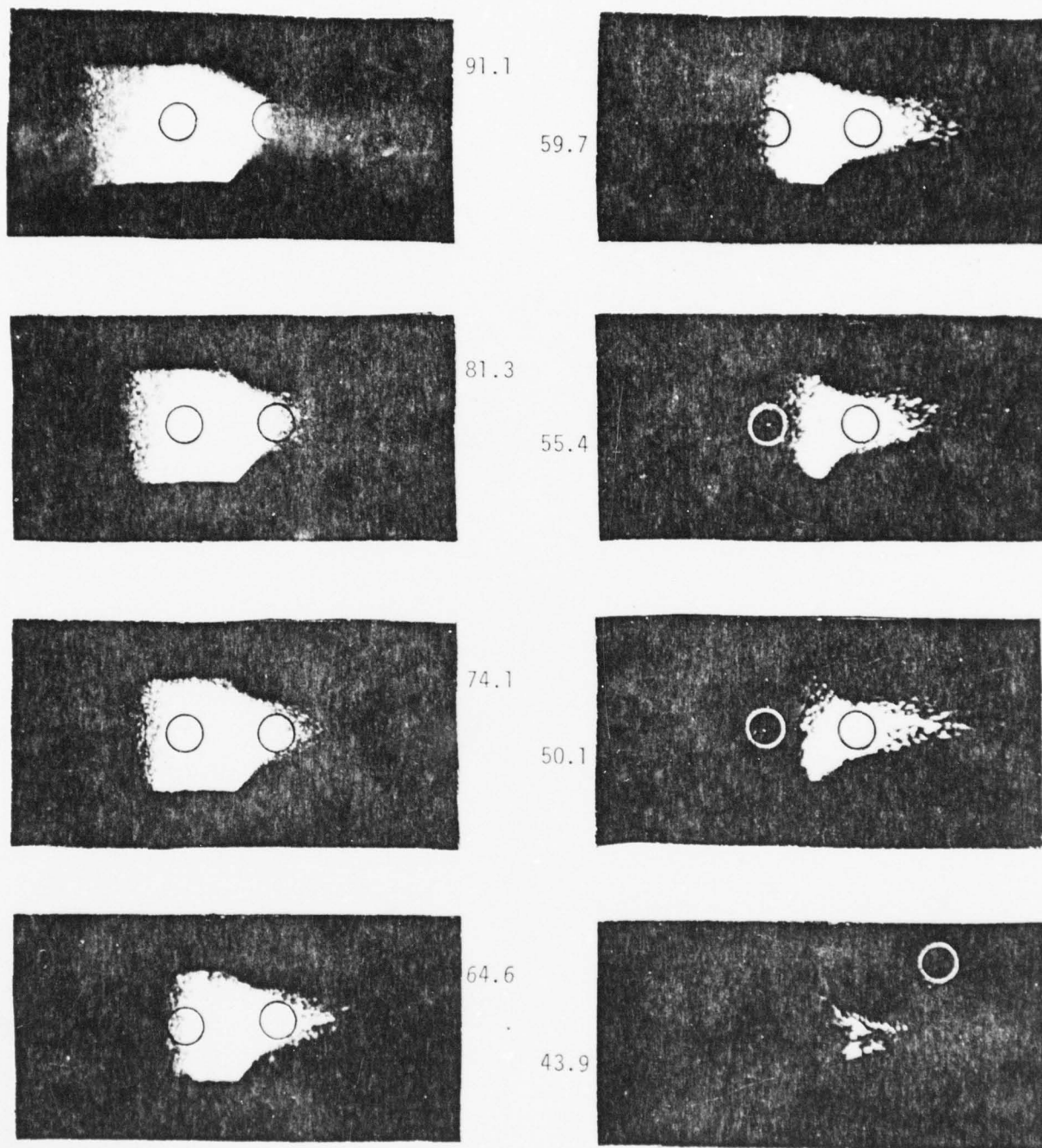


Figure 21.

Light well photographs; early (1974) data.

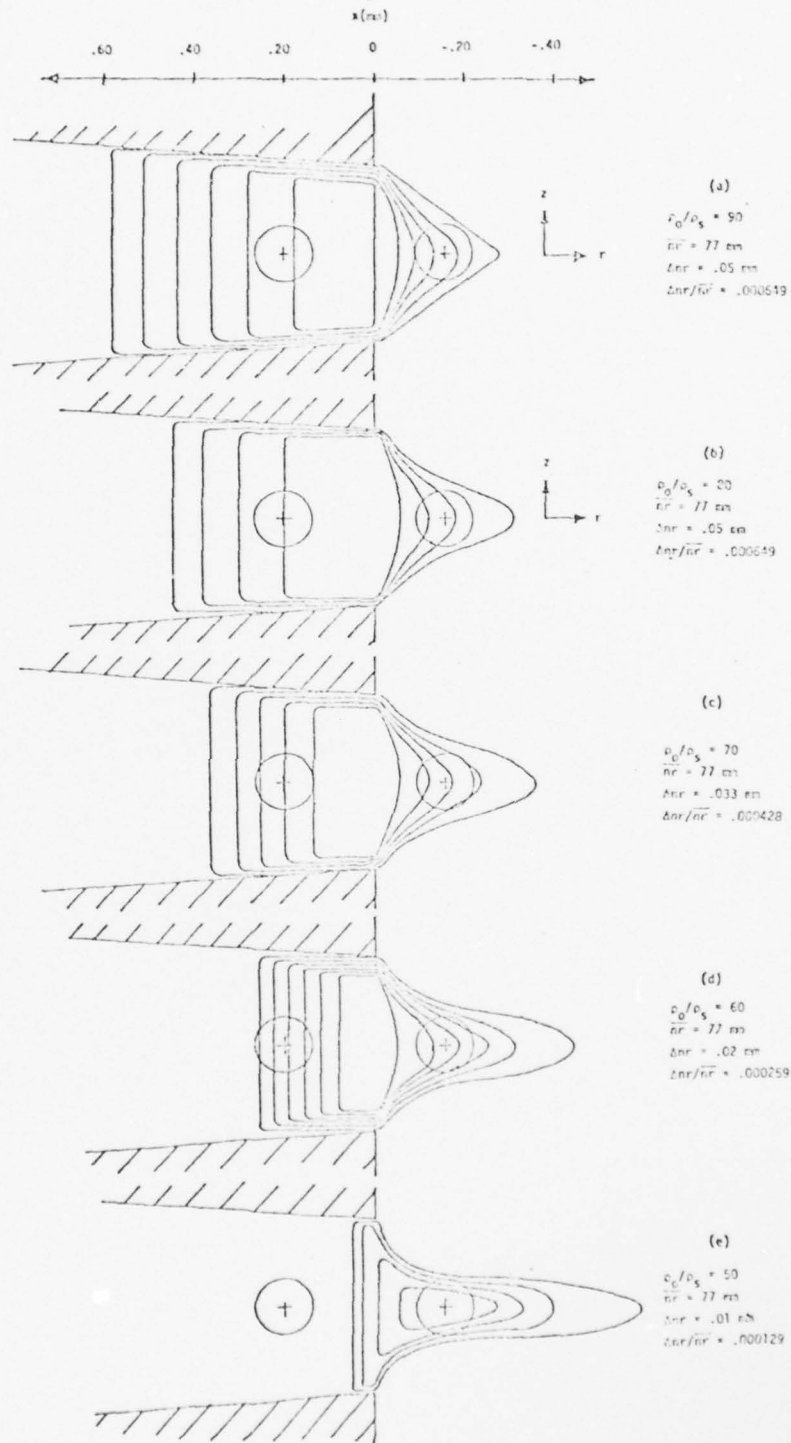


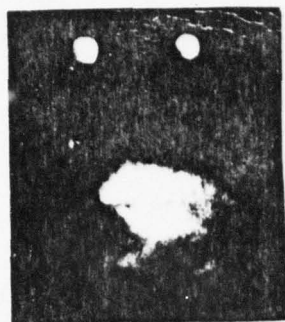
Figure 22.

Estimated true nr contour plots for the light wells.

ρ_0/ρ_s

ρ_0/ρ_s

95



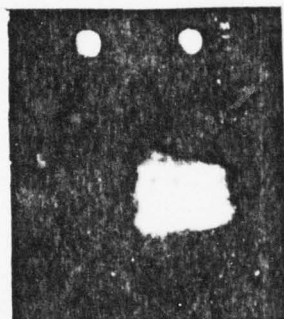
(a)

90



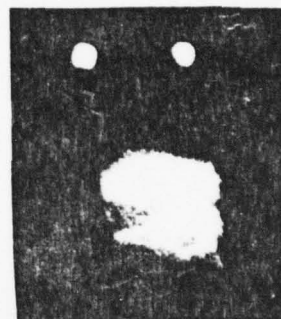
(d)

82.5



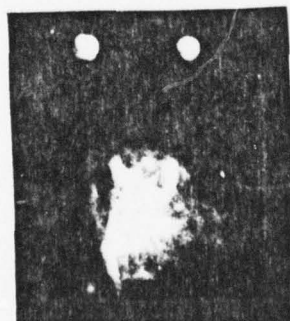
(b)

67.5



(e)

65

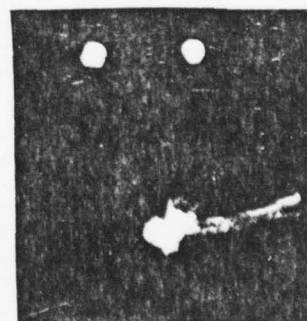


(c)

$\rho_{00}/\rho_s = 95.4$

$x_{in} = .22 \text{ mm}$

47.5



(cc)

$\rho_{00}/\rho_s = 95.6$

$x_{in} = -.15 \text{ mm}$

Figure 23.

Output beam divergence angle photographs.

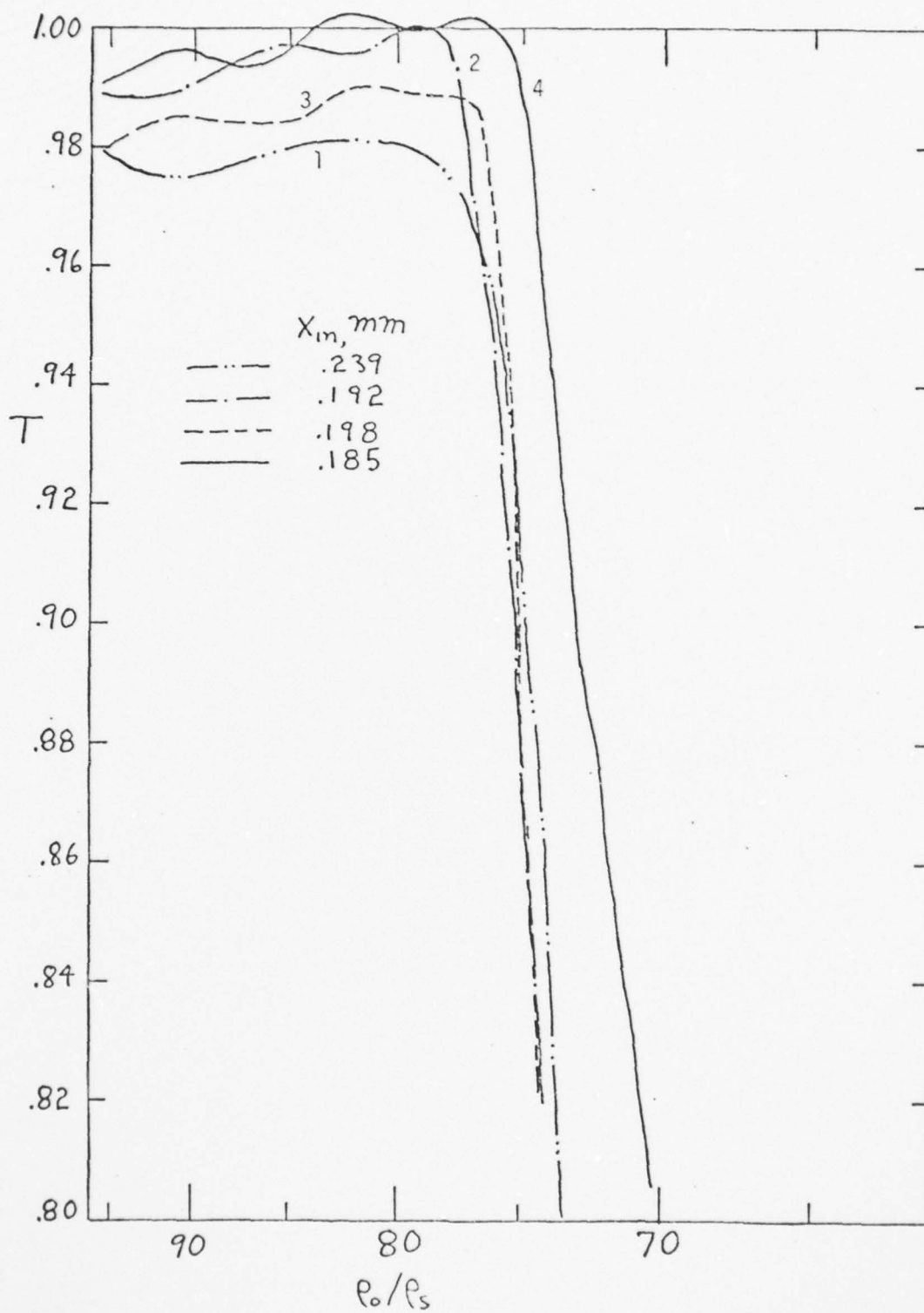


Figure 24.

Transmission data taken under high transmission operating conditions.

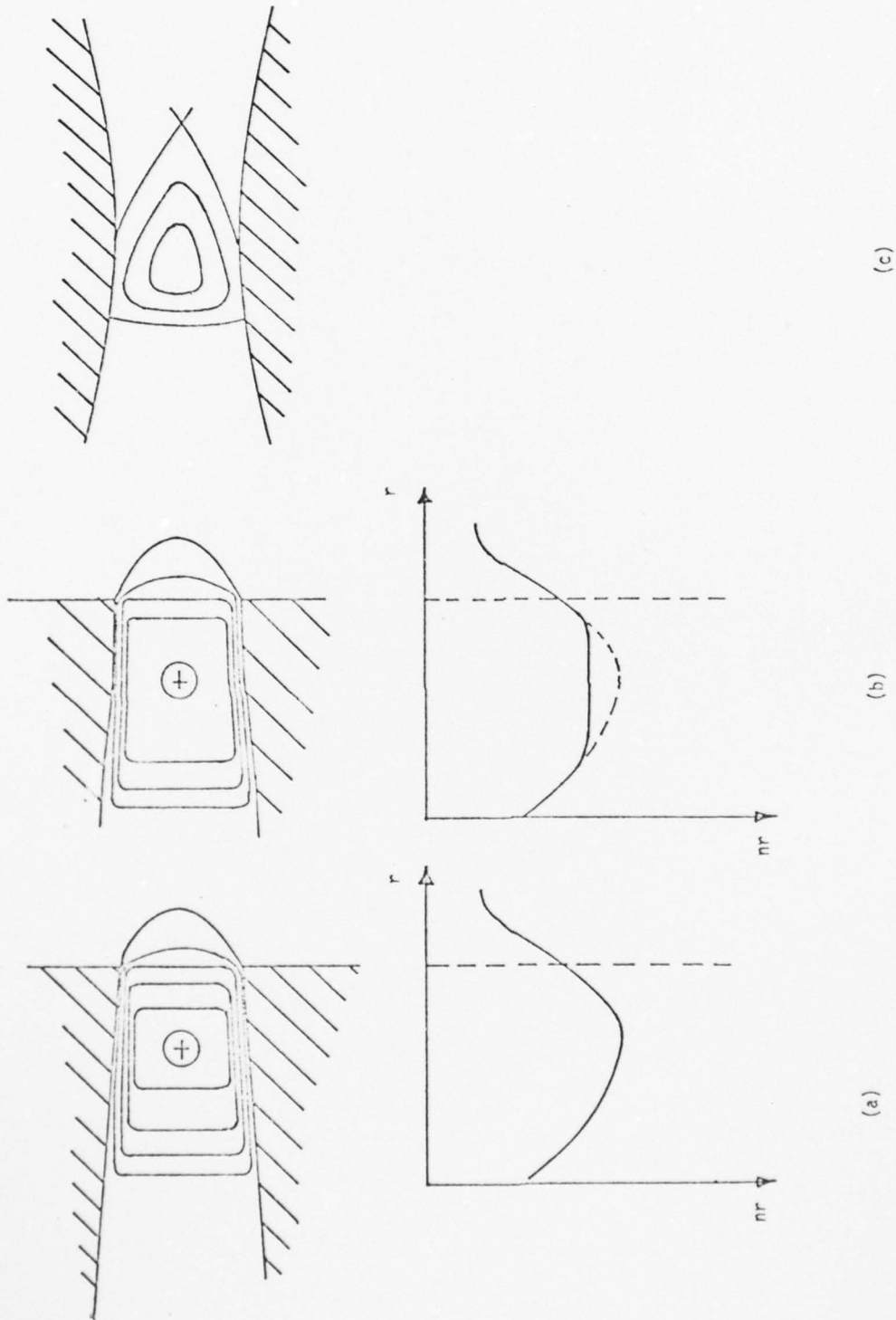


Figure 25.
nr contour plots and nr versus r profiles for recommended improved Venus Machine light wells.

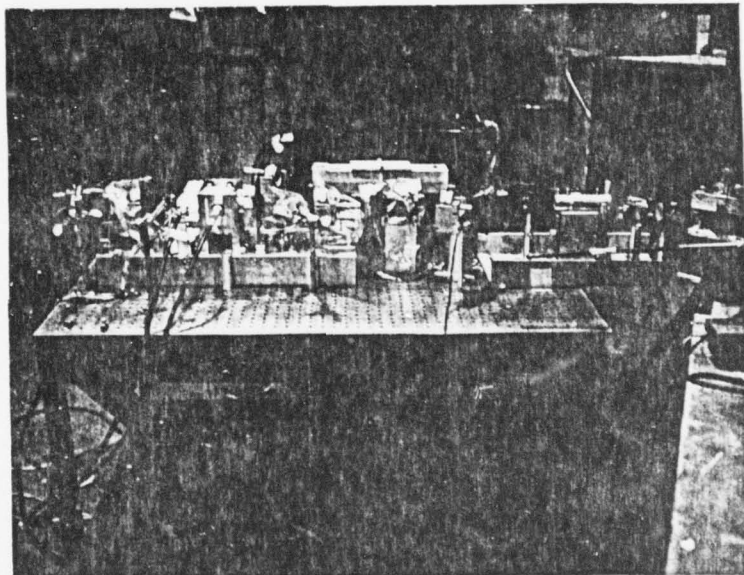


Figure 26.

Ruby laser.

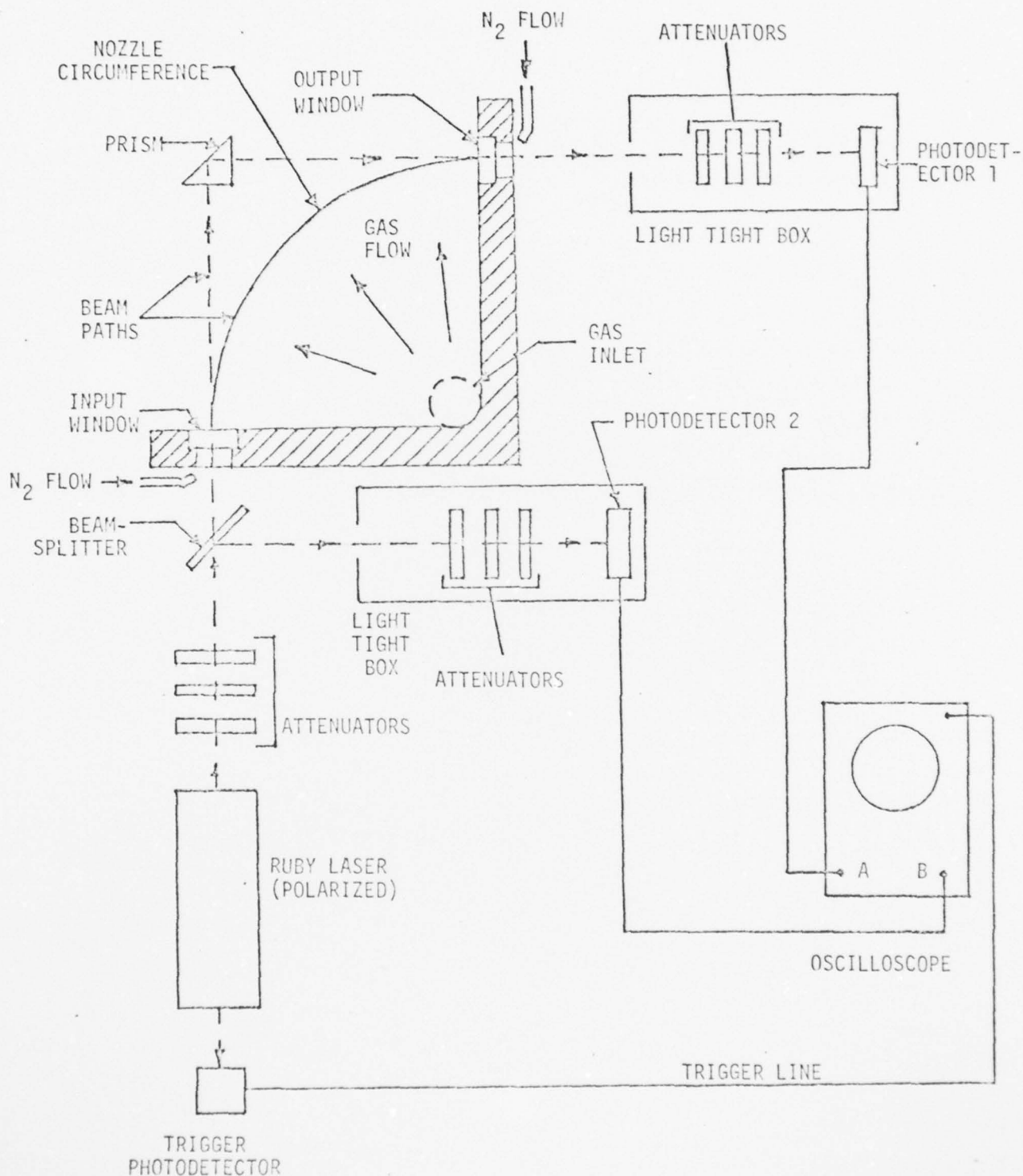


Figure 27.

Experimental setup for high power transmission measurements on the 90° Venus Machine.

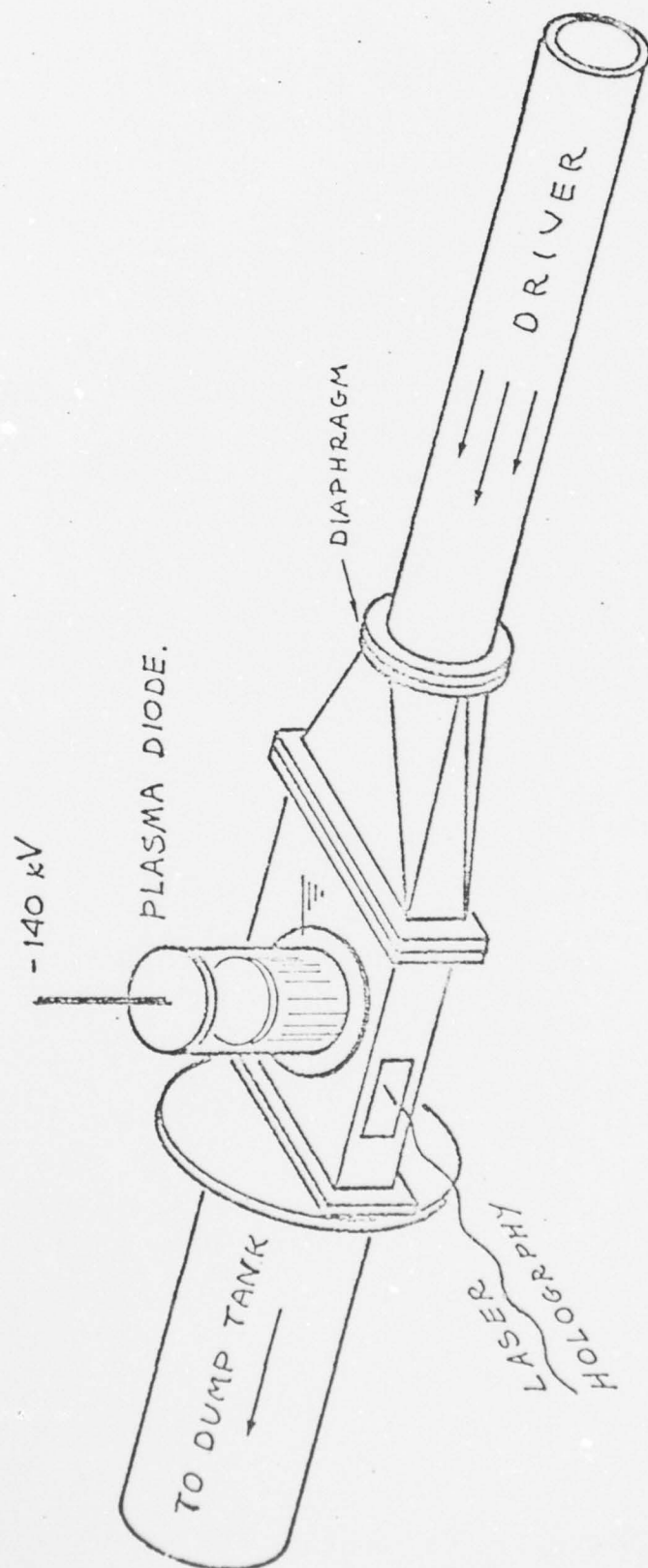


FIG. 28 SCHEMATIC OF DISCHARGE / FLOW FACILITY

AD-A062 390

WASHINGTON UNIV SEATTLE

F/G 20/5

FLUID MECHANICAL REFRACTING GAS PRISM AND AERODYNAMICS OF E - B--ETC(U)

MAY 78 D W BOGDANOFF, W H CHRISTIANSEN

AFOSR-74-2650

AFOSR -TR-78-1494

NL

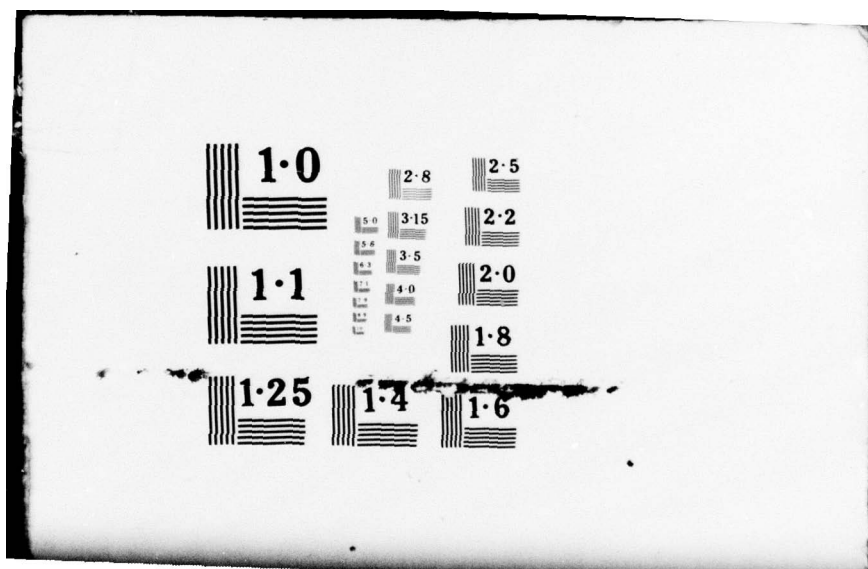
UNCLASSIFIED

2 OF 2
ADA
082390



END
DATE
FILMED

3 -79
DDC



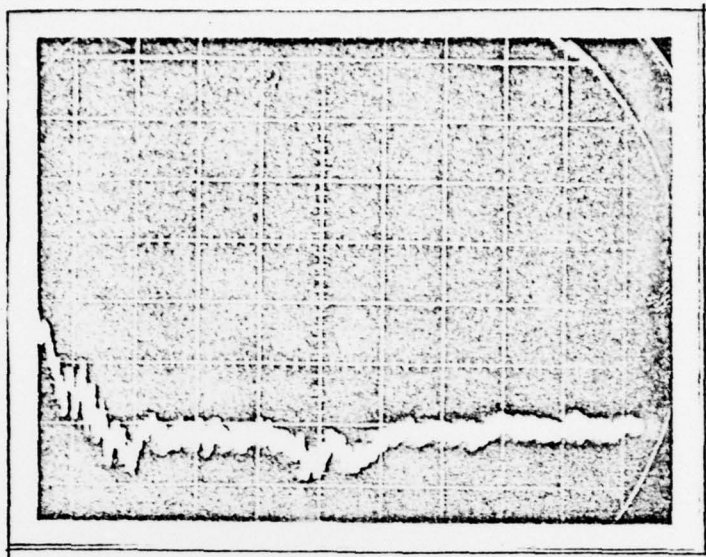


Fig. 29 Test section pressure history
 $t = 1\text{ms/div}$

Boundary
Layer

Scale 5:1

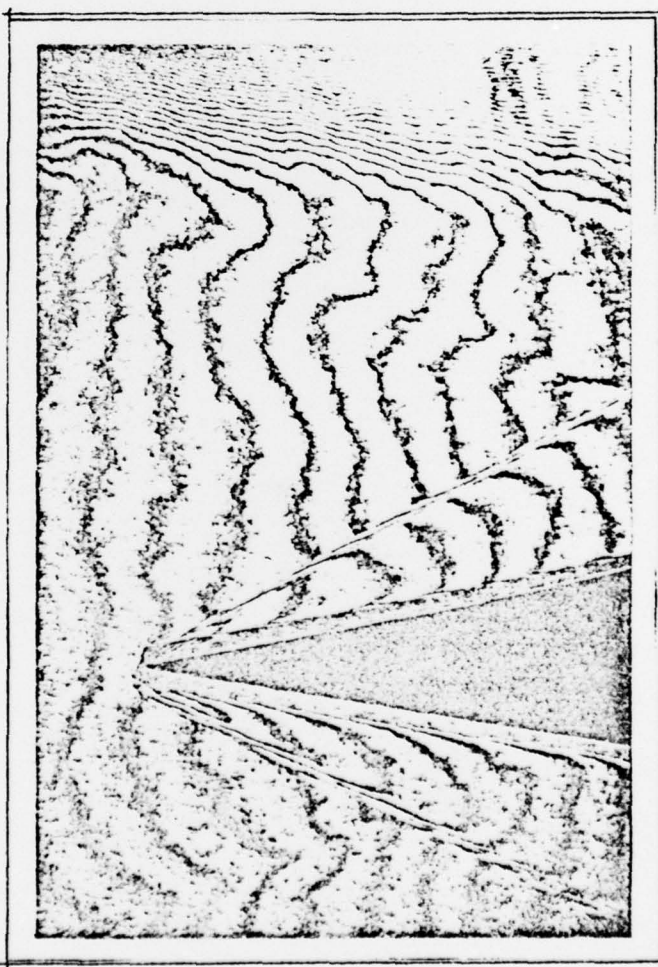


Fig. 30 Oblique shock on 2-D wedge

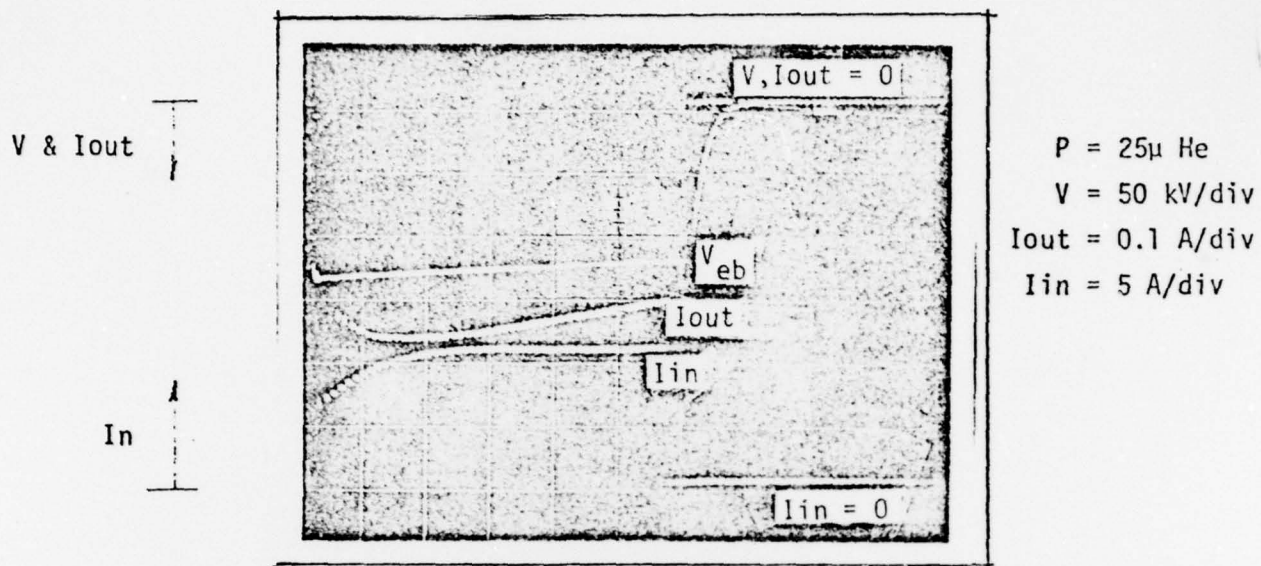


Fig. 31 E-Beam Voltage & Current Traces
t = 50 μ s/div

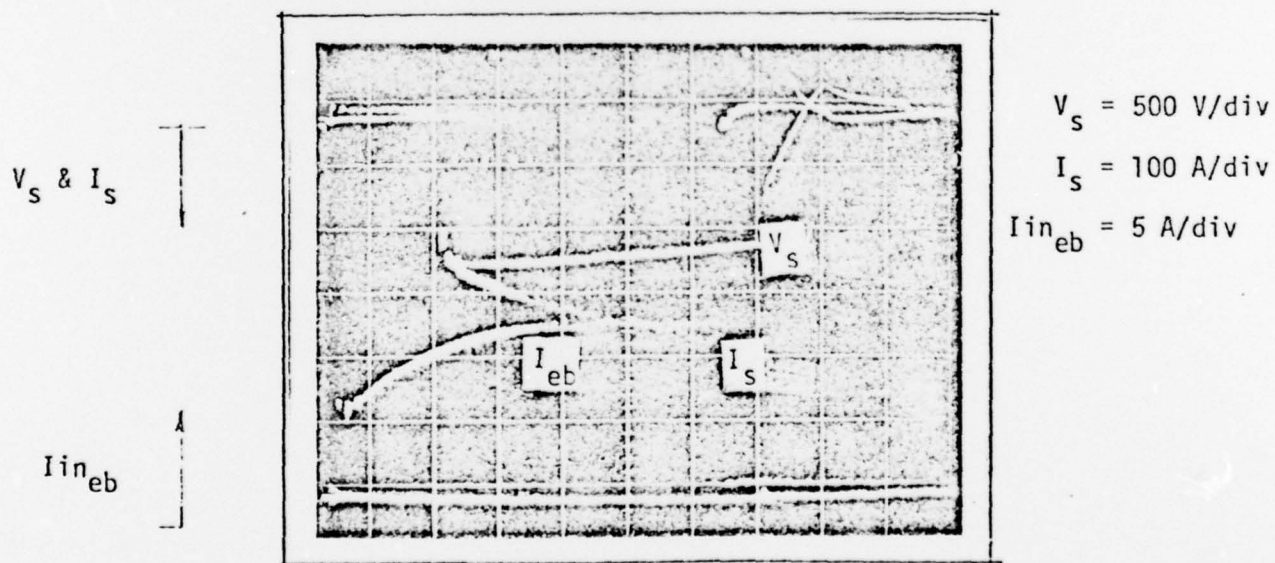


Fig. 32 Sustainer Voltage-current traces
t = 50 μ s/div

REPORT DOCUMENTATION PAGE		READ INSTRUCTIONS BEFORE COMPLETING FORM
1. REPORT NUMBER AFOSR-TR- 78 - 1494	2. GOVT ACCESSION NO.	3. RECIPIENT'S CATALOG NUMBER
4. TITLE (and Subtitle) FLUID MECHANICAL REFRACTING GAS PRISM AND AERO- DYNAMICS OF E - BEAM SUSTAINED DISCHARGE IN SUPERSONIC FLOW, BOTH APPLICABLE TO LASER TECHNOLOGY	5. TYPE OF REPORT & PERIOD COVERED INTERIM 1 Jan 77 - 31 Dec 77	
7. AUTHOR(s) D W BOGDANOFF W H CHRISTIANSEN	6. PERFORMING ORG. REPORT NUMBER	
9. PERFORMING ORGANIZATION NAME AND ADDRESS UNIVERSITY OF WASHINGTON AEROSPACE & ENERGETICS RESEARCH PROGRAM SEATTLE, WASHINGTON 98195	8. CONTRACT OR GRANT NUMBER(s) AFOSR 74-2650 ✓	
11. CONTROLLING OFFICE NAME AND ADDRESS AIR FORCE OFFICE OF SCIENTIFIC RESEARCH/NA BLDG 410 BOLLING AIR FORCE BASE, D C 20332	10. PROGRAM ELEMENT, PROJECT, TASK AREA & WORK UNIT NUMBERS 2307A3 61102F	
14. MONITORING AGENCY NAME & ADDRESS (if different from Controlling Office)	12. REPORT DATE May 1978	
	13. NUMBER OF PAGES 99	
	15. SECURITY CLASS. (of this report) UNCLASSIFIED	
16. DISTRIBUTION STATEMENT (of this Report) Approved for public release; distribution unlimited.		
17. DISTRIBUTION STATEMENT (of the abstract entered in Block 20, if different from Report)		
18. SUPPLEMENTARY NOTES		
19. KEY WORDS (Continue on reverse side if necessary and identify by block number) VENUS MACHINE GAS PRISM LASERS ELECTRIC DISCHARGE LASER OPTICAL CONTROL		
20. ABSTRACT (Continue on reverse side if necessary and identify by block number) Details are presented of extensive experimental tests of a 90 degree Venus Machine, a fluid mechanical optical control device which deflects a beam of light continuously through large angles. A motion-picture photographic technique was used to obtain extensive data under a variety of operating conditions on the size and shape of the light well, a region in the flow where light rays are trapped in near circular paths. The angular divergence of the laser beam leaving the Venus Machine was also measured for the same range of operating conditions. These experimental results, along with parallel theoretical work, have allowed a		

DD FORM 1 JAN 73 1473

UNCLASSIFIED
SECURITY CLASSIFICATION OF THIS PAGE (When Data Entered)

reasonably complete understanding of the operation of the present 90 degree device at low laser power levels and have indicated that potential exists for the design of Venus Machines of much higher performance and optical quality. Construction of a ruby laser and the necessary optical and detector systems for high-power Venus Machine transmission was completed. Preliminary calibration measurements with the detector system were made. Other experimental work is underway to find ways of improving the performance of electron-beam sustained electric discharge lasers. Some considerations include discharge boundary layer interactions and medium homogeneity. Preliminary results of the fundamental mechanisms of the interaction of electrical discharges of the glow type and the fluid mechanics as found in supersonic electric discharge lasers are briefly presented in this report. ↗

UNCLASSIFIED

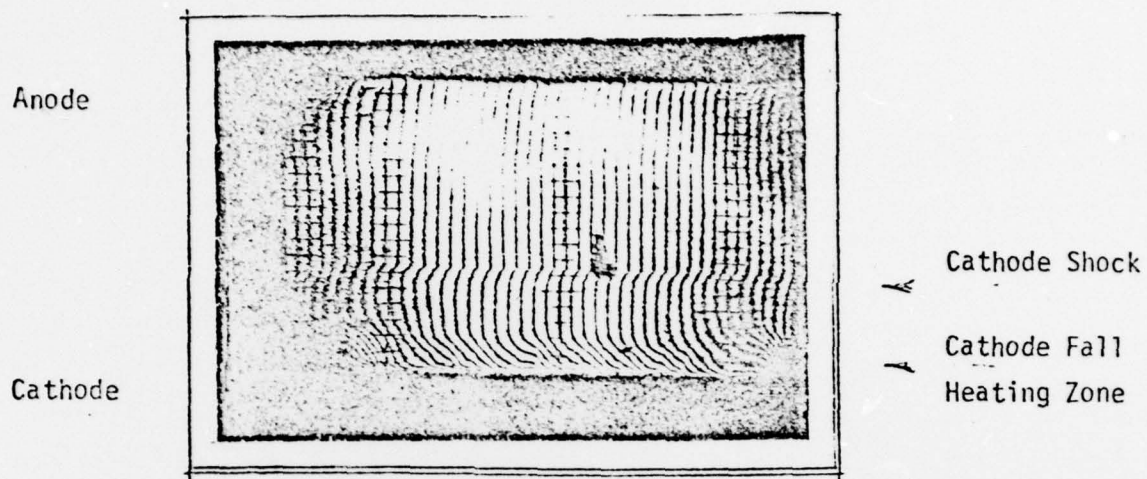


Fig. 33 Interferogram of Cathode Shock
 $t_{\text{ruby}} = 35 \mu\text{s}$ after sustainer pulse
 $\Delta\rho/\rho = 6\%$ per fringe

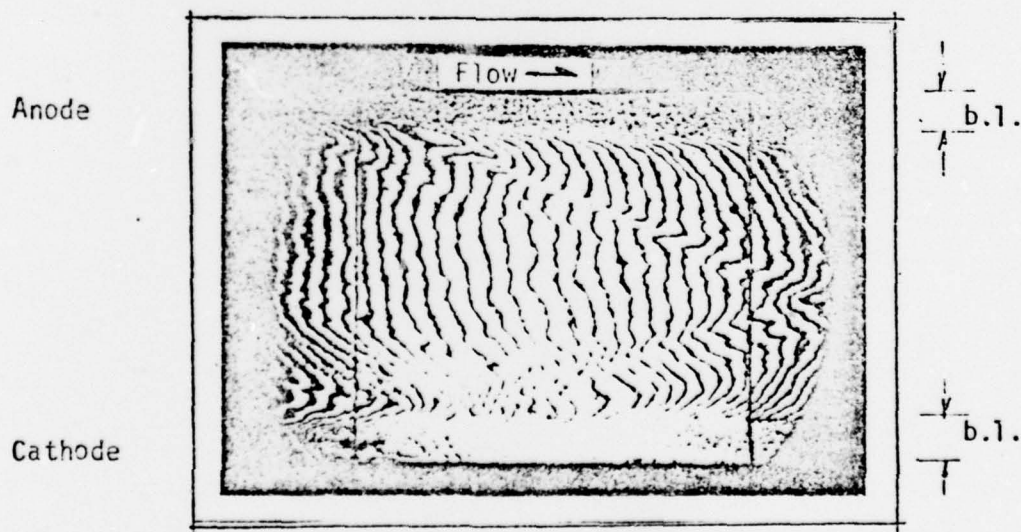


Fig. 34 Interferogram of Flow Process
 with Discharge on.